University of Potsdam
Institute of Physics and Astronomy
Applied Condensed-Matter Physics
Karl-Liebknecht-Straße 24/25
Haus 28
14476 Potsdam-Golm

Soft nanocomposites
with enhanced electromechanical response
for dielectric elastomer actuators

Dissertation in partial fulfillment of
the requirements of the degree of
Doctor of Natural Sciences
(Dr. rer. nat.)

submitted to the Faculty of
Mathematics and Natural Sciences of
the University of Potsdam

presented by

Hristiyan Stoyanov

Matr. Nr.: 734400

$01.02.2007 - 30.04.2010$

Supervised by

Prof. Dr. Reimund Gerhard

Abstract

Electromechanical transducers based on elastomer capacitors are presently considered for many soft actuation applications, due to their large reversible deformation in response to electric field induced electrostatic pressure. The high operating voltage of such devices is currently a large drawback, hindering their use in applications such as biomedical devices and biomimetic robots, however, they could be improved with a careful design of their material properties. The main targets for improving their properties are increasing the relative permittivity of the active material, while maintaining high electric breakdown strength and low stiffness, which would lead to enhanced electrostatic storage ability and hence, reduced operating voltage. Improvement of the functional properties is possible through the use of nanocomposites. These exploit the high surface-to-volume ratio of the nanoscale filler, resulting in large effects on macroscale properties.

This thesis explores several strategies for nanomaterials design. The resulting nanocomposites are fully characterized with respect to their electrical and mechanical properties, by use of dielectric spectroscopy, tensile mechanical analysis, and electric breakdown tests. First, nanocomposites consisting of high permittivity rutile TiO_2 nanoparticles dispersed in thermoplastic block copolymer SEBS (poly-styrene-co-ethylene-co-butylene-co-styrene) are shown to exhibit permittivity increases of up to 3.7 times, leading to 5.6 times improvement in electrostatic energy density, but with a trade-off in mechanical properties (an 8-fold increase in stiffness). The variation in both electrical and mechanical properties still allows for electromechanical improvement, such that a 27 % reduction of the electric field is found compared to the pure elastomer. Second, it is shown that the use of nanofiller conductive particles (carbon black (CB)) can lead to a strong increase of relative permittivity through percolation, however, with detrimental side effects. These are due to localized enhancement of the electric field within the composite, which leads to sharp reductions in electric field strength. Hence, the increase in permittivity does not make up for the reduction in breakdown strength in relation to stored electrical energy, which may prohibit their practical use. Third, a completely new approach for increasing the relative permittivity and electrostatic energy density of a polymer based on 'molecular composites' is presented, relying on chemically grafting soft π-conjugated macromolecules to a flexible elastomer backbone. Polarization caused by charge displacement along the conjugated backbone is found to induce a large and controlled permittivity enhancement (470 % over the elastomer matrix), while chemical bonding, encapsulates the PANI chains manifesting in hardly any reduction in electric breakdown strength, and hence resulting in a large increase in stored electrostatic energy. This is shown to lead to an improvement in the sensitivity of the measured electromechanical response (83 % reduction of the driving electric field) as well as in the maximum actuation strain (250 %). These results represent a large step forward in the understanding of the strategies which can be employed to obtain high permittivity polymer materials with practical use for electro-elastomer actuation.

Zusammenfassung

Die Palette von elektro-mechanischen Aktuatoren, basierend auf dem Prinzip weicher dehnbarer Kondensatoren, scheint besonders für Anwendungen in der Medizin und für biomimetische Applikationen unbegrenzt. Diese Wandler zeichnen sich sowohl durch hohe Reversibilität bei großer mechanischer Deformation als auch durch ihre Flexibilität aus, wobei die mechanischen Deformationen durch elektrische Felder induziert werden. Die Notwendigkeit von hoher elektrischer Spannung zur Erzeugung dieser mechanischen Deformationen verzögert jedoch die technisch einfache und breite Markteinführung dieser Technologie. Diesem Problem kann durch eine gezielte Materialmodifikation begegnet werden. Eine Modifikation hat das Ziel, die relative Permittivität zu erhöhen, wobei die Flexibilität und die hohe elektrische Durchbruchsfeldstärke beibehalten werden sollten. Durch eine Materialmodifikation kann die Energiedichte des Materials bedeutend erhöht und somit die notwendige Betriebsspannung des Aktuators herabgesetzt werden. Eine Verbesserung der funktionalen Materialeigenschaften kann durch die Verwendung von Nanokompositen erzielt werden, welche die fundamentalen Eigenschaften der Nanopartikel, d.h. ein gutes Verhältnis von Oberfläche zu Volumen nutzen, um eine gezielte makroskopische Materialmodifikation zu bewirken.

Diese Arbeit behandelt die Anwendung innovativer Strategien für die Erzeugung von Nanomaterialien mit hoher Permittivität. Die so erzeugten Materialien und deren relevante Aktuatorkenngrößen werden durch elektrische und mechanische Experimente vollständig erfasst. Mittels der klassischen Mischansätze zur Erzeugung von Kompositmaterialen mit hoher Permittivität konnte durch nichtleitendes Titaniumdioxid TiO_2 (Rutile) in einem Thermoplastischen-Block-Co-Polymer SEBS (poly-styrene-co-ethylene-co-butylene-co-styrene) die Permittivität bereits um 370 % erhöht und die elektrische Energiedichte um 570 % gesteigert werden. Diese Veränderungen führten jedoch zu einem signifikanten Anstieg der Steifigkeit des Materials. Aufgrund der positiven Rückkopplung von elektrischen und mechanischen Eigenschaften des Kompositmaterials ermöglicht bereits dieser einfache Ansatz eine Verbesserung der Aktuation, bei einer 27 %-igen Reduktion der Aktuatorbetriebsspannung. Eine direkte Verwendung von leitfähigen Nanopartikeln kann ebenso zu einem Anstieg der relativen Permittivität beitragen, wobei jedoch die Leitfähigkeit dieser Nanopartikel bedeutende Wechselwirkungen verursacht, welche somit die Energiedichte des Materials negativ beeinflusst und die praktische Verwendung dieses Kompositsystems ausschließt. Als ein völlig neuer Ansatz zur Steigerung der relativen Permittivität und Energiediche und abweichend vom klassischen Mischverfahren, wird die Herstellung eines "Molekularen Komposits", basierend auf einem chemischen Propfverfahren, präsentiert. In diesem Ansatz wird ein π-konjugiertes leitfähiges Polymer (PANI) an die Hauptkette des Elastomers der Polymermatrix gebunden. Die daraus resultierende Ladungsverteilung entlang der Elastomerhauptkette bewirkt eine 470 %-ige Steigerung der Permittivität des "Molekularen Komposits" im Vergleich zur Permittivität des unbehandelten Elastomermaterials. Aufgrund der Verkapselung der chemischen Bindungen der PANI-Kette entstehen kaum negative Rückwirkungen auf die elektrischen und mechanischen Eigenschaften des so erzeugten Komposits. Diese Materialeigenschaften resultieren in einem signifikanten Anstieg der Energiedichte des Materials. Das mittels dieses Verfahrens erzeugte Komposit zeigt sowohl eine Steigerung der Sensitivität der elektromechanischen Antwort (Reduktion des elektrischen Felds um 83 %) als auch eine bedeutende Steigerung der maximalen Aktuation (250 %). Die Ergebnisse und Ideen dieser Arbeit stellen einen wesentlichen Sprung im Verständnis zur Permittivitätssteigerung in Polymermaterialien dar und werden deshalb in der Erforschung und Entwicklung von Elastomeraktuatoren Beachtung finden.

Acknowledgements

First of all it is my pleasure to thank Prof. Dr. Reimund Gerhard for giving me an opportunity to work in his group and for the many years of supervision, encouragement and support.

I would like to express my sincere and deepest gratitude to the Kompakt project leader Dr. Guggi Kofod-the invisible driving force behind all the achievements in this work. Thank you for your support, generous help and unlimited patience, while teaching me how to play the "Glassperlenspiel" in science.

Further, I would like to thank Dr. Denis McCarthy for his valuable suggestions throughout the project. I endow my sincere thanks to all the ACMP group members for their assistance and cooperation and particularly Dipl. Ing. Werner Wirges for the valuable suggestions in the experimental work. I would like to convey my thanks to all the guys involved in the Kompakt project: Phisan Katekomol, Sebastian Risse, Michael Melzer, Andre Becker. Especially, I would like to thank our technician Dipl. Ing. Hülya Ragush for her help to build the new experimental setups and for all technical support. I endow my sincere thanks to Sebastian Risse for helping me constantly with LaTeX and especially for his kind assistance in the design and page layout of the dissertation. I would like to thank Sandra Zeretzke for the assistance with the arrangement of my administrative tasks. My heartiest thanks to Mr. Breakdown-Mathias Kollosche for sharing the destiny of being a PhD student with me. His friendship, encouragement and successful cooperation from the preliminary to the concluding level enabled me to develop a broad understanding of the subject. I am greatly indebted to him for the translation of the Abstract in German and his efforts in helping me to broaden my view and knowledge of the German language. I endow my sincere thanks to my flatmate Daniel Storey for reviewing the thesis and for helping me to deepen my knowledge of the English language.

Last but not least, I would like to thank my family. This thesis would not have been possible without their love and support.

Contents

Chapter 1

Introduction

1.1 Motivation

Muscle is a biological contractile system, which converts the chemical energy of ATP (adenosine trisphosphat) into mechanical work. It is considered to be highly optimized system, since the structure is fundamentally the same for all animals and variations between species are small. After millions of years of evolution, Nature has created a highly sophisticated actuator mechanism. Muscle is hierarchically organized to rely on functions occuring at the microscopic level. The hierarchical organization of the muscle is illustrated in Fig. 1.1.
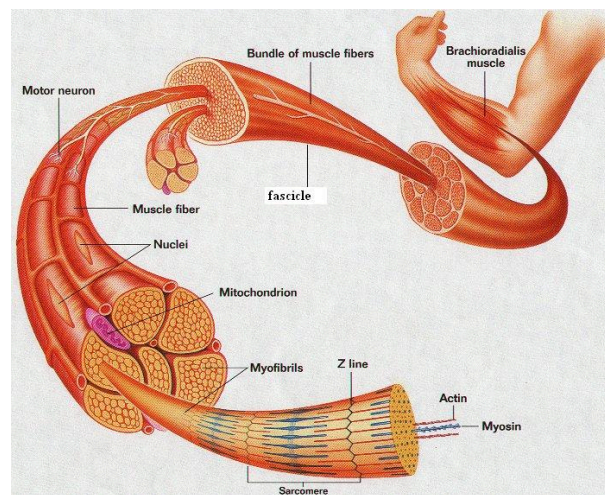
Figure 1.1: Structure of the human muscle (www.bioanim.com).

The functional unit of contraction, myofibril, comprises of several hundred contractile protein filaments-actin and myosin. The filaments form an ordered array and make up sarcomeres, the contractile units of myofibril. Bundles of parallel-oriented myofibrils form individual muscle fibers (cells). Muscle fibers are bundled to form fascicles and the fascicles are bundled to form the muscle organ. Muscle organ itself is a very complicated three dimensional nanofabricated system with integrated sensors, energy delivery, waste/heat removal, local energy supplies, actuator, and repair mechanisms. Muscle tissue contracts and relaxes when triggered by electrical stimuli from the brain, through the nerves.

It is not surprising that for many years, human technology has attempted to emulate biological muscles with artificial systems. Actuators or motion-generating devices are driving many mechanisms that are used in our daily life. For many years, efforts have been made to reduce their size, mass and power as well as use them to operate biologically-inspired devices. One of the first attempts for artificial muscle modelling was made in the early 1950's by an American physician Joseph L. McKibben. He developed and investigated the behavior of a variety of pneumatic actuators now known as McKibben actuators. A very attractive feature of McKibben actuator is its very high force to weight ratio 400:1 compared to alternatives at this time such as pneumatic cylinders and DC motors, which had ratios in the order of 16:1 [1]. The main disadvantage of this artificial modelling system is that McKibben actuator performance depends on compressed gas which is supplied by a compressor driven by bulky electric motors. Thus, the weight, limited sizes and complex transmissions of electric motors has constrained the design and development of this artificial muscles approach.

The next step in the development of artificial muscles was the introduction of shape memory alloys (SMA) and electroactive ceramics (EAC). They were considered as actuation material candidates for replacing heavy electric motors and hydraulic actuators. Shape memory alloys are a group of smart materials that demonstrate the ability to undergo substantial plastic deformation, and then return to their original shape when subjected to the appropriate thermal process [2]. With regard to using shape memory alloys as an approach to muscle like actuators, there are a number of issues impeding their suitability. The main disadvantage is the slow response time. SMAs need a long time to cool and return to their lower temperature shape, thus limiting the expansion-contraction cycle time. However, due to the biocompatibility of some SMAs, their application in medicine - osteosynthesis is being investigated and looks promising. Actuators based on piezoelectric ceramic materials probably represent the most mature and best established of the different emerging technologies. The physical phenomenon of piezoelectricity provides the foundation for the transduction process upon which all piezoelectric actuators are based. Piezoelectric ceramics possess both a direct effect, in which an electrical charge is generated by a mechanical stress, and the converse effect, in which an electrical field produces a mechanical displacement. EAC found application in many actuation mechanisms in robotics, vibration isolation, active damping and many others [2], however the fragility and maximum actuation strains on the order of 1 % make them unsuitable for artificial muscle development.

In the beginning of the 1990s, a new class of smart materials, which respond to electrical stimulation with significant change in shape or size, nowadays widely known as Electroactive polymers (EAPs) emerged in the field of actuators. Pioneers in the field considered them as artificial muscles of the future due to their superior characteristics and similarity in performance to biological muscles. The similarity includes resilient, damage-tolerant and large actuation strains (stretching, contracting, or bending) [1, 3]. Researchers in the field of biomimetics (where designs are based on biologically-inspired models) predict that these materials could be used to mimic the movements of animals, insects and even human body parts. The performance of the emerging polymer actuators exceeds that of natural muscle in many respects, making them particularly attractive for use anywhere where a muscle-like response is desirable, including in medical devices, prostheses, robotics, toys, biomimetic devices, and micro/nanoelectromechanical systems [4]. EAPs can be sub-divided based on their actuation mechanism into two major classes: ionic EAPs (also called "wet" because they often use an aqueous component material) and electric field activated EAPs. Both types of EAPs possess complimentary advantages and disadvantages (for detailed discussion see [1, 4]. The sub-class of EAPs whose responses are stimulated by external electrical fields (known as the field-activated EAPs) attract attention due to their medium to good performance in all

categories, including high achievable strain, energy density, actuation pressure and response speed [1,5]. Among the different electric field activated EAPs (e.g. ferroelectric polymers, electrostrictive polymers, dielectric elastomers, liquid crystal elastomers) dielectric elastomers have shown the best electromechanical performance in terms of actuation strain, force and elastic energy density [6]. Their actuation response is the result of electrostatic interactions between electrodes and based on that mechanism, extremely large strains (> 200 %) can be obtained [7]. More typically the strains are 10-100 %, which compares well with the response observed in skeletal muscle (20-40 %) [4]. High electromechanical coupling leads to a high work density 3.4 MJ/m^3, which is approximately 400 times that of human muscles [7,8]. A drawback of dielectric elastomer actuators (DEA), which is a common problem for all electric field activated actuators, is the need of high voltages (> 1 kV) as a result of the high electric fields (> 100 MV/m) needed to drive them. Indeed, the high voltages are not a technical problem, since compact dc-to-dc converters are commercially available, however, high voltages are a major concern mainly because of related safety issues, particularly in some of the potential areas of application, e.g. biomedical devices, biomimetic robots and toys. Due to these drawbacks, commercial application of these materials is at an early stage. Hence, research efforts are currently aimed at finding new materials which enable lower operating voltages. The challenge can be overcome via improvements in material properties, which is the aim of this work.

1.2 Background and literature review

1.2.1 DEA electromechanical response and material requirements

A dielectric elastomer actuator can be regarded as a compliant capacitor, in which the conversion of electrical energy into mechanical work is due to the coupling of the electrostatic stress with the elastic deformation. Fig. 1.2 displays schematically the DEA operating principle.
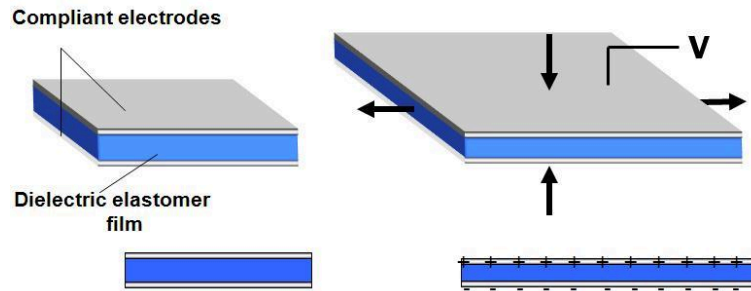
Figure 1.2: Schematical view of DEA operating principle.

Physically, application of a voltage difference to the compliant capacitor causes charge to flow to the electrodes. Additional charges are accumulated on the electrodes as a result of the polarization in the dielectric material. The attraction of these physical charges on opposing electrodes leads to an electrostatic force [7,9], called the Maxwell stress, which is commonly written as (for detailed discussions see Sec. 2.3):

$$p = \sigma E = \varepsilon_r' \varepsilon_0 E^2, \tag{1.1}$$

where σ is the charge density, $\varepsilon_0 = 8.85*10^{-12}$ F/m is the vacuum permittivity, ε'_r is the relative permittivity (real part) and E is the electric field. The electrical stress on the dielectric medium in turn leads to mechanical deformation. Eq. (1.1) shows that higher electrostatic pressure is expected from a dielectric material capable of inducing higher charge density at a given electric field. Therefore the storage of electrical charges inside the active dielectric elastomer material is fundamental to the electromechanical response of DEA. The deformation in the material caused by the electrical stress continues until a balance is achieved between electric and elastic forces. Since the elastic force depends on the Young's modulus (Y) of the material, the electromechanical actuation strain of the DEA can be written as (in the case of very low strain):

$$S = \frac{\varepsilon'_r \varepsilon_0 E^2}{Y} = \beta E^2 \tag{1.2}$$

For strains higher than 5-10 %, the above equation is replaced by a more complicated nonlinear hyperelastic equivalent [10], but the argument that the material should have a low stiffness to display large strains remains. Eq. (1.2) includes all the important material parameters and based on it and the above considerations, it can be concluded that the ideal material for this technology would have a high permittivity, low Young's modulus and high electric breakdown strength to support high applied electric fields. A factor β can be defined, as the strain sensitivity for a given electric field, and it is a valuable measure of the actuation properties of a given material. Many commercially available elastomers meet the mechanical requirement for actuation, however inherently elastomers suffer from low electrostatic energy density due to relatively low permittivity (below 5). Consequently, the necessary high energy density for actuation relies on the possibility of applying high electric fields (>100 MV/m). For a given material, if the real part of the permittivity could be increased independently of other parameters, from Eq. (1.2) above, it is expected that the electromechanical actuation properties would improve. Correspondingly, an increased permittivity can lead to a significant reduction of the high driving electric fields, which in turn leads to lower driving voltages, which would be an advantage for some areas of application. Another approach allowing reduction in the operating voltage, would be decreasing the thickness of the elastomer film. However due to the difficulties related with producing and handling of very thin elastomer films (about 1 µm), the research interest has been focused mainly on developing elastomer materials with high permittivity.

1.2.2 Towards high permittivity nanocomposites

Generally, polymer materials with high permittivity and high energy density are the key enablers for numerous capacitive applications such as thin film capacitors with small foot-prints embedded in circuit boards [11], compact electronic devices such as organic field effect transistors or random access memories based on capacitive elements [12], as well as piezoelectric and pyroelectric sensors [13]. Moreover, there is growing need for polymer capacitors that can store large amount of energy and then deliver it instantaneously, e.g. for stationary power systems, hybrid electric vehicles [14]. Therefore, much research has been carried out to develop high permittivity composites with improved energy storage. The researchers sought to combine the unique mechanical properties of polymers, such as flexibility and light weight, as well as versatile chemistry, processability, and simple manufacturing, with the superior electrical properties of different nanofiller particles to obtain high permittivity nanocomposites. To date, the literature reports approaches for increasing the permittivity based on the following physical principles: 1) mixing rule - dispersion of insulating high permittivity ceramic particles and 2) subpercolative approach - dispersion

of conductive particles below the percolation threshold. Another particularly promising approach, which can be regarded as a subcategory of the percolative approach is the dispersion of nano-clusters of highly polarizable molecules. Both approaches possess advantages and disadvantages and will be discussed in the following subsection.

Current trends in DEA research are to adopt the approaches for increasing the permittivity of the polymer and to apply them directly with respect to DEA. Increasing the permittivity of a compliant capacitor for DEA exposes one more challenge, the corresponding increase in permittivity would be beneficial only if it is accompanied with little or no change in elastic properties (mechanical reinforcement).

1.2.2.1   High ε'_r nanocomposites - literature review

As mentioned above, improved permittivity and energy density also benefits other applications, hence approaches used to improve other polymers could apply for elastomers as well. In this subsection, a review of the recent works in the field is presented.

The mixing rule approach in which high permittivity metal oxide particles such as (TiO_2, $BaTiO_3$, lead zirconate titanate (PZT), etc.) are randomly dispersed in a polymer matrix has proved to be suitable for considerable enhancements of the dielectric properties, while maintaining very low dielectric losses ($\tan \delta$). The methodology of this approach is to combine the desirable dielectric properties of ceramic particles with a high breakdown strength and mechanical flexibility of the polymer. Studies have shown that the permittivity of a 0-3 connectivity type composite is dominated by the matrix, therefore, a relatively large volume fraction of high dielectric constant inorganic phase is needed [15]. For example, in the representative work the authors prepared mixed connectivity composites consisting of calcium modified lead titanate (PTCa) ceramic powder dispersed in polyvinylidene fluoride trifluoroethylene (PVDF-TrFE). At 50 vol% an increase of 4.5 times ($\varepsilon'_r = 36$ at 1 kHz) over the polymer matrix ($\varepsilon'_r = 8.1$ at 1 kHz) was observed. Bai et al. [13] reported $Pb(Mg_{1/3}Nb_{2/3})O_3$-$PbTiO_3$ (particle size 500 nm)/P(VDF-TrFE) composites with an ε'_r value above 200 at 60 vol%. Rao et al. [16] prepared a lead magnesium niobate-lead titanate (PMN-PT)+$BaTiO_3$/high-ε'_r epoxy system ($\varepsilon'_r = 6.4$) composite with ε'_r value of 150 and dielectric loss ($\tan \delta$) of 0.016, in which a ceramic filler loading as high as 85 vol% was used. At such high filler loadings the composites suffer degradation of mechanical properties, in terms of high weight, low flexibility and weak matrix-filler bonding. However, an optimum can be found, where the composite material retains certain flexibility while displaying improved dielectric response [17]. Table 1.1 summarizes the type, composition and dielectric properties of different ceramic/polymer composite systems reported in the literature.

The size of filler particles has been shown to have a strong influence on the dielectric properties. Lewis [18] proposed that as the size of filler particles decreases to the nanometer scale, the properties of the polymer-filler interface would become dominant over the bulk properties of the phases. Experimentally, the concept was tested by Sun et al. [19] who has shown that the dielectric permittivity of a composite consisting of nanosize silica particles dispersed in epoxy polymer is higher than for a composite with micro-size particles. Tanaka et al. [20] proposed a multi-core model to explain the influence of the interphase on the dielectric properties. According to it, the interphase of a spherical inorganic particle embedded in a polymer matrix consists of three layers: a bonded layer, a bound layer and a loose layer. The diffuse Gouy-Chapman layer is superimposed to the above three layers. The first layer corresponds to a contact layer where the polymer is in contact with the filler surface, and the second corresponds to the interfacial layer region. The third layer is a region loosely coupled and interacting with the second layer. It is

Table 1.1: Summary of the ceramic/polymer nanocomposites.

materials	ε'_r	$\tan \delta$	filler size	filler loading	ref.
PTCa/ PVDF-TrFE	36	N/A	N/A	50 vol%	[15]
$Pb(Mg_{1/3}Nb_{2/3})O_3$- $PbTiO_3$/P(VDF-TrFE)	200 (10 kHz)	0.1 (10 kHz)	500 nm	50 vol%	[13]
PZT/PVDF	50	N/A	20 µm	50 vol%	[21]
PMN-PT+$BaTiO_3$/ high-k epoxy	150 (10 kHz)	0.016 (10 kHz)	900 nm/ 50 nm	85 vol%	[16]
$CaCu_3Ti_4O_{12}$/ P(VDF–TrFE)	243 (1 kHz)	0.26 (1 kHz)	N/A	50 vol%	[17]
$BaTiO_3$/ P(VDF-HFP)	37 (1 kHz)	< 0.07 (1 MHz)	30-50 nm	50 vol%	[22]

argued, that the second layer contributes to the reduction in the permittivity by disturbing the motion of dipoles originating from some polar group. Since, the first layer is directly linked to the filler, the second and the third layers are suggested to be the most influential in affecting the dielectric properties of the composites.

Direct influence of the interfacial region and therefore on the dielectric properties can be achieved by attaching suitable organic molecules (in terms of polarity, polarizability) to the filler particles. Kim et al. [22] determined that effective binding of phosphonic acids to $BaTiO_3$ influence the interfacial interaction between the particles and P(VDF-HFP) host polymer. As a result, a well dispersed nanocomposite with high ε'_r and high dielectric strength was obtained. Influence of the interfacial region by chemical modification of the filler particles is a very important step in high permittivity composites showing that by changing the interfacial interaction between filler and host polymer, not only can the dielectric permittivity be influenced, but the electric breakdown strength as well. The previous studies dealing with electric breakdown of ceramic/polymer composites showed that the addition of nanoparticles have a negative impact on the composite breakdown strength, which is caused by the filler particles acting as electrical defect centers that distort and enhance the local field, resulting in reduced breakdown strength [23,24]. By proper chemical modification of the filler particles, the electrical breakdown strength can be enhanced as shown in the representative work [22].

The applicability of the mixing rule approach to DEA has been tested by Carpi et al. [25]. They studied a polymer-ceramic composite, consisting of a silicone matrix in which titanium dioxide powder (10 µm grain size) was dispersed. The authors observed a decrease of the Young's modulus at 30 vol% which was ascribed to cavitation, and deterioration of the mechanical properties for higher volume fractions due to ineffective crosslinking. The observed increase of the permittivity (from 5.5 to 8 for 30 vol%) in combination with a decrease in the Young's modulus resulted in improved electromechanical response and reduction in the driving voltages.

The sub-percolative approach in which conductive filler nanoparticles are dispersed in polymer matrix is based on percolation theory predicting a large deviation of the relative permittivity on approaching the insulator-conductor transition [26]. The increase follows a power law $\varepsilon_c = \varepsilon'(p_c - p)^{-s}$, where ε' is the relative permittivity of the polymer matrix, s is a critical exponent characterizing the transition, p is the fraction of the conductive filler and p_c is the percolation threshold. An advantage of the sub-percolative approach compared to the mixing rule approach is the possibility of enhancing the relative permittivity substantially above that of the polymer matrix at a low filler concentration, thereby possibly preserving

the valuable mechanical properties of the base polymer material. Several authors have already investigated different conductor-insulator systems and reported substantial permittivity increases. Poly(vinylidene fluoride)(PVDF) was commonly chosen as the polymer matrix, although epoxy, silicone rubber and PVDF copolymers have also been investigated. For example, the enhancement effect was demonstrated with metal conducting particles like Ni ($d = 5$ µm) in PVDF and at 18 % filler loading values of 400 and loss factor of 0.18 at 100 Hz were reported [27]. Rao et al. [16] prepared silver(Ag) flake epoxy composites and reported a high permittivity, $\varepsilon'_r \approx 2000$ and a loss factor tan δ of 0.24 at 10 kHz. Similar effects were found with carbon-based particles, such as carbon nanotubes [28] and with acetylene black (CB) [29]. Finally, the effects can be observed with conducting polymers as filler, as demonstrated with polyaniline in PVDF [30]. Details of some subpercolative composite materials reported in recent years are summarized in Table 1.2.

Table 1.2: Summary of the subpercolative composites.

materials	ε'_r	tan δ	filler size	filler loading	ref.
Ni/PVDF	400 (100 Hz)	0.18 (100 Hz)	5 μm	18 vol%	[27]
Ag flake/epoxy	2000 (10 kHz)	0.24 (10 kHz)	1.5 μm	11.2 vol%	[16]
steel fiber/PVDF	427 (50 Hz)	> 100 (50 Hz)	d=30 μm l=500 μm	10 vol%	[31]
nanocrystalineNi/ PVDF	2050 (100 Hz)	10 (100 Hz)	$\sim$30 nm	28 vol%	[32]
self-passivated Al/ epoxy	100 (10 kHz)	0.02 (10 kHz)	100 nm	50 wt.%	[33]
carbon-nanotubes/ PVDF	50 (1 kHz)	0.3 (1 kHz)	N/A	1.6 vol%	[28]
acetylene black/ PVDF	56 (100 kHz)	0.15 (100 kHz)	N/A	1.3 vol%	[29]
polyaniline/ PVDF	2000 (100 Hz)	0.8 (100 Hz)	< 1000 nm	23 vol%	[30]

As can be readily seen, the effect is universally observable, and on first it appears plausible that this effect could be employed directly for enhancement of permittivity where this is required. One of the major hurdles for this type of high permittivity composites is the high dielectric loss inherent in these systems. High dielectric loss is due to the conductivity increase approaching the insulator-conductor transition. Currently, much work has been focused on strategies leading to decrease of the high dielectric losses. For example, Xu et al. [33] reported a modified percolative composite consisting of self-passivated Al/epoxy composite having a $\varepsilon'_r = 100$ at 10 kHz and low dielectric losses tan $\delta = 0.02$ at the same frequency. The reason for the low tan δ was ascribed to the self-passivation of Al particles, leading to a dense insulating shell around the particles preventing current leakage. However, assessment of the usefulness of the sub-percolative approach for energy storage requires further investigations, as in the literature little was found that focused on the electric breakdown strength and associated energy density for these type of composites.

Another particularly promising approach, which can be regarded as a subcategory of the percolative approach is the dispersion of nano-clusters of highly polarizable molecules. Zhang et al. [34] used copper-phthalocyanine (CuPc) oligomer, which is an organic semiconductor material with dielectric constant as high as 10^5, and dispersed it in P(VDF-TrFE) matrix. The composite showed a ε'_r of 225 and a loss

factor tan δ of 0.4 at 1 Hz. The improvement of dielectric properties was ascribed to a displacement of the electrons under electric fields from the conjugated π-bonds within the entire molecule. Enhancement in the relative permittivity was found to lead to an improvement in the electromechanical response and reduction in the driving electric field. A high permittivity value of 7000 (at 1 kHz) and tan δ of 0.6 for composites with 25 vol% has been achieved by Huang et al. [35] in an all-polymer composite material, fabricated by a combination of conductive π-conjugated polyaniline (PANI) particles coated with insulating polymer with a poly (vinylidene fluoride-trifluoroethylene-chlorotrifluoroethylene) [P(VDF-TrFECTFE)] terpolymer matrix ($\varepsilon'_r > 50$). The authors observed a decrease in the electrical breakdown strength, however a strong increase in dielectric permittivity led to significantly enhanced strain response. The decrease in breakdown strength was attributed to excessive agglomeration, ascribed to incompatibility of the organic fillers with the polymer matrix. Further Huang et al. [36] showed that chemically grafting the oligomer particles to the backbone improves the compatibility. This resulted in a fully functionalized nanophase polymer in which nanocrystallites were found to be well-distributed in the polymer matrix, which was seen to improve the electric breakdown strength and the electromechanical response.

Following the above discussion, it can be concluded that the main challenge for all approaches to composite polymers with improved energy density lies in maintaining the breakdown strength. There is an indication that when the filler is of nanoscopic dimensions, the internal electric field distribution will have local spots of increased electric field concentration, which reduces the electrical breakdown strength of the composite [37]. To achieve electromechanically active polymers with high actuation strain, it is required that the improvement in these two parameters is balanced with a low increase in the elastic modulus.

1.3   Aim and Scope of the Work

The aim of this thesis is to investigate different nanocomposite approaches with respect to their applicability for DEA and to gain a physical understanding of the phenomena involved. The primary goal of this work is to develop soft nano-composite elastomer materials with enhanced electro-mechanical response for dielectric elastomer actuators (DEA). A schematic representation of the strategies employed is shown in Fig. 1.3. Improvement of the electro-static energy storage (high permittivity) is made using the following approaches: addition of ceramic nano-particles (I), sub-percolating conductive particles (II) or nano-domains of highly polarizable molecules (III). By developing an understanding of the employment of conductive percolating particles (percolative composites), the issue of electrically conductive compliant electrodes (IV) can be addressed as well.
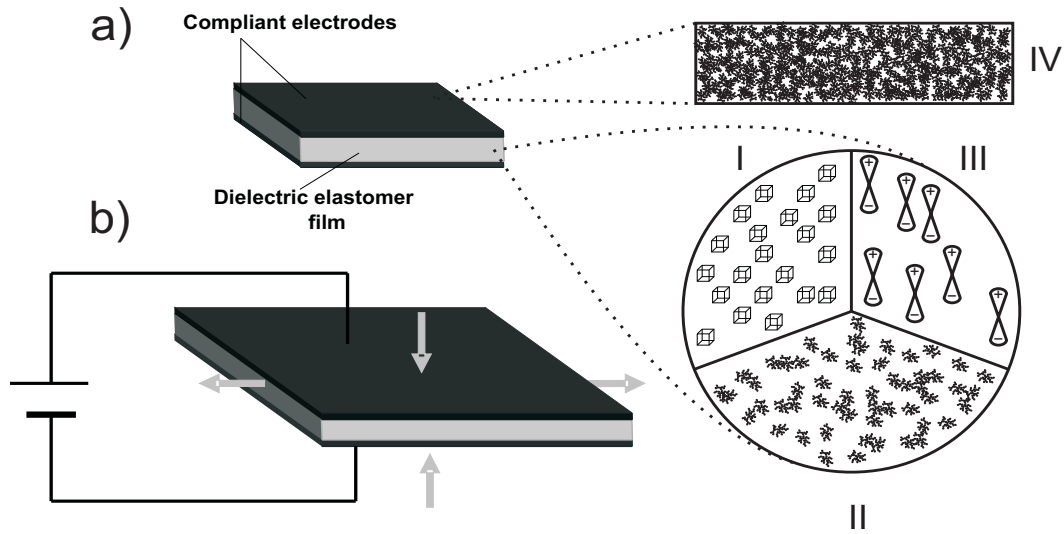
Figure 1.3: Schematic representation of the possible composite structures of the active material: I-ceramic particles, II-subpercolative conductive particles, III- nano-clusters of highly polarizable molecules, IV-conductive percolative network for compliant electrodes.

1.3.1   Thesis Outline

This thesis is organized such that each chapter has its own introduction. Chapter 1 includes an introduction to EAPs with a focus on dielectric elastomer actuators. DEA principle of actuation is discussed and the material requirements are outlined. A literature review of the recent works in the field of high permittivity composites is presented and discussed with respect to DEA.

The comprehensive theoretical review in Chapter 2 gives an introduction to polymers and elastomers and discusses the concept of dielectricity in static and alternating electric fields. Electrostatic stress and the corresponding electro-mechanical instability in soft compliant capacitors are discussed in details. Finally, different theories of high permittivity composites: effective medium theory (EMT), classical mixing rules and percolation theory are discussed.

In Chapter 3, the chemistry and functional properties of the materials used in this work are reviewed.

Chapter 4 describes the experimental methods and preparation procedures for the composites. Finally, the various experimental techniques used for characterization of the materials are outlined.

Chapter 5 is devoted to the complete electro-mechanical evaluation of the mixing rule approach for permittivity enhancement. In particular TiO$_2$-SEBS composites are investigated and are shown to exhibit substantial increase of the permittivity, but with a trade-off in mechanical properties. Further, it is demonstrated that balance between electrical and mechanical properties can be found resulting in improved electro-mechanical response. This chapter will be submitted to *Soft Matter* for publication.

In Chapter 6, a sub-percolative approach for increasing the relative permittivity and corresponding energy density of a polymer is evaluated. A model system consisting of carbon black (CB) particles dispersed in SEBS elastomer matrix is investigated and the increase of the relative permittivity is compared with the electric breakdown properties of the composite, in terms of calculated electrical energy density at breakdown. This chapter is published in *Applied Physics Letters*.

In Chapter 7, a completely new approach for increasing the electro-static energy density of polymer, based on molecular composites is presented. It is shown that chemically grafting π-conjugated macromolecules (polyaniline (PANI)) to a flexible elastomer backbone SEBS-g-MA (poly-styrene-co-ethylene-co-butylene-co-styrene-g-maleic anhydride) results in molecular composites of strongly increased permittivity with hardly any reduction in the electric breakdown strength, resulting in a large increase in stored electrostatic energy. This lead to an improvement in the measured electromechanical response as well as in the maximum actuation strain. This chapter has been accepted for publication in *Journal of Materials Chemistry*.

Finally, concluding remarks are summarized in Chapter 8, along with recommendations for future work.

Chapter 2

Theory and background

This chapter is intended to review briefly the basic concepts, the most important experimental results and theoretical approaches reported in the literature which are related to the work in the thesis.

2.1   Introduction to polymers and elastomers

Polymers are long chain-like macromolecules where repeated molecular units known as monomers are linked by covalent bonds. The macromolecular structure is created by a chemical reaction known as polymerization, in which the monomers react with each other forming a molecular chain that can contain a thousand or more repeated units. The atoms, which form the polymer chain, are predominantly carbon atoms or carbon atoms in combination with oxygen and/or nitrogen and/or halogen groups. The nature of chemical bonding between the linking atoms directly influences the electrical properties. For example, most polymers are insulators and resist the flow of a current. The poor conduction of electricity arises from the strong covalent σ-bonds between the atoms, which localizes the electrons in the molecular structure, thus preventing charge transport. Polyethylene, consisting of -CH_2- repeating units, is the typical example of a saturated polymer consisting of σ-bonds formed from sp^3 hybrid orbitals between carbons (Fig. 2.1(a)). Since the carbon atom has four valent electrons with an electron configuration of $1s^2 2s^2 2p^2$, sp^2 hybridization is also possible, in which the 3 sp^2 orbitals lie in a plane with angles of $120°$ between them, and one remaining p-orbital lies orthogonal to the plane of the sp^2 orbitals. Carbon atoms with sp^2 hybrid orbitals can form a σ-bond, while the remaining p_z orbitals overlap to form an additional π-bond parallel to the underlying σ-bond. The electrons in the π-bond are less strongly bound than the electrons in the σ-bonds and hence can be easily removed. A macromolecular chain, where the single and double bonds between the atoms alternate, is said to be *conjugated*. An example of conjugated polymer is polyacetylene, consisting of -CH=CH- repeating units (Fig. 2.1(b)). The weaker bonding of the π electrons in conjugated polymers leads to semiconducting properties. The conjugated polymer can be transformed from a semiconductor to a conductor, by partial oxidation or reduction of the π-system, which leads to either increase or decrease in the number of delocalized electrons. The process of increasing the mobility of the electrons in the delocalized orbitals is known as *doping*. The evolution of conducting polymers began in 1975 with the discovery of a linear conjugated organic polymer, polyacetylene, by Shirakawa. Two years after its discovery, higly conductive (metallic) properties were reported, as a result of oxidation with iodine [38].
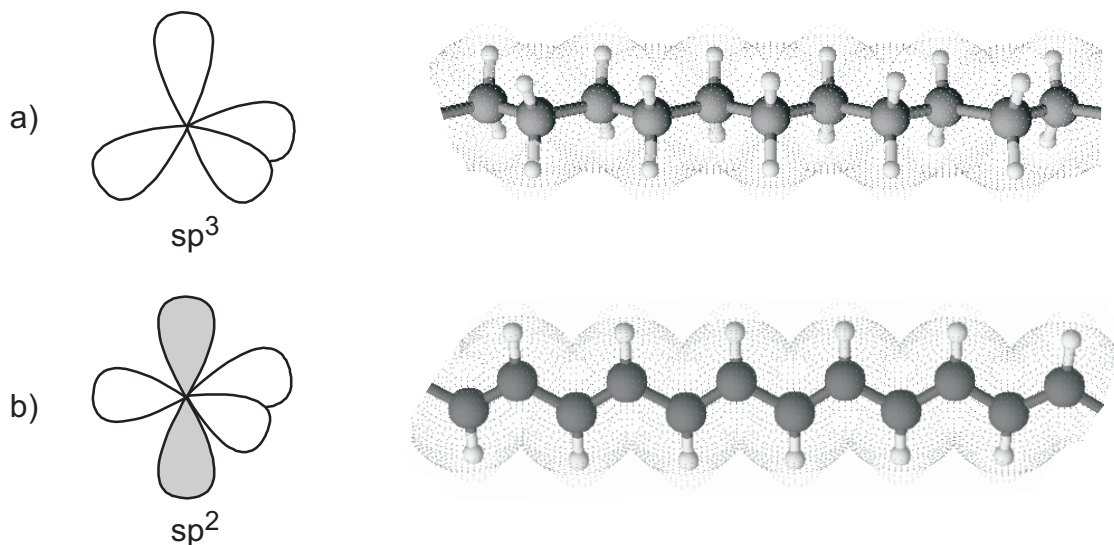
Figure 2.1: a) sp^3 hybrid orbital and molecular structure of polyethylene; b) sp^2 hybrid orbitals and the molecular structure of polyacetylene.

In general, polymers due to their macromolecular structure, have complex shapes and form solids that may be either amorphous or crystalline, but are commonly partially crystalline. Long flexible molecules naturally become highly entangled and contorted with each other in the molten or dissolved state, and reorganization into regular crystalline structures upon solidification is a difficult process. However, some crystallization usually still takes place in most polymers in which the macromolecules wander through ordered and disordered regions. The mechanical properties of a given polymer strongly depend on the length of the polymer chains and the nature of solid formation. Elongation of a piece of solid polymer by applying a force to it, leads first to disentanglement of the macromolecular chains and a consequent slipping of the chains with respect to each other. This behavior is known as *visco-elasticity* [39] and is responsible for the unique mechanical properties of polymers, namely their flexibility. Disentanglement of the chains on the molecular level gives a reversible elastic properties, while the flowing of the chains contributes to the viscous behavior. Due to the higher level of entanglement, it is clear that the amorphous polymers show higher elasticity than the partially crystalline. To prevent the slipping of polymer chains and therefore to promote elastic recovery behavior the mobility of the chains must be low. This is accomplished by chemical bonding of the polymer chains in certain positions, a reaction known as *crosslinking*. The first successful crosslinking of a polymer was done by Charles Goodyear, who invented a method of vulcanization for crosslinking of rubber by heating a mixture of rubber-tree sap and sulphur. By the introduction of a certain number of crosslinking or junction points between the chains, a coherent network is produced in which all macromolecules are linked together and therefore can no longer move independently. Taking these considerations into account, the requirements for an elastic polymer (*elastomer*) as outlined by Treloar [40] are: 1) the presence of long-chain molecules with freely rotating links; 2) weak secondary forces between the molecules; 3) an interlocking of the molecules at a few places along their length to form a three-dimensional network.

The crosslinking of the elastomer can be done either by an irreversible chemical reaction or by a concept known as a *physical* (reversible) *crosslinking*. The physical crosslinking is achieved through the two-phase structure of the elastomer, in a way that two or more monomers are copolymerized, using either block or graft polymerization techniques. One of the monomers makes up the soft or amorphous segment, which

contributes the rubbery characteristics, while the other monomer constitutes the hard, or crystalline segment. It is essential that the hard and soft blocks are immiscible at a molecular level, so that, the hard blocks form separate domains in the amorphous matrix, thereby acting as anchor points which physically crosslinks the rubber domains. The main advantage of physical crosslinking elastomers is their solubility and processability. In contrast, the chemical crosslinking elastomers can not be processed or dissolved after crosslinking. However, the chemical cross-linking elastomers do demonstrate low visco-elastic losses, due to the strong covalent bonds linking the polymer chains.

Elastomers exhibit predominantly entropy-driven elasticity. The elastic behavior results directly from a decrease in entropy associated with the distortion of a chain from its most probable conformation. Entropy driven elasticity manifests in thermo-elastic effect [40]: 1) a stretched elastomer sample subjected to a constant load contracts reversibly on heating; and 2) an elastomer gives out heat reversibly when stretched. The reversible temperature increase follows directly from the fact that the deformation of an elastomer is associated with a reduction of entropy. With no change in internal energy ($dU = 0$), and based on the kinetic theory, it can therefore be written that $dW = -dQ$. The work done by the stretching force (dW) is positive, hence it follows that the heat absorbed (dQ) is negative, i.e. the heat is produced on stretching.

2.2 Dielectrics

Dielectricity is a physical model commonly used to describe how an electric field interacts with atoms or molecules inside a material. For instance, when a metal body is exposed to an electric field, the free electrons flow due to the electric forces against the field until the field in the body vanishes. This gives rise to a charge transport or conduction. In contrast, other type of materials, or *dielectrics* as Faraday (1839) called them are insulators they contain no free charge carriers which can be moved by electric forces. The word dielectric is derived from the prefix dia, originally from Greek, which means "through" or "across"; thus, the dielectric is referred to as a material that permits the passage of the electric field or electric flux, but not any type of charge carriers. Strictly speaking, there is no a truly insulating substance that will obstruct, under all circumstances, the transport of electric charge through it. All real dielectric materials permit to a certain degree, the passage of particles, as a result of impurities and imperfections, however, in view of their exceptional low conductivities, ranging from 10^{-18} to 10^{-6} S/m, they can be regarded as electrical insulators [41]. Due to the redistribution of the bound charges (electrons, protons), such a class of materials exhibit a whole set of effects when placed in an electric field, as will be discussed in the following.

2.2.1 Dielectrics in static fields

The dielectric model is easily understood when we consider a parallel plate capacitor as illustrated in Fig. 2.2. The capacitor consists of two parallel metallic electrodes of an area (A) separated by a distance (d) in a vacuum (Fig. 2.2(a)). When the plates are maintained at a constant potential difference (V), surface charge concentration $+ A\sigma$ and $- A\sigma$ builds up on the capacitor plates, until the voltage drop over the capacitor plates matches that of the voltage source.

The charge density $+ \sigma$ is the source of a uniform electric flux density D_0, which ends on the charge density $- \sigma$ and is directly proportional to the electric field, $E=V/d$, and can be written as:
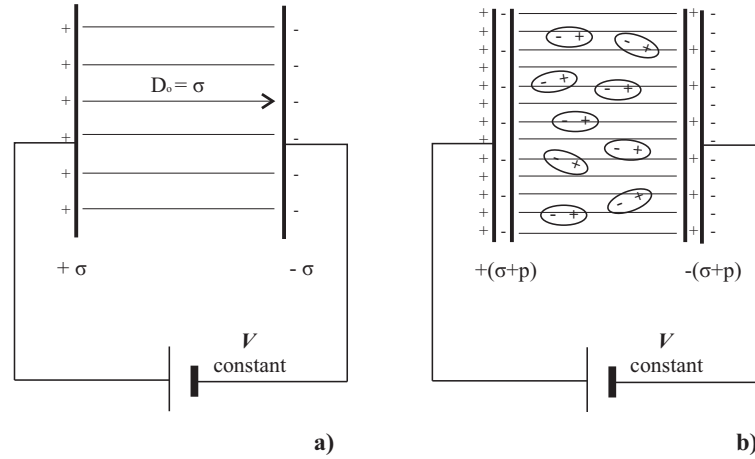
Figure 2.2: Charges on a parallel-plate capacitor with a) a vacuum between the plates, and b) polarized dipoles in the dielectric between the plates.

$$D_0 = \varepsilon_0 E, \tag{2.1}$$

where the constant of proportionality ε_0 is called permittivity of free space and has the value of $8.85*10^{-12}$ F/m. The ratio of the charge on the plate to the difference in potential is the capacitance:

$$C_0 = \frac{A\sigma}{V} = \frac{\varepsilon_0 A}{d} \tag{2.2}$$

If a homogeneous dielectric is introduced between the plates keeping the potential constant (Fig. 2.2(b)), the charge density on the plates increases from σ to $\sigma + p$, leading to an increase of the capacitance.

$$C = \frac{A(\sigma + p)}{V} \tag{2.3}$$

The dielectric medium will respond to the static electric field by redistributing its charge components, an effect known as *polarization*. If the molecules which the material consists of are non-polar, they will become polarized because the electrons will feel a force opposite to the field, while the positively charged nuclei feel a force in the direction of the field. Thus, a dipole moment is induced. This phenomenon is called *displacement polarization*. If the molecules are polar, thus having permanent dipoles, they will go from a random alignment to being oriented parallel to the field direction. This process is called *orientational polarization*. The bound charge densities $\pm p$, that appear on the surfaces of the dielectric are the external effect of the polarization of the individual elements of the dielectric. The increase in the charge density to $\sigma + p$ leads to an increase of the flux density, which adopting more general vector notation can be defined as:

$$\overline{D} = \varepsilon_0 \overline{E} + \overline{P} \tag{2.4}$$

This increase in the flux density occurs without any increase in the potential gradient, and is a measure of the electric *displacement* in the material. The ratio C/C_0 is characteristic of the dielectric material between the plates and is known as a static relative permittivity:

$$\varepsilon_{\text{s}} = \frac{C}{C_0} = \frac{(\sigma + p)}{\sigma} = \frac{\varepsilon_0 \overline{E} + \overline{P}}{\varepsilon_0 \overline{E}} = 1 + \frac{\overline{P}}{\varepsilon_0 \overline{E}} = 1 + \chi, \tag{2.5}$$

where $\chi = \frac{\overline{P}}{\varepsilon_0 \overline{E}}$ is the electric *susceptibility* of the material.

The relative permittivity can vary from material to material depending on the amount of polarization which occurs. It is essentially independent of the applied voltage and therefore the applied field, and it is commonly called dielectric constant of the material. However, it is a complex parameter, which depends on frequency and therefore is more properly termed the relative permittivity (with respect to the absolute permittivity of free space), and this term will be used in this thesis.

2.2.1.1 Polarization and relative permittivity

The polarization of molecular dipoles stores energy in the dielectric medium. It describes the dielectric displacement which originates from the response of a material to an external electric field. If we consider the polarization on the molecular level, the effect of the applied electric field is to induce an electric dipole p on each individual molecule, with a magnitude depending on the local electric field strength E_{L} at the molecule:

$$p = \alpha E_{\text{L}}, \tag{2.6}$$

where the constant of proportionality α is called the polarizability of the molecule. Each molecule of a polarized material will behave electrically as consisted of charges separated by a distance in the electric field direction, resulting in a dipole moment $\overline{P}dv$. In an isotropic material, the effect in the uniform field will be a product of dipole moments $\overline{P}dv$ aligned in the field direction in each elemental volume dv. The total dipole moment, therefore, can be related to the number of molecules per unit volume N_0:

$$\overline{P} = N_0 \alpha \overline{E_{\text{L}}} \tag{2.7}$$

There are five recognizable modes of electrical polarization shown by matter. Four of these operate at the molecular level and can be classified as: electronic, atomic, dipolar (orientational) polarization, and hyperelectronic (nomadic) polarization, as observed in π-conjugated systems. The fifth type of polarization known as interfacial or Maxwell-Wagner polarization depends upon the marcoscopic structure of the matter.

A. Electronic polarization   Electronic polarization is a universal polarization response and arises from a slight distortion of electronic distribution with respect to the positive nucleus of any atom. The displacement is quite small, due to the high intra-atomic field at an electron due to the nucleus (in the order of 10^{11} V/μm), while externally applied fields seldom exceed 10^8 V/μm. The dipole moment induced in the atom was shown to be $(4\pi\varepsilon_0 R^3)E$, where R is the radius of the atom [42], and therefore the dipole moment is proprtional to the applied field. In most organic solids, the electronic polarization leads to a relative permittivity ε_{r} of about 1.8-4. In inorganic solids, especially those of the heavy elements with higher electronic density, higher values are observed. For example, the electronic polarization contribution in an element such as silicon ($\varepsilon_{\text{r}} = 12$) is higher than that of elemental carbon as diamond ($\varepsilon_{\text{r}} = 5.5$).

B. Atomic polarization   This type of polarization arises from the distortion of the arrangement of atomic nuclei in a molecule. In most organic solids where ions are absent, this type of polarization makes a minor contribution (usually 1/10 of the electronic polarization). The contribution due to the atomic polarization can be evaluated and separated from the contribution of electronic polarization by comparing the permittivity obtained at different frequencies. The movement of heavy nucei is more sluggish than that of electrons, therefore the atomic polarization occurs at lower frequencies ($\sim 10^{12}$ Hz) compared to that of the electronic polarization ($\sim 10^{14}$ Hz). In the case of inorganic solids, the magnitude of atomic polarization can be larger. For example, in an ionic solid NaCl, the positive sodium ions (Na^+) move relative to the negatively charged chloride ions (Cl^-) when subjected to an external electric field which gives a rise to ε_r of 6.12. For inorganic solids with non symetric arangements of positive and negative centers the effect can be quite sizable. For example, in a metal oxide TiO_2, particularly the rutile form, the titanium atom is surrounded by an octahedron of oxygen sites. Atomic polarization arising from a displacement of the center of the Ti^{4+} cation relative to the O^{2-} ions leads to a relative permittivity of 170 [43]. A similar type of displacement, that gives rise to remarkably high relative permittivity is found in metal oxides with a general composition of ABO_3, such as $BaTiO_3$. The crystal structrure of these materials is known as a perovskite structure "loose ion in a cage" and is schematically shown in Fig. 2.3.

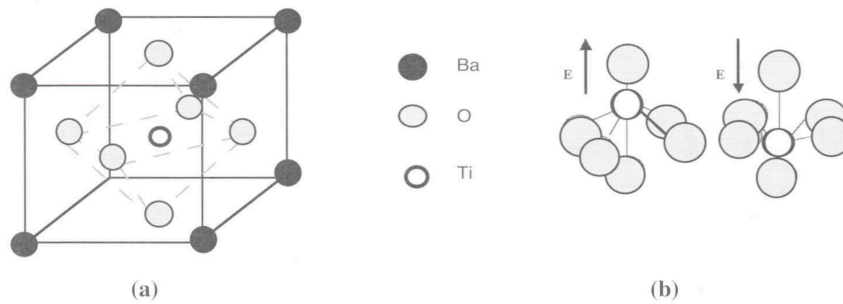
Figure 2.3: The perovskite structure of $BaTiO_3$: a) the cubic phase (at T>120 °C) b) schematic ilustration of dipole switching upon application of electric field (adapted from [44]).

The perovskite $BaTiO_3$ has a permittivity of ~ 3000. The origin of the remarkably high permittivity is a phenomenon known as *spontaneous polarization.* The unit cell of $BaTiO_3$ is cubic at high temperatures, and undergoes a cubic/tertragonal transition at approximately ~ 120 °C, a temperature known as Curie temperature [45]. In the cubic phase (above 120 °C), the Ti^{4+} and Ba^{2+} cations are located at the centers of the oxygen cage, while in the polar (tetragonal) phase (below 120 °C) the cations are displace relative to the O^{2-} ions, leading to the formation of a spontaneous (existing in the absense of electric field) electric dipole. The directions of the displacement of the cations in reference to the oxygen can be switched by the electric field in such a way that upon removal of the field the dipole stays in the new orientation (Fig. 2.3(b)). The characteristics of having spontaneous polarization, and the ability to reverse the direction of polarization with an external electric field is specifically called *ferroelectricity.*

C. Orientational polarization   The presence of molecular groups having atoms of different electronegativity leads to the formation of permanent dipole moments. If these molecules are independent of each other, and hence free to rotate in the field, there is a tendency for the molecules to realign as the electric field is applied, thereby reducing their potential energy. Examples of such dipolar molecules are H_2O, HF, and chlorebenzene. Rotational polarization also arises from the rotation of pendant polar groups such as

-OH or -CO. Liquid water has a permittivity of about 80 at a frequency below 19 GHz, however it falls to about 1.8 at optical frequencies, where the molecular dipoles can no longer follow the applied electric field. Orientational polarization of electrical dipoles is mainly limited to liquids, due to the weak bonding between the molecules, however it can be observed also in some polymers, e.g. poly(vinylchloride) and poly(vinylidene fluoride) PVDF. PVDF is a well known ferroelectric polymer, which due to its high inherent spontaneous polarization exhibits relatively high permittivity $\varepsilon_r \sim 15$ compared to common polymers ($\varepsilon_r \leq 5$). Its ferroelectricity originates from molecular dipoles associated with positively charged hydrogen atoms and negatively charge fluorine atoms (Fig. 2.4(a)).
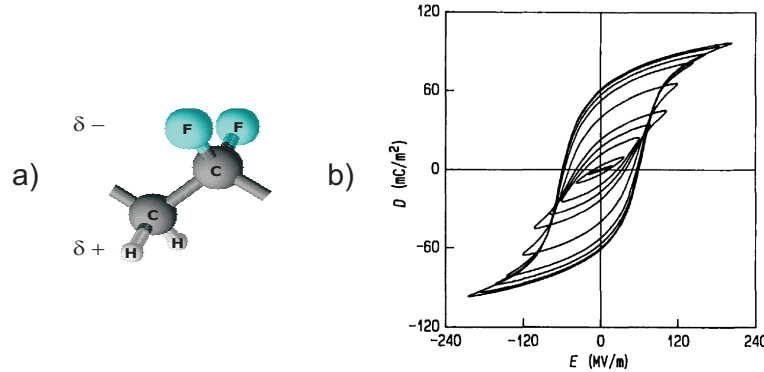

Figure 2.4: Molecular structure of PVDF repeating unit (a) and hysteresis loop of PVDF (adapted from [46]) (b)).

Ferroelectricity implies a polarization hysteresis behavior associated with reversal of the spontaneous polarization. A typical hysteresis D-E loop for PVDF is shown in Fig. 2.4(b). As the electric field strength is increased, the dipoles start to align in a positive direction giving rise to a rapid increase in the polarization. At very high field levels, the polarization reaches a saturation value. Switching the orientation of the electric field, flips the direction of the polarization and hence a hysteresis loop is observed. The electric field needed to reduce the polarization to zero is called the coercive field strength.

D. Hyperelectronic (nomadic) polarization Hyperelectronic polarization arises in π-conjugated molecules, due to the displacement of charge carriers along molecularly large domains. The term hyperelectronic (nomadic) polarization was proposed by Pohl in 1965 to account for the high polarizabilities observed in some π- conjugated molecules [47]. In this type of polarization, the response to an electric field can be considered due to the pliant interaction of charge pairs of excitons, localized temporarily on long polarizable molecules. These carriers are molecularly separated, and can be displaced over extended regions of near-zero resistance of associated π-orbitals, limited in path only by the molecular boundary. Under electric field, the mobile carriers are displaced forming monopoles which gives rise to high polarizabilities [48] (schematically shown in Fig. 2.5).

As outlined by Pohl [49], the ratio of polarizabilities of the hyperelectronic to electronic can be in the order of tens of thousands. This can be shown by simple calculation as illustrated in the following. When electronic polarization occurs in an organic solid, the average displacement of the electrons to the nucleus of the atom is about 10^{-9} nm, while, in the long conjugated molecule, it can be in the order of 100-1000 nm. The atomic or molecular dipole moment generated by the field is $p = ed$, where e is the electronic charge, and d is the average displacement, and the total polarization per unit volume N, is given by $P = Ned$. The typical concentration of electrons in organic solids is $\sim 10^{24}$ cm^{-3}, and if a value of the
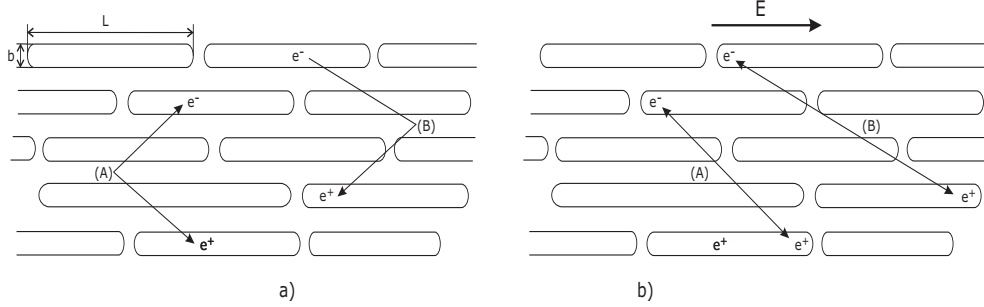
Figure 2.5: Schematic diagram of monopole (exciton and ion) formation in long π-conjugated polymers. Charge pair formed at regions (A) and (B) migrate to distant molecules of dimensions L × b. When the electric field is off (a), there is a certain amount of delocalization of the carries, but the net polarization is zero. With the field on (b) a large polarization results from the long domains in which the carriers may move (adapted from [48]).

free charges in a conjugated system of only 10^{17} cm^{-3} is assumed, then at relative displacement of 100 nm the ratio of polarizabilities is 10000.

E. Maxwell-Wagner polarization   Interfacial polarization, also known as the Maxwell-Wagner effect, arises due to the build-up of charges at the interfaces of heterogeneous systems. The four types of polarization discussed above are phenomena of molecular scale and occur when charges are locally bound in atoms or molecules. However, macroscopically the real dielectric materials always have to some extent regions of non-uniformity or impurities (e.g. cracks and defects, regions of occluded moisture) that can be regarded as a second phase. At the interface charge accumulation appear and under the electric field, these mobile charges drift through the material toward electrodes, thus contributing to an increase in the conductivity, and consequently to the relative permittivity. Since interfacial polarization is completely determined by conductivity, it is an undesirable superficial effect, which can give misleading results if not recognized. It can be easily mistaken for dipole orientational polarization, since the effect is pronounced at low frequencies. At high frequencies AC electric field, the build-up charges have insufficient time to respond and therefore the effect is absent. A summary of the frequency response of the different polarization mechanisms is given in the following paragraph. Maxwell-Wagner polarization can be very pronounced in heterogeneous systems, e.g. polymer blends, organic/inorganic composites.

F. Characteristic frequency of the polarization mechanisms   The characteristic relaxation frequency of each polarization mechanism discussed above is schematically shown in Fig. 2.6. A resonant effect due to electric oscillation is usually associated with electronic and atomic polarization with resonant frequencies of 10^{15} to 10^{14} Hz and 10^{13} to 10^{12} Hz respectively. Because the molecular dipoles have inertia, the orientational polarization is not a resonant process and therefore the response to the electric field is always retarded. The characteristic frequency for this relaxation is from 10^6 to 10^4 Hz. Hyperelectronic and Maxwell-Wagner polarizations occur at low frequency. It is important to emphasize that, hyperelectronic polarization is a phenomenon of molecular scale, in contrast to interfacial polarization which occurs at the interface of the microscopic boundaries.
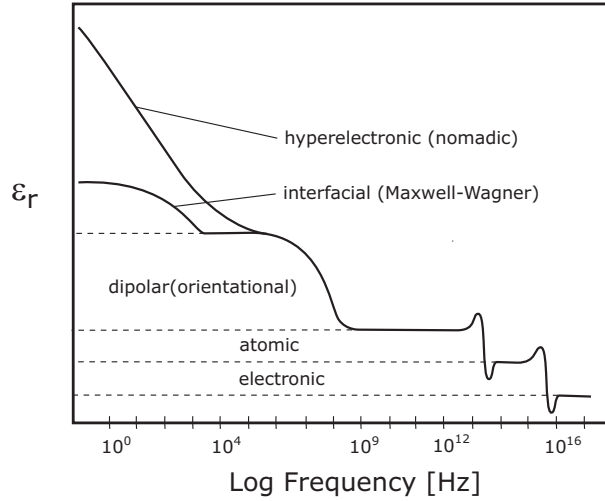
Figure 2.6: Schematic diagram of electrical polarization mechanisms and their frequency responses.

2.2.2 Dielectrics in alternating fields

Dielectric response is frequency dependent. Since no material medium can follow instantaneously the variations of the electric field, there is a delay between the polarization and the field. Jonscher [50] defines the time response to a step function field, $E(t) = 0$ for $t < 0$, $E(t) = E_0$ for $t > 0$, of the current:

$$i(t) = \frac{dP}{dt} = \varepsilon_0 E_0 f(t), \tag{2.8}$$

where $f(t)$ is the dielectric response function. The response of polarization to an arbitrarily time-varying signal $E(t)$ is given by the convolution integral:

$$P(t) = \varepsilon_0 \int_0^\infty f(\tau)E(t - \tau)d\tau \tag{2.9}$$

Fourier transformation of Eq. (2.9) gives the frequency (ω) dependence of polarization:

$$P(\omega) = \varepsilon_0 \chi(\omega)E(\omega), \tag{2.10}$$

where $P(\omega)$ and $E(\omega)$ are Fourier components of $P(t)$ and $E(t)$, respectively, and $\chi(\omega)$ is the frequency dependent susceptibility and is defined as the complex Fourier transform of $f(t)$:

$$\chi(\omega) = \chi'(\omega) - i\chi''(\omega) = \int_0^\infty f(t) \exp(i\omega t)dt, \tag{2.11}$$

where $i = (-1)^{1/2}$. The real component χ' gives the component of polarization in phase with the field, the imaginary component χ'' gives the quadrature component, known as dielectric loss. χ' and χ'' are interrelated, and as shown by Jonscher [51] they are Hilbert transforms of each other, known in this context as the Kramers-Kronig relations. One very important consequence of these relations is that a mechanism leading to a strong polarization must inevitably give rise to correspondingly high losses

19

somewhere in the frequency spectrum. In a field of peak amplitude E_0, the energy loss is $\varepsilon_0 \chi''(\omega) E_0^2 / 2$ and the power loss is $\sigma(\omega) E_0^2 / 2$, and therefore the alternating current (ac) conductivity is defined as:

$$\sigma(\omega) \propto \varepsilon_0 \omega \chi''(\omega) \qquad (2.12)$$

2.2.2.1 Jonscher universal law

On the basis of experimentally observed similarity of the $\omega - \chi''$ curves for a large number of dielectric solids, Jonscher has proposed an universal pattern in which the frequency dependence of the dielectric loss follows the empirical law, known as Universal Dielectric Response (UDR) [52]:

$$\chi''(\omega) \propto \omega^{n-1} \text{ with } 0 < n < 1 \qquad (2.13)$$

The universal response applies to permanent dipoles and hopping carriers of electronic, polaronic and ionic nature. Jonscher states that UDR

> "... is valid in solids with covalent, ionic and molecular bonds, in single crystals, polycrystalline and amorphous structures, and therefore independent of the structure of the material."

The frequency dependence of the electrical conductivity can be represented by:

$$\sigma(\omega) \propto \omega^n \qquad (2.14)$$

2.2.2.2 Complex relative permittivity and dielectric loss

The dielectric function $f(t)$ in time domain and the complex frequency domain function $\chi(\omega)$ represent the basic interpretational analysis on experimental data. However, starting from this fundamental level there are various options to present the data. For example, it could be more appropriate in some cases to plot the frequency dependent permittivity $\varepsilon'(\omega)$ instead of $\chi'(\omega)$ or the frequency dependent conductivity $\sigma(\omega)$ instead of dielectric loss $\chi''(\omega)$.

It is convenient to study relaxation processes by measuring the real and imaginary components of the permittivity over a range of frequencies. The permittivity is related to the susceptibility, and also can be expressed in terms of the real and imaginary components:

$$\varepsilon(\omega) = \varepsilon^* = \varepsilon' - i\varepsilon'' \qquad (2.15)$$

The meaning of the real and imaginary parts may be better understood by considering a parallel-plate capacitor with a dielectric material between the plates (Fig. 2.7(a)). In an ideal dielectric, the current which flows in the external circuit after application of an alternating voltage with amplitude V_0 given by $V = V_0 \cos\omega t$ leads the voltage by 90° and there is no component of the current in phase with the voltage. However, if a real dielectric is placed between the plates, due to the polarization mechanism described above the current phasor will be not in phase with the voltage but by an angle (90°-δ), where δ is a phase lag, known as the *loss angle* (Fig. 2.7(b)):
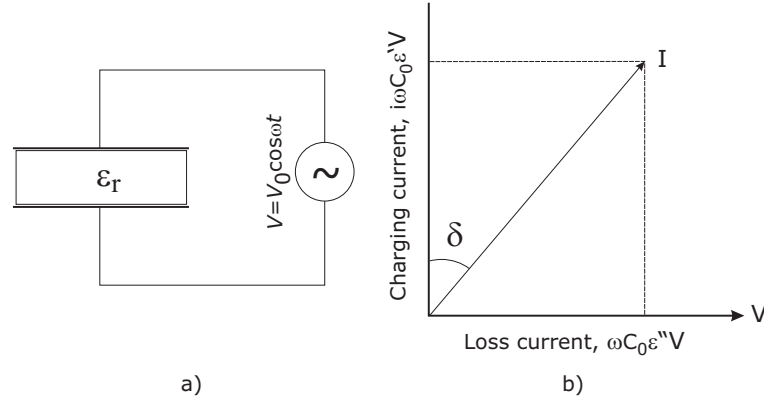
Figure 2.7: AC losses in a dielectric: a) circuit diagram, b) the phasor diagram of a current (adapted from [53]).

$$I = I_0 \cos \left[\omega t + (\frac{\pi}{2} - \delta) \right],$$ (2.16)

where

$$I_0 = \omega C_0 \varepsilon(\omega) V_0$$ (2.17)

The current can be resolved into two components: the component leading the applied voltage by 90°, known as a capacitive component of the current,

$$I_c = i\omega C_0 \varepsilon' V$$ (2.18)

and a resistive component, which is in phase with the voltage

$$I_r = \omega C_0 \varepsilon'' V$$ (2.19)

Work can only be done by the capacitive component and the resistive component gives rise to dielectric loss. The loss angle δ is given by:

$$\tan \delta = \frac{\varepsilon''}{\varepsilon'} = \frac{\text{energy disipated/cycle}}{\text{energy stored/cycle}},$$ (2.20)

usually ε'' referred to as the loss factor and $\tan \delta$ the dissipation factor.

2.2.2.3   Dielectric relaxation

The simplest idealized physical model for a relaxation of a dielectric material was introduced by Debye [54]. It describes the response of a spherical and non-interacting population of molecular dipoles to an electric field, which is a very good approximation of a gas introduced between two conductive plates. The model considered the frequency dependence reorentational process of the dipoles, and introduced a relaxation time τ at a certain frequency after which the dipoles are not able to follow the alternating field. The complex permittivity of the Debye function can be expressed as:

$$\varepsilon(\omega) = \frac{\varepsilon_{\mathrm{s}} - \varepsilon_{\infty}}{1 + i\omega\tau} + \varepsilon_{\infty}, \tag{2.21}$$

where ε_{s} and ε_{∞} are the static and unrelaxed permittivity at the high frequency limit, respectively. The complex permittivity can be separated into real and imaginary part:

$$\varepsilon' = \frac{\varepsilon_{\mathrm{s}} - \varepsilon_{\infty}}{1 + \omega^2\tau^2} + \varepsilon_{\infty} \text{ and } \varepsilon'' = \frac{\varepsilon_{\mathrm{s}} - \varepsilon_{\infty}}{1 + \omega^2\tau^2}\omega\tau \tag{2.22}$$

Debye's equation describes a symmetric loss peak, whereas in reality the measured shape of the dielectric loss spectrum ε'' is broad and asymmetric. In fact, the Debye response is seldom seen, as the real systems contain dense populations of interacting dipoles. To account for the interaction of the dipoles, different empirical formulas based on the Debye model have been developed by Cole-Cole [55], Davidson [56], Havriliak and Negami [57] with a general formula given by:

$$\varepsilon(\omega) = \frac{\varepsilon_{\mathrm{s}} - \varepsilon_{\infty}}{[1 + (i\omega\tau)^{\alpha}]^{\beta}} + \varepsilon_{\infty}, \tag{2.23}$$

where α and β are fitting parameters describing the symmetric and asymmetric broadening of the loss peak.

- $\alpha = \beta = 1$ - the Debye model is recovered

- $0 < \alpha < 1$ and $\beta = 1$ - Cole-Cole equation (amorphous solids and certain polymers)

- $\alpha = 1$ and $0 < \beta < 1$ - Davidson-Cole equation (liquids and polymer solutions)

- $0 < \alpha < 1$ and $0 < \beta < 1$ - Havriliak- Negami equation (gives the complete phenomenological description of a relaxation process)

In addition, in heterogeneous (composite) materials, a strong increase in the dielectric loss ε'' at low frequency may be observed due to conductivity (σ_{dc}). The conductivity term can be added to Eq. (2.23), leading to

$$\varepsilon(\omega) = \varepsilon_{\infty} + \frac{\varepsilon_{\mathrm{s}} - \varepsilon_{\infty}}{[1 + (i\omega\tau)^{\alpha}]^{\beta}} + \frac{\sigma_{\mathrm{dc}}}{j\varepsilon_0\omega} \tag{2.24}$$

The values of the α, β and σ_{dc} can be obtained by performing a least squares fit of Havriliak-Negami (HN) function known as HN analysis.

2.3 Electrostatic stress in compliant capacitors

The electrostatic energy density of the electric field $u = \frac{1}{2}\varepsilon_{\mathrm{r}}\varepsilon_0 E^2$ stored in the compliant capacitor can be expressed as an electric energy per unit volume:

$$U = uAt = \frac{1}{2}\varepsilon_{\mathrm{r}}\varepsilon_0 V^2 \frac{A}{t} = \frac{1}{2}CV^2, \tag{2.25}$$

where A is the area, t is the thickness, C is the capacitance and V is the voltage. The force between the electrodes is given by:

$$f = -\frac{dU}{dt}$$

The change in stored electrostatic energy dU for a change dt in thickness and dA in area can be derived by the differentiation of the energy:

$$dU = \frac{\varepsilon_r \varepsilon_0 V^2}{2} d(\frac{A}{t}) = \frac{\varepsilon_r \varepsilon_0 V^2}{2}(\frac{1}{t}dA - \frac{A}{t^2}dt) \tag{2.26}$$

From the mechanical constraints, which are related to the volume incompressibility of the ideal elastic material during deformation $At = const$ follows:

$$tdA + Adt = 0 \iff \frac{dA}{A} = -\frac{dt}{t} \tag{2.27}$$

Replacing dA with $-A\frac{dt}{t}$ in Eq. (2.26) yield

$$dU = -\frac{\varepsilon_r \varepsilon_0 V^2}{2} 2\frac{A}{t^2}dt = -\varepsilon_r \varepsilon_0 (\frac{V}{t})^2 A dt = -\varepsilon_r \varepsilon_0 E^2 A dt \tag{2.28}$$

The electrostatic pressure (Maxwell stress) exerted into the material can be written as:

$$p = \frac{f}{A} = -\frac{\frac{dU}{dt}}{A} = \varepsilon_r \varepsilon_0 E^2 \tag{2.29}$$

The derived equation is very similar to the equation describing the stress on the surface of a dielectric in an electric field $p = \frac{1}{2}\varepsilon_r \varepsilon_0 E^2$. The doubling of the stress in a compliant capacitor originates from the softness of the electrodes allowing deformation in a direction perpendicular to the electric field.

2.3.1 Electro-mechanical instability

Subject to high voltages, a soft elastomer deforms from initial thickness d_0 to thickness d due to the induced electrostatic stress given by $p = \varepsilon_r \varepsilon_0 E^2$ as described above. Electrostatic stress driven deformation is balanced by the mechanical stress as shown by Zhao and Suo [58]:

$$\sigma_E = \sigma_H \tag{2.30}$$

When the function of the voltage reaches maximum, the electromechanical instability occurs causing an electric breakdown. Based on that consideration, the authors developed an electromechanical instability breakdown model, for a semicrystalline polymers covered with compliant electrodes and subject to a voltage Φ and a biaxial force P in the plane, which simulates the conditions of a pre-strain elastomer under electric field:

$$\sigma_L + \sigma_E = \sigma_H \Rightarrow \frac{P}{HL\sqrt{\lambda}} + \varepsilon\left(\frac{\Phi}{H\lambda}\right) = K(-\ln\lambda)^N, \tag{2.31}$$
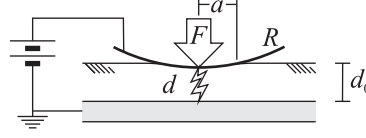
Figure 2.8: Schematic of breakdown experiment with spherical electrode (adapted from [59]).

where H is the polymer thickness and sides L×L in undeformed state, λ is the deformation ratio and N and K are parameters used to fit experimentally recorded stress-stain relation. Based on this relation, the authors calculated the critical conditions for the electromechanical instability and related them to the following two special cases: necking and pull-in instability.

Recently, Kollosche and Kofod [59] investigated electrical failure in very soft elastomers, as a function of their elastic properties. They described the electromechanical instability failure as it occurs in a standard breakdown experiment configuration. The breakdown experiment is sketched in Fig. 2.8, where a spherical electrode indenter with radius of curvature R is pushed with a force F_L into a soft material of initial thickness d_0. The model proposed by the authors, includes the effects of load, hemi-spherical boundary conditions and the Neo-Hookean constitutive model describing the mechanical stress. The model is based on the balancing of the boundary load σ_L, electrostatic σ_E and hyperelastic stresses σ_H as proposed by Zhao and Suo. The load stress corresponds to the load force F_L on the circular contact area $\pi a^2 = \pi(R^2 - (R - (1-\lambda)d_0)^2) \approx 2\pi R d_0(1-\lambda)$. The electrical stress is given by $\frac{1}{2}\varepsilon_r\varepsilon_0 E^2$, due to the stiff metal electrode boundary conditions. Application of the Eq. (2.31) results in the following equation, for the critical thickness and electric field at instability:

$$\frac{F_L}{2\pi R d_0(1-\lambda)} + \frac{\varepsilon_r\varepsilon_0}{2\lambda^2}\left(\frac{\Phi_C}{d_0}\right)^2 = -\frac{Y}{3}\left(\lambda^2 - \frac{1}{\lambda}\right) \tag{2.32}$$

Differentiation by λ and setting $\partial_\lambda\Phi_C = 0$ results in:

$$\frac{F_L}{2\pi R d_0(1-\lambda)^2} - \frac{\varepsilon_r\varepsilon_0}{\lambda^3}\left(\frac{\Phi_C}{d_0}\right)^2 = -\frac{Y}{3}\left(2\lambda + \frac{1}{\lambda^2}\right), \tag{2.33}$$

These equations can be solved simultaneously, resulting in a measured electric breakdown strength, defined as $\frac{\Phi_c}{d_0}$, and the critical stretch at breakdown λ_c. The model was found to describe soft elastomers with varying elastic modulus ($Y = 156 - 320$ kPa) convincingly.

2.3.2 Isotonic and isometric transverse stress and strain

The electro-mechanical coupling of dielectric elastomer planar actuator was described theoretically by Carpi et al. [60], in terms of electrically induced transverse stress, in both isotonic (i.e. at constant load) and isometric (i.e. at constant length) conditions. A simplified (first order) analysis assuming linearly elastic, isotropic material with constant volume was used and the mechanical equilibrium of the actuator was described as:

$$S_{xx} = \frac{1}{Y}T_{xx} - \frac{1}{2Y}T_{yy} - \frac{1}{2Y}T_{zz} \tag{2.34}$$

$$S_{\text{yy}} = -\frac{1}{2Y}T_{\text{xx}} + \frac{1}{Y}T_{\text{yy}} - \frac{1}{2Y}T_{\text{zz}} \tag{2.35}$$

$$S_{\text{zz}} = -\frac{1}{2Y}T_{\text{xx}} - \frac{1}{2Y}T_{\text{yy}} + \frac{1}{Y}T_{\text{zz}}, \tag{2.36}$$

where S_{ii} and T_{ii} are the actuator strain and stress along the Cartesian axis i $(i = x, y, z)$. By applying a passive pre-stress (isotonic condition) given by $T_{\text{xx}} = $ (prestress) and electric field along the thickness direction (z) given by $T_{\text{zz}} = -p$ the equilibrium strains can be expressed as:

$$S_{\text{xx}} = \frac{1}{Y}T_{\text{xx}} + \frac{1}{2Y}p \tag{2.37}$$

$$S_{\text{yy}} = -\frac{1}{2Y} + \frac{1}{2Y}p \tag{2.38}$$

$$S_{\text{zz}} = -\frac{1}{2Y} - \frac{1}{Y}p, \tag{2.39}$$

As shown in Eq. (2.37) the active isotonic strain (actuation strain) along x direction is given by $\frac{p}{2Y}$, while the prestress-induced passive strain is $\frac{T_{\text{xx}}}{Y}$.

In the isometric conditions, similar analysis can be performed and taking into account the constrains of the both ends of the actuator ($S_{xx} = 0$) the new equilibrium condition along x can be described as:

$$0 = \frac{1}{Y}T_{\text{xx}} + \frac{1}{2Y}p \Rightarrow T_{\text{xx}} = -\frac{p}{2} \tag{2.40}$$

Eq. (2.37) and (2.40) imply that isotonic and isometric stresses have the same theoretical expression.

2.4 Dielectric properties of composites

In this section, dielectric properties of composites consisting of insulating or conducting filler particles homogeneously dispersed in a polymer matrix are theoretically described. Classical mixing rules, effective medium and percolation theories are discussed in details.

2.4.1 Polymer-Ceramic composites

In this section, analytical methods to model the effective permittivity of composites are introduced. The possible restrictions and problems related to the methods are pointed out.

2.4.1.1 Classical dielectric mixing rules

Classical dielectric mixing rules are algebraic formulas with which the effective permittivity of heterogeneous mixtures can be predicted as a function of the volume fraction of the constitute materials and their permittivities. The concept of effective, or macroscopic permittivity, implies that the heterogeneous

mixture responds to electromagnetic excitation as if it were homogeneous [61]. Since the heterogeneous material consist of inhomogeneities between the phases larger than the atomic scale, the concept applies only when the scale of the discontinuities is much smaller than the wavelength.

Using a theoretical approach to assess the effective permittivity of heterogeneous systems requires the calculation of the polarizabilities and dipole moments of the inclusions that compose the mixture. An accurate prediction of the macroscopic dielectric behavior must account for the detailed internal structure of the composite, the dielectric and shape characteristics, the volume fractions and the spatial arrangement of the different components [62].

A. Spatial arrangement rules The simplest level of prediction is based on the spatial arrangements of two immiscible components, made of an isotropic dielectric medium of permittivity ε_1 and volume fraction ν_1 filled with dielectric phase of permittivity ε_2 and volume fraction $\nu_2 = 1 - \nu_1$. There are several different ways in which two different components may occur in combination: series, parallel, impregnated, interspersed, uniformly or randomly dispersed, etc. [42]. In general, based on these spatial arrangements it is expected that the relative permittivity of the composite ε_c will be found between two extremes, the lower bound for the equivalent series connection of two materials and the upper bound for the parallel connection.

$$\varepsilon_{c,\min} = \frac{\varepsilon_1\varepsilon_2}{\varepsilon_1\nu_2 + \varepsilon_2\nu_1} \tag{2.41}$$

$$\varepsilon_{c,\max} = \varepsilon_1\nu_1 + \varepsilon_2\nu_2 \tag{2.42}$$

A further step in modeling the dielectric properties of a heterogeneous material is the Lichtenecker mixing rule [63] that can be written as:

$$\varepsilon_c^k = \varepsilon_1^k \nu_1 + \varepsilon_2^k \nu_2, \tag{2.43}$$

where k is a parameter that determines the type of mixing rule. When k = −1 the formula for dielectrics in series, Eq. (2.41) is recovered. When k = 1 the formula for parallel connection of dielectrics is obtained (Eq. (2.42)). In the case where k = 0, Lichtenecker proposed an intermediate form between the serial and parallel form called logarithmic mixing rule:

$$\ln(\varepsilon_c) = \nu_1\ln(\varepsilon_1) + \nu_2\ln(\varepsilon_2) \tag{2.44}$$

B. Maxwell-Garnett (MG) mixing rule The Maxwell-Garnett mixing rule [64], also known as the Clausius-Mossotti approximation, is one of the most widely used methods for calculating the bulk dielectric properties of inhomogeneous materials. It was one of the first successful attempts to provide an exact electromagnetic description for the response of the heterogeneous system. The Maxwell-Garnett mixing equation assumes dielectric spheres dispersed in a continuous dielectric medium. The effective permittivity can be calculated by replacing each sphere with an equivalent dipole moment and adding the contribution of all dipoles together. The dipole moment is given by:

$$p = \alpha E_L, \tag{2.45}$$

where E_L is the local electric field and α is the polarizability of the sphere.

$$\alpha = V(\varepsilon_2 - \varepsilon_1)\frac{3\varepsilon_1}{\varepsilon_2 + 2\varepsilon_1}, \tag{2.46}$$

where V is the volume of the sphere, ε_2 is the permittivity inside the sphere and ε_1 is the permittivity of the continuous dielectric medium outside of the sphere. When the polarizability of a single sphere is known, the average electric polarization density can be calculated as a function of the number density n of the spheres, $P = np$. The local field or Lorentzian field is dependent on the shape of the inclusion, and for a sphere can be written as:

$$E_\text{L} = E + \frac{1}{3\varepsilon_1}P \tag{2.47}$$

The effective permittivity ε_eff can be defined as a relation between the external field E and the average flux density D.

$$D = \varepsilon_\text{eff}E = \varepsilon_1 E + P \tag{2.48}$$

Combining Eq. (2.45) with Eq. (2.47) gives the average polarization, and then the effective permittivity can be written as:

$$\varepsilon_\text{eff} = \varepsilon_1 + \frac{n\alpha}{1 - n\alpha/3\varepsilon_1} \tag{2.49}$$

This relation is known as Clausius-Mossotti formula and often is written in the form

$$\frac{\varepsilon_\text{eff} - \varepsilon_1}{\varepsilon_\text{eff} + 2\varepsilon_1} = \frac{n\alpha}{3\varepsilon_1} \tag{2.50}$$

For practical application more useful quantities are permittivities of the components and their volume fractions $\nu = nV$. The Maxwell Garnett formula can be obtained by combining Clausius-Mossoti formula with the polarizability expression (Eq. (2.46)):

$$\varepsilon_\text{eff} = \varepsilon_1 \left[1 + \frac{3\nu_2(\varepsilon_2 - \varepsilon_1)}{2\varepsilon_1 + \varepsilon_2 - \nu_2(\varepsilon_2 - \varepsilon_1)}\right] \tag{2.51}$$

The Maxwell-Garnett approximation is an idealized model, assuming two-phase isotropic dielectric components and the inclusions are with a simple geometry. Some heterogeneous systems in the nature obey this model quite well, e.g. clouds, fog (fog is formed of spherical water droplets in air, and the mixture is diluted), however more complicated heterogeneities does not follow the assumption of that model. The disadvantage of the Maxwell-Garnett mixing rule is that it tends to underestimate the effective permittivity of random mixtures with higher filler concentrations [65, 66], because the percolation threshold is equal to 1. In the case of high dielectric contrast $\varepsilon_2/\varepsilon_1$ between the components, the formula fails to predict the effective permittivity and the value obtained for the ε_eff remains closer to the permittivity of the background until the mixture is almost completely filled with spheres.

C. Bruggeman mixing rule   Bruggeman's model [67] is an extension of the Maxwell-Garnett approximation assuming symmetry between the spherical inclusions and the continuous dielectric phase. The first term in the summation represents the polarizability of a sphere with permittivity ε_2 weighted with

the corresponding volume fraction and the second term represents the polarizability of a sphere with permittivity ε_1 weighted with the volume fraction of the continuous phase. The model assumes that the initially low volume fraction of the filler is gradually increased by infinitesimal additions and the solution of a differential equation based on Eq. (2.51), leads to the Bruggeman's mixing rule:

$$\frac{\varepsilon_2 - \varepsilon_{\text{eff}}}{\varepsilon_{\text{eff}}^{1/3}} = \frac{(1 - \nu_2)(\varepsilon_2 - \varepsilon_1)}{\varepsilon_1^{1/3}} \tag{2.52}$$

The Bruggeman formula was found to estimate reasonably well, composites consisting of high volume fraction spherical inclusions [68,69]. Limitation of the mixing rule equation is the tendency to overestimate the effective permittivity of a random mixture of spheres with small volume fraction. Experimental results obtained from similar systems have shown that the effective permittivity lies between Maxwell Garnett and Bruggeman mixing rules [66, 70]. For low mixing ratios results are closer to MG, while for higher mixing ratios they are closer to that predicted from the Bruggeman formula.

D. Yamada model Yamada [71] has investigated a binary system composed of ellipsoidal particles dispersed in a continuous dielectric medium. Considering the electrical potentials which are produced outside and inside the ellipsoidal region and introducing a shape parameter n to account for non-spherical particles the following formula was derived:

$$\varepsilon_{\text{eff}} = \varepsilon_1 \left[1 + \frac{3n\nu_2(\varepsilon_2 - \varepsilon_1)}{n\varepsilon_1 + (1 - \nu_2)(\varepsilon_2 - \varepsilon_1)} \right] \tag{2.53}$$

The shape parameter n depends on the shape of the filler particles through an elliptical integral. Assuming a spheroid with an equal semi-minor axis $a = b$ and defining the ratio between a and the major axis c as $\eta = c/a$, the shape of the particles can be be prolate ($\eta > 1$, $n > 3$), spherical ($\eta = 1$, $n = 3$) or oblate ($\eta < 1$, $n < 3$).
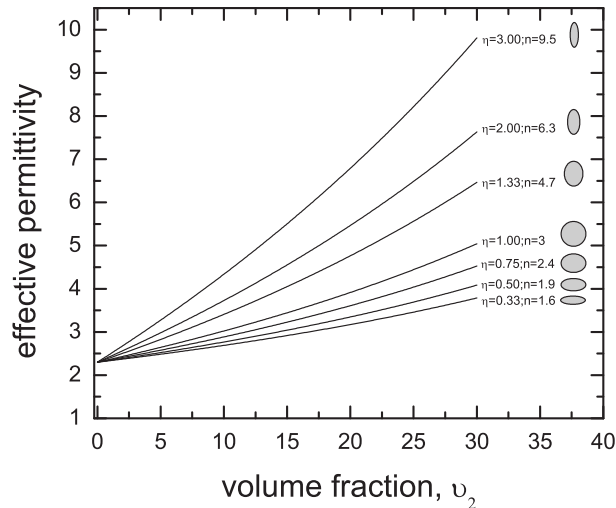

Figure 2.9: Prediction of the Yamada dielectric mixing model ($\varepsilon_1 = 2.3$ for the matrix, and $\varepsilon_2 = 128$ for the filler inclusions) plotted for different shape parameters.

Based on these considerations, the shape parameter as a function of semi-axes ratio may be solved analytically,

$$n = \frac{\eta^2 - 1}{\frac{\cos^{-1} n}{\sqrt{\eta^{-2} - 1}} - 1} \tag{2.54}$$

Fig. 2.9 represents the increase of the effective permittivity with filler volume fraction plotted for different shape parameters n. The real permittivity of the continuous dielectric medium is taken to be $\varepsilon_1 = 2.3$ and for the ellipsoidal inclusions $\varepsilon_2 = 128$, which represents the real situation for a soft elastomer filled with a high permittivity ceramic particles (e.g. TiO_2 particles). As seen, the Yamada model predicts that the shape of the particles will influence the effective permittivity strongly. For example, for prolate particles with $\eta = 3$; $n = 9.5$, the effective permittivity increases by 50% compared to spherical particles ($\eta = 1$; $n = 3$). The Yamada model have been found to describe the composite effective permittivity of different systems very well [13, 70, 72].

E. Representations and predictions of the various mixing rules

Effective permittivity prediction based on the mixing models discuss above is summarized in Fig. 2.10 (with $\varepsilon_1 = 2.3$ for the continuous dielectric medium, and $\varepsilon_2 = 128$ for the filler inclusions). The highest predicted value is for a parallel connection of the two constituents. Physically, for a composite material consisting of a soft elastomer filled with high permittivity ceramic particles, this parallel circuit representation can occur if the two materials are separating themselves in to parallel domains. The lowest predicted value is for a serial connection of the two materials, which physically could occur if the filler particles sediment completely. An intermediate form between the serial and parallel circuit representation is the Lichtenecker logarithmic mixing rule. The prediction of the classical mixing rules shown in Fig. 2.10 corresponds to the case of a perfectly random mixture of the filler inside the matrix. Maxwell-Garnett more accurately predicts composites with a low filler concentrations, while Bruggeman formula gives good estimation for higher filler concentrations. Yamada formula takes into account the shape of the filler inclusions, and can be used in a case where the particle shape differs from spherical.
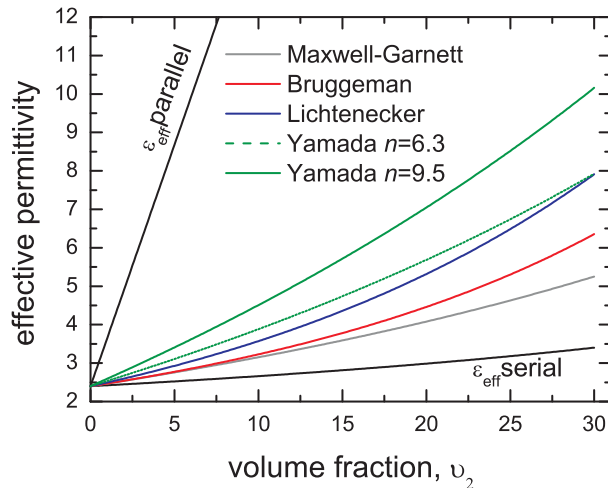

Figure 2.10: Prediction of the classical dielectric mixing models ($\varepsilon_1 = 2.3$ for the continuous dielectric medium, and $\varepsilon_2 = 128$ for the filler inclusions).

2.4.2 Electrically conductive and sub-percolative composites

The addition of conductive filler to a polymer matrix can produce electrically conductive or high permittivity composites depending on the concentration of the filler. If the amount of filler is high enough to form a continuous network through the sample, an insulator-to-conductor transition occurs and current flows through the material. Below the transition, material with high permittivity can be obtained, due to the formation of encapsulated conductive domains in the polymer matrix. This behavior can be predicted and analyzed by the percolation theory. In this section, a general percolation theory is introduced and the concept of percolation is explained with an emphasis on insulator-to-conductor transition in composites.

2.4.2.1 Percolation theory

Percolation is a standard model for disordered systems in which the disorder is defined by a random variation in the degree of connectivity. In particular, it focuses on the emergence of a critical or spanning percolating cluster that connects opposite sides of the system. The critical fraction of the component at which percolation occurs is termed the geometric percolation threshold, usually denoted as p_c.

In classical percolation theory [26, 73], the percolation concept is described based on a idealized discrete system - *lattice*. A lattice can be considered to be built up of sites and bonds, as shown in Fig. 2.11. For simplicity, consider a square lattice where each site is occupied randomly with probability p or is empty with probability $1 - p$.

bond percolation; p<p_c   bond percolation; p>p_c   site percolation; p<p_c   site percolation; p>p_c
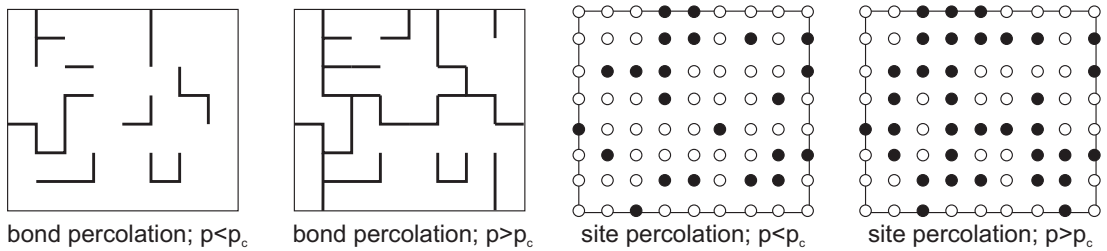
Figure 2.11: Illustration of percolation concept on a square lattice.

When p is low, the occupied sites or bonds are either isolated or form small clusters of nearest-neighbor sites. At sufficiently high p values the separated clusters interconnect to form a large cluster that connects the opposite sides of the system. The emergence of a spanning cluster occurs at a critical fraction of occupied sites or bonds known as *percolation threshold*. The percolation threshold depends on the percolation type (bond or site) and the details of the lattice, which includes dimensionality and symmetry (Table 2.1).

Table 2.1: Percolation thresholds (bond and site) for different lattices.

lattice	coordination, z	bond, p_c	site, p_c
triangular	6	0.3473	0.5000
square	4	0.5000	0.5927
hexagonal	3	0.6527	0.6962

When the dimension of the lattice is fixed, the percolation threshold p_c decreases with decreasing coordination number z. In addition to the percolation threshold, another important parameter to characterize the geometrical properties of the percolation system is the *probability P_∞* that a site or bond belongs to

the spanning cluster, and the linear size of the cluster, characterized by the *correlation length* ξ. The ξ is defined as the mean distance between the two sides of the spanning cluster and therefore represents the characteristic length of percolation.

$$P_\infty \;\propto\; |p - p_{\mathrm{c}}|^{\beta} \tag{2.55}$$

$$\xi \;\propto\; |p - p_{\mathrm{c}}|^{-\nu} \tag{2.56}$$

The exponents β, ν are known as *critical percolation exponents* and display universal scaling behavior. While p_{c} depends on the type of percolation system considered, the critical exponents are universal and independent of the lattice type and the percolation type (bond or site percolation). They depend only upon the dimensionality of the lattice. The values of β, ν are given in Table 2.2.

Table 2.2: Critical scaling exponents in two and three dimensions.

critical exponents	$d = 2$	$d = 3$
β	$5/36$	0.41
ν	$4/3$	0.88

2.4.2.2   Dielectric properties of percolating systems

Percolation theory has been mainly used to understand and predict effective transport properties, as these properties depend on the connectivity in a straightforward way. It was originally used to describe the flow of a fluid through a porous medium [74], however it can be use to describe a whole range of physical and chemical phenomena such as permeabilities of diphasic materials, sol-gel phase transitions, thermal conductivity, diffusion constants [75], and insulator-to-conductor transition in composites which is the application in this thesis.

Percolation behavior has been well-studied on an idealized lattice system, however in Nature one has often to deal with *continuum percolation*. For example, the position of the two components in heterogeneous materials, specifically composite systems, are not restricted to the discrete sites of a regular lattice. Continuum percolation, where all possible occupation positions of the phases fill the space, represents a more realistic percolation model.

In a continuous media, e.g. conductive fillers in an insulating polymer matrix, percolation theory predicts power-law dependence of the effective conductivity (σ_{eff}) and permittivity ($\varepsilon_{\mathrm{eff}}$) near the percolation threshold p_{c} (insulator-conductor transition):

$$\sigma_{\mathrm{eff}} = \sigma(p - p_{\mathrm{c}})^{t} \tag{2.57}$$

$$\varepsilon_{\mathrm{eff}} = \varepsilon(p_{\mathrm{c}} - p)^{-s} \tag{2.58}$$

where ε is the relative permittivity of the polymer matrix, σ is conductivity prefactor, s and t are critical exponents characterizing the transition, p is the fraction of the conductive filler. The conductivity prefactor is an extrapolation of the percolation law at 100% filler material. It does not necessarily equal the conductivity of the pure filler material, as the percolation law is valid only close to the percolation threshold. The exponents s and t are universal and depend only upon the dimensionality of the system. For a 3D system the universal values are $t = 2$ and $s = 1.3$ [73].
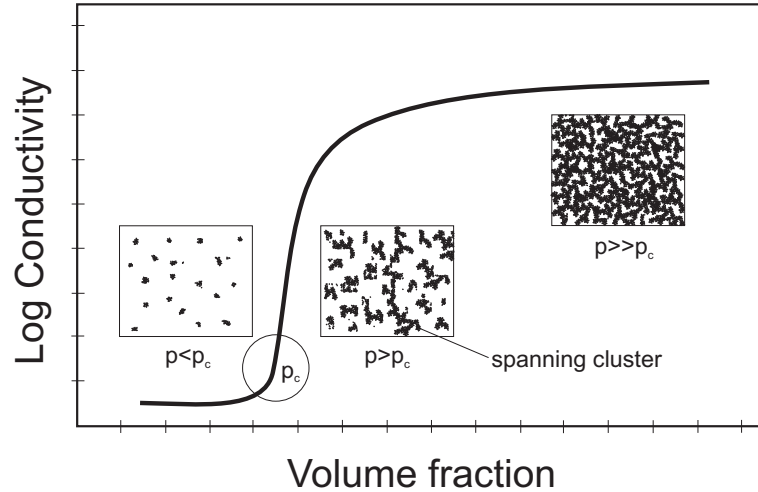
Figure 2.12: Schematic representation of predicted dependence of conductivity on the concentration of the conductive filler material in an insulating matrix.

The insulator-conductor transition is characterized by an abrupt change of conductivity of several orders of magnitude and a divergence of a real part of the relative permittivity. The reason for an abrupt increase in conductivity is the direct electrical contact between the conductive fillers spanning the sample. For low conductive filler concentrations, the filler particles are encapsulated by the insulating media and the distance between them is greater than the tunneling distance of electrons, therefore the electrical conductivity of the composite is close to that of the insulating polymer matrix. At a critical filler concentration p_c the conductivity of the composite increases rapidly. Further increase of the filler conentration leads to a formation of a network of conductive pathways and correspondingly a steady increase of electrical conductivity until it saturates and approaches that of the filler particle medium. The typical microstructures for these characteristic filler concentrations are displayed in Fig. 2.12.

According to the theory, the relative permittivity of the composite is inversely related to the difference between the actual filling volume fraction of fillers and the threshold value of percolation. Approaching the insulator-conductor transition, according to Eq. (2.58), the effective permittivity of the composites increases tremendously and could be three or four orders of magnitude higher than that of the dielectric matrix. The physical reason for the divergence is the existence of many conducting channels which randomly stretch across the length of the system and are separated only by very thin insulating barriers, thus forming a capacitor with a large area and a small thickness. Every channel of this type contributes to an abnormally large capacitance, and all of these are randomly connected in series and parallel.

Experimentally, percolation threshold and the scaling exponents s and t can be determined from ac measurements of the complex permittivity and conductivity and application of the scaling equations (Eq. (2.57), Eq. (2.58)).

The percolation threshold in heterogeneous materials is strongly dependent on particle shape and orientation. It has been shown, both theoretically and experimentally, that the percolation threshold depends on the aspect ratio (length/diameter) of the filler [76, 77]. Munson-McGee [76] estimated the critical concentration of cylinders necessary for the formation of a three-dimensional percolation network based on statistical arguments. The geometry and the state of orientation were taken into account and was shown, that for randomly dispersed cylinders the percolation threshold is strongly dependent by the value of the aspect ratio and can vary from less than 1 % when the aspect ratio is close to 1000, to more than

20 % when the aspect ratio is less than 10. Garboczi et al. [78] considered an idealized material built up from freely overlapping ellipsoids (ranging from the extreme oblate limit of platelike particles to the extreme prolate limit of needlelike particles) and derived the following equation for the p_c:

$$p_c \sim 0.6 \frac{d}{L},\tag{2.59}$$

where d and L are the diameter and the length respectively. Based on these predictions, it can be concluded that one-dimensional nanostructures are ideal fillers for conductive composites (e.g. carbon nanotubes), due to their high aspect ratios.

A. Universal scaling relations for the ac-conductivity and complex permittivity   The frequency dependent dielectric response of a percolative system near the threshold exhibits power law behaviour that can be written in the following form [79]:

$$\sigma'(\omega, p = p_c) \propto \omega^x \tag{2.60}$$

$$\varepsilon'(\omega, p = p_c) \propto \omega^{-y} \tag{2.61}$$

where $x + y = 1$. The exponents x and y can be related to the critical percolation exponents in the following way [80]:

$$x = \frac{t}{2\nu - \beta + t}, \qquad y = \frac{2\nu - \beta}{2\nu - \beta + t} \tag{2.62}$$

$$x = \frac{t}{s + t}, \qquad y = \frac{s}{s + t} \tag{2.63}$$

Derivation of Eq. (2.62) is based on a model describing the anomalous diffusion of the charge carriers in the clusters [81], while Eq. (2.63) on the intercluster polarization model [82,83]. As seen, Eq. (2.62) converges in Eq. (2.63) if $s = 2\nu - \beta$. The universal value of the loss angle δ has been found to be constant with frequency at the percolation threshold (below the characteristic frequency $\omega_p = \frac{\sigma}{\varepsilon_0 \varepsilon}$) and to depend only on dimensionality of the system.

$$\delta = \frac{\pi}{2} \frac{s}{s + t} \tag{2.64}$$

Almond [84,85] proposed a resistance-capacitance ($R - C$) percolation model, which was found to predict the complex dielectric response acurately. The model analyzed the two component percolative system in terms of a network of idealized resistors and capacitors. Since the typical percolative composite consists of microscopic conducting particles dispersed homogeneously into an insulating matrix, it is argued that a suitable representation is a randomly connected network of resistors and capacitors in which the connectivity between the components is equally likely to be in series or parallel (schematic representation in Fig. 2.13). In an equivalent circuit of such a network the complex conductivity, which is given by the net admittance, can be characterized using Lichtenecker's rule:

$$\log(Y_{net}) = \alpha_c \log(Y_1) + (1 - \alpha_c) \log(Y_2) \iff Y_{net} = Y_1^{\alpha_c} Y_2^{(1-\alpha_c)}, \tag{2.65}$$
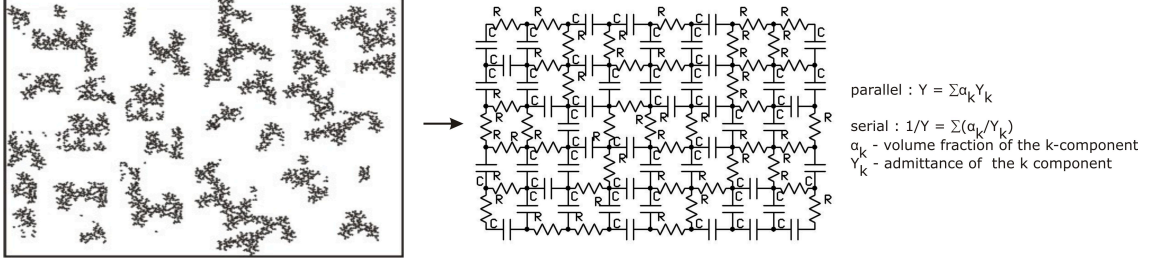
Figure 2.13: Conductor-insulator percolative system as a randomly connected network of resistors and capacitors.

where α_c is the fraction of capacitors with admittance $Y_1 = i\omega C$ and $(1 - \alpha_c)$ is the fraction of resistors with admittance $Y_2 = 1/R$. The network complex conductivity and capacitance can be expressed as

$$\sigma^* = Y_{\text{net}} = (i\omega C)^{\alpha_c}(1/R)^{1-\alpha_c} \tag{2.66}$$

$$C^* = \frac{\sigma^*}{i\omega} \tag{2.67}$$

Eq. (2.66) and (2.67) can be solved for experimentally measurable parameters: the real part of the conductivity and relative permittivity

$$\sigma' = (\omega\varepsilon\varepsilon_0)^{\alpha_c}(\sigma)^{1-\alpha_c}\cos(\alpha_c\pi/2) \tag{2.68}$$

$$\varepsilon' = (\omega\varepsilon_0)^{\alpha_c-1}\varepsilon^{\alpha_c}(\sigma)^{1-\alpha_c}\sin(\alpha_c\pi/2), \tag{2.69}$$

where σ is the conductivity of the conducting phase, ε is the relative permittivity of dielectric phase. Eq. (2.68) and (2.69) predict the frequency dependent part of the spectra. The general form of the equations, taking into account the contributions from the frequency independent response, can be written as [79]:

$$\sigma(\omega) = \sigma_{\text{dc}} + B\omega^{\alpha_c} \tag{2.70}$$

$$\varepsilon(\omega) = D\omega^{\alpha_c-1} + \varepsilon_\infty, \tag{2.71}$$

where B and D represent frequency independent prefactors from the upper equations, σ_{dc} represents the dc conductivity of the system, and ε_∞ represents the permittivity at high frequencies. Eq. (2.70) and (2.71) demonstrate that the power law exponent n in the Jonscher UDR (see section 2.2.1, Eq. (2.13) and (2.14)) is directly related to the volume fraction of the dielectric phase in a heterogenous conductor-insulator system.

Chapter 3

Materials

3.1 Introduction

In the following chapter, the structure and the basic properties of the various materials used in this study are discussed. The thermoplastic elastomer and its mechanism of crosslinking is detailed. Both insulating and conducting nanofiller particles are described. Finally, the properties of the conjugated polymer material employed are discussed.

3.2 Thermoplastic block copolymers

Thermoplastic elastomers (TPE) are class of materials that combines the processing characteristics of thermoplastics with the physical properties of the vulcanized rubbers [86]. This fortunate combination of properties is due to the phase-separated structure of the materials. TPE's are made by copolymerization of two or more monomers, using either block or graft polymerization techniques. One of the monomers develops the soft or amorphous segment, which contributes the rubbery characteristics, while the other monomer develops the hard, or crystalline segment with high glass transition temperature that functions as a thermally stable component. It is essential that the hard and soft blocks are immiscible at a molecular level so that the hard blocks form separate domains in the rubber matrix, which will act as physical crosslinks. During processing, at elevated temperatures (above the glass transition temperature) or in the presence of a solvent, the hard areas soften. After cooling or solvent evaporation, the hard domains re-form and harden, locking the elastomeric domains in place again. This unique combination of properties give them a significant advantage over the conventional thermosets in which the crosslink is a covalent bond created during the irreversible chemical reaction known as the vulcanization process. From a practical point of view, TPE's are an excellent class of materials allowing the adjustment of mechanical properties via a change in composition. Their properties can be controlled by varying the ratio of the monomers and the lengths of the hard and soft segments. There are six main thermoplastic elastomer groups found commercially [86]: styrenic block copolymers, polyolefin blends (TPOs), elastomeric alloys, thermoplastic polyurethanes (TPUs), thermoplastic copolyesters and thermoplastic polyamides. In the representative work, thermoplastic styrenic block copolymers were used and are discussed in detais in the following subsection.
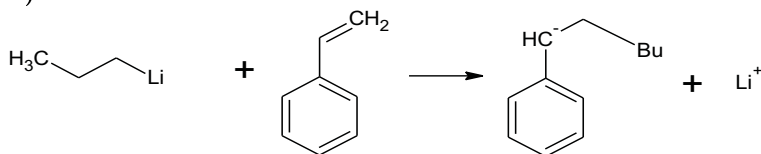
3.2.1 Styrenic block copolymers

Styrenic Block Copolymers (SBCs) are the largest-volume category of thermoplastic elastomers. Annual consumption is about 1.200.000 metric ton [86]. SBCs consist of at least three blocks, namely two hard polystyrene end blocks and one soft, elastomeric (polybutadiene, polyisoprene, either or not hydrogenated) midblock. The inclusion of butadiene or isoprene influences the properties of the end product. Because of the chemical incompatibility of the polystyrene end-block and the polydiene mid-block, phase separation occurs on a microscopic scale, causing the polystyrene blocks to form separate domains in the rubber matrix. These domains act as physical crosslinks, providing the material with rubber-like qualities.

3.2.1.1 Chemistry of styrenic block copolymers

Styrenic Block Copolymers are synthesized by "living" anionic polymerization with an organometallic catalyst, such as butyllithium, as initiator [87]. Anionic "living" polymerization allows precise control of the ratio of the monomers and the lengths of the hard and soft segments and thereby control of the properties of the end product. The anionic polymerization mechanism of poly(styrene-butadiene-styrene)(SBS) block copolymer is presented in Fig. 3.1. The first step known as initiation is an activation reaction between the styrene and the organometallic catalyst, leading to an active radical, poly(styryl)-lithium (often said to be "living") that can initiate polymerization of styrene.

1) Initiation
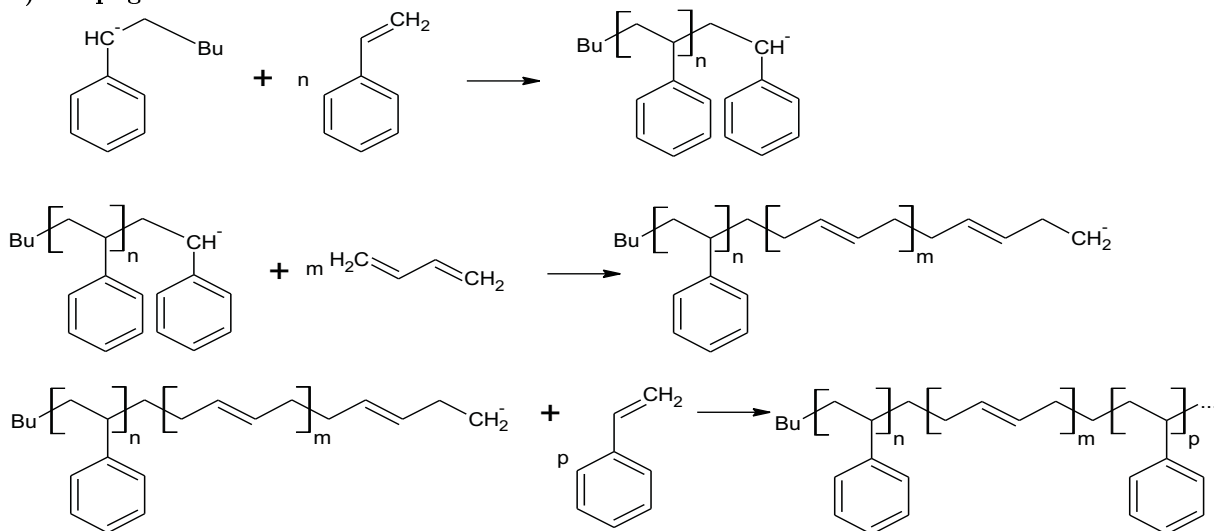
2) Propagation

Figure 3.1: Anionic polymerization of styrene-butadiene-styrene block copolymer.

The addition of new styrene monomers results in polymerization on the "living" end of the polymer chain and a subsequent increase in the length of the existing chains, a step known as propagation. The polymerization process can be precisely controlled, due to the non-terminating "living" end of every

polymer chain. Molar mass is determined by the monomer to initiator mole ratio. After the styrene monomers are consumed, diene monomers are added to the mixture, leading to a polymerization of the soft segment of the block copolymer. Finally, styrene monomers are added to polymerize the second styrene hard segment. When this reaction is complete, the product $S - B - S^- Li^+$ can be inactivated by the addition of a protonating species such as alcohol. This will terminate the reaction $S - B - S^- Li^+ + ROH \rightarrow S - B - SH + ROLi$.

The only three common monomers that are easy to polymerize using this process are styrene, butadiene and isoprene. Therefore only two block copolymers are produced on a commercial scale, namely poly(styrene-butadiene-styrene) SBS and poly(styrene-isoprene-styrene) SIS. In both cases, the elastomer segments contain one double bond per molecule of original monomer. Double bond reactivity limits stability of the copolymer. In order to improve stability, micro structure modifiers are added, and as a result the polybutadiene midsegment is produced as a random mixture of two structural forms, the (1,4) and (1,2) isomers [86]. Double bond saturation by hydrogenation leads to a polymer that is essentially a copolymer of ethylene-butylene (EB) (Fig. 3.2).
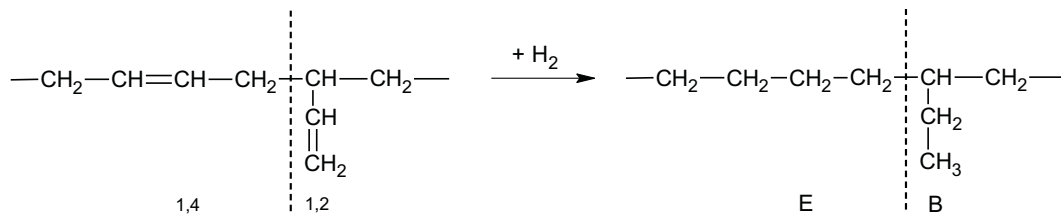

Figure 3.2: Hydrogenation of butadiene isomers.

Similarly, polyisoprene elastomer segments can be hydrogenated to give ethylene-propylene (EP) copolymers. The resultant SEBS and SEPS elastomers have excellent weather, heat-induced aging, and chemical (acid, alkali and alcohol) resistance [86].

In this work, three different styrenic block copolymers were used; SEBS-Dryflex 500040 (SEBS4, $\rho = 930$ kg/m^3), SEBS-Dryflex 500120 (SEBS12, $\rho = 930$ kg/m^3) produced by VTC Elastoteknik AB − Sweden and Kraton FG (SEBS-g-MA, $\rho = 930$ kg/m^3) produced by Kraton Polymers US LLC.
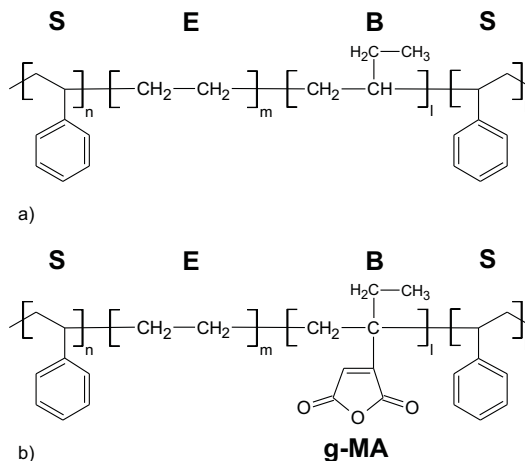

Figure 3.3: Chemical formulas of a) SEBS and b) SEBS grafted with maleic anhydride (MA).

SEBS4 and SEBS12 thermoplastic elastomers have the identical chemical structure (Fig. 3.3 a)), but the different molar mass of the styrene hard segments leads to a difference in mechanical properties. SEBS4

is a very soft elastomer with an elastic modulus of $Y = 116$ kPa, while SEBS12 has a higher elastic modulus ($Y = 556$ kPa) and respectively a higher content of styrene. SEBS-g-MA is functionalized with 1.0 to 1.7 wt. % maleic anhydride (MA) grafted to the middle block (Fig. 3.3 b)).

3.3   Titanium Dioxide (TiO₂)

Titanium dioxide, also called titania, is one of the most widely used oxides in the chemical industry. Its various applications range from its use in solar cells, in the production of hydrogen and electric energy, as a gas sensor, as a support for metal clusters in catalysis, as white pigment in paints, in cosmetic products, etc. TiO_2 occurs in Nature in three different forms which, in order of abundance, are rutile, anatase, and brookite. Besides these three polymorphs found in nature, additional high-pressure forms have been synthesized: columbite, baddeleyite, fluorite, pyrite and cotunnite [88]. Among all polymorphs, rutile and anatase are mostly manufactured in chemical industry as microcrystalline materials.

Fig. 3.4 shows the bulk unit cell of rutile and anatase form of TiO_2. The two polymorphs are based on interconnected TiO_6 octahedra, but their linkages and degree of edge and face sharing differ. Anatase can be regarded to be built-up from octahedrals that are connected by their vertices; in rutile, the edges are connected. While rutile crystals are readily available, anatase crystals are more difficult to obtain. The reason is that anatase is a metastable phase and transforms into rutile at temperatures between 780-1180 K, depending on the sample preparation conditions. Difference in the crystal structure cause a difference in the dielectric properties. The rutile form has a higher static dielectric constant ($\varepsilon_s \sim 110$) than the anatase form ($\varepsilon_s \sim 30$). The local environment of the titanium ion in the rutile is very similar to perovskite crystals such as barium titanate ($BaTiO_3$).
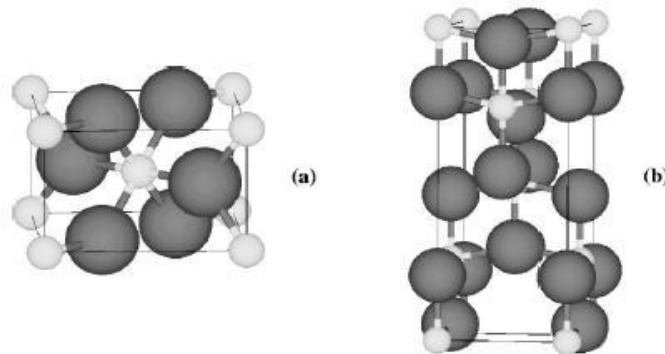

Figure 3.4: Crystal structure and bonding of TiO_2 polymorphs: rutile (a), anastase (b) (adapted from [88]). Small and large spheres represent Ti and O atoms respectively.

Each Ti_4^+ cation is completely coordinated with six O_2^- anions in an octahedral configuration. This octahedron is not regular, showing a slight orthorhombic distortion, with the distances of the titanium and the oxygen ions at the apexes of the octahedron. Owing to that distortion, the rutile titanate shows anisotropic dielectric properties, with static dielectric properties of 86 along the axes a and b and 170 along c [43].

In this study, 300 nm rutile TiO_2 (R 320 D, Sachtleben Chemie GmbH, Germany) were used. The TiO_2 particles have a density of $\rho = 4200$ kg/m³ and are coated with silicone oil to improve the dispersibility

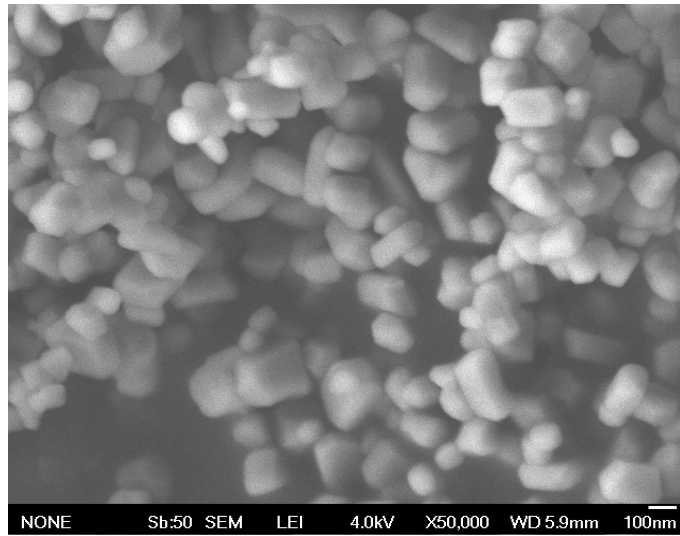and water repellency. The uncoated particles have an ellipsoid shape as revealed by the SEM image (Fig. 3.5).

Figure 3.5: Field effect scanning electron microscope (FESEM) image of rutile TiO_2 (R 320 D).

For theoretical calculations, the average value of the three spatial directions is used for the static dielectric constant ($\varepsilon_s = 128$), assuming random orientation of the TiO_2 particles inside the polymer matrix.

3.4 Carbon Black (CB)

Carbon black is a powdered form of a highly dispersed elemental carbon, similar to graphite in its microstructure. CB is manufactured by controlled vapour-phase pyrolysis of hydrocarbons and contains over 97 to 99% elemental carbon. There are a number of different types of carbon black, produced by different industrial processes, including acetylene black, channel black, furnace black, lamp black and thermal black [89]. Most of the world's CB is produced by the oil furnace process. In the oil furnace reactor, a flame is produced from air and natural gas. The carbon black feedstock is atomized into the flame and the carbon black formation takes place. As a result, carbon black particles have fractal morphology. They are composed of primary particles about 30 nm in diameter which irreversibly fuse during the furnace/combustion process to produce primary aggregates between 150-500 nm in diameter. At sufficiently high carbon black content, the aggregates can form a gel as the tenuous network structure formed by the agglomeration of particles. These agglomerates can be broken down using shear forces or ultrasonic treatment, so the primary aggregates are the smallest ultimate dispersible unit of carbon black. Carbon black is a good conductor of electricity, due to the hexagonal arrangement of the carbon atoms, with sp^2 double bonding between them resulting in a delocalized π- system. Own to this fact, CB is widely used as a conductive filler, being mixed in plastics, elastomers, paints, adhesives, films, and pastes. Carbon blacks with percolation thresholds of 5-50 % are available commercially. Changing the reactor geometry, relative flow of air, gas, and feedstock or the position of the water quench, produces grades of CB with different morphology which has an influence on the percolation threshold.

Ketjenblack®️ EC-300J produced by Akzo Nobel was used in this study. Due to the specific morphology, percolation threshold is substantially lower in comparison to conventional carbon blacks. The filler

particles have average primary size of around 30 nm and surface area of 795 m^2/g (BET). The appearance is powder-like and black, the material is supplied as little nodules of 2 mm in diameter, with much dust in between.

3.5 Conjugated polymers

The essential structural characteristic of all conjugated polymers is their π-system, extending over a large number of monomer units. The extensive delocalization of electrons is known to be responsible for an array of remarkable characteristics such as electro-optical behavior, electronic conductivity, etc. The unique feature of these materials is their combination of the processability and outstanding mechanical characteristics of polymers with the readily-tailored electrical, optical, and magnetic properties of functional organic molecules. In particular, the potential use of these materials in light-emitting diodes, field-effect transistors, photovoltaic cells, and other opto-electronic devices has motivated the development of synthesis and processing methods of conjugated polymer materials with unique properties.

3.5.1 Polyaniline (PANI)

Polyaniline is synthesized by an oxidation of aniline that can be performed either electrochemically or chemically. PANI is unique because it is easily synthesized, is environmentally stable, and possesses a simple doping/dedoping chemistry. PANI can occur in a number of oxidation states, which can be fully or partially oxidized forms. The chemical structure of the main forms are shown in Fig. 3.6. The different states range from the fully reduced leucoemeraldine (in which the nitrogen atoms are amines) to the fully oxidized form, pernigraniline (in which the nitrogen atoms are imines). The half oxidized form - emeraldine, contains an equal number of amine and imine units.
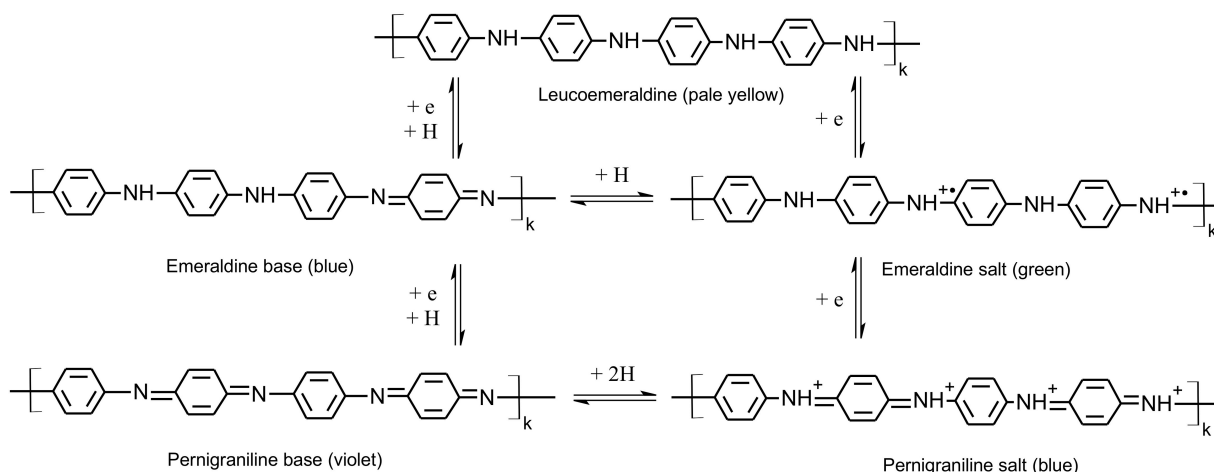
Figure 3.6: Interconversion of the main oxidation and protonated states of PANI.

PANI can be converted from the semiconducting emeraldine base form to the conducting emeraldine salt form by charge-transfer doping or protonation. The process of charge carriers generation is called protonic acid doping, and it is this simple doping/dedoping process that makes PANI so unique. The solubility of the emeraldine salt is poor in common solvents, but it can be increased by protonation with sulphonic

acids with long alkyl chains, e.g. dodecylbenzenesulfonic acid (DBSA). Excess amounts of DBSA both dope and plasticize the emeraldine base [90].

In this work, a commercial toluene based solution of conductive emeraldine salt doped with DBSA (Panipol-T, Panipol Oy, Finland) was used. PANI has a density of 1240 kg/m^3 and conductivity in the range of 10^2 S/cm [91]. The Panipol-T is a π-conjugated soft polymer able to form thermoreversible gels, which shows mechanical behavior close to ideal rubber elasticity [92].

Chapter 4

Experimental techniques

In this chapter, the sample preparation methods and the experimental techniques used to characterize the electro-mechanical properties of the developed nanocomposites are described.

4.1 Preparation of composite solutions

A common problem for preparation of nanocomposites is the agglomeration and consequent sedimentation of the filler. In this section, the experimental strategies to overcome this problem and prepare homogeneous nanocomposite dispersions are discussed.

4.1.1 Preparation of TiO$_2$ - SEBS dispersions

A stock SEBS/toluene solution was prepared by dissolving the polymer at a concentration of 100 g/L in an ultrasonic bath (Transonic digital - T490DH, Elma-Hans Schmidbauer GmbH & Co KG, Germany). The required amount of the elastomer solution was added to various weighed masses of TiO$_2$ particles to produce composite dispersions with different volume fractions. Volume percentages were used to keep track of the filler content in the final composites. The amount of TiO$_2$ was calculated using the definition of volume percentages and density formula:

$$\left.\begin{array}{l} p_{\text{TiO}_2} = \frac{V_{\text{TiO}_2}}{V_{\text{SEBS}} + V_{\text{TiO}_2}} \\[2mm] m = \rho v \end{array}\right\} \Rightarrow m_{\text{TiO}_2} = \frac{\rho_{\text{TiO}_2}}{\rho_{\text{SEBS}}} \frac{p_{\text{TiO}_2}}{1 - p_{\text{TiO}_2}} m_{\text{SEBS}} \tag{4.1}$$

where m is the mass, ρ is the density, V is the volume and p_{TiO_2} is the volume fraction of TiO$_2$. To disperse the TiO$_2$ particles each of the prepared composite solutions were sonicated with an ultrasonic tip (High intensity ultrasonic processor - Vibracell 75041, Sonics & Materials Inc., USA) for 5 min and then further sonicated in an ultrasonic bath for 2 h in order to homogenize the mixture. Immediately before drop-casting the films, the dispersions were again sonicated with the ultrasonic tip for 5 mins.

4.1.2 Preparation of CB-SEBS dispersions

The preparation procedure of CB-SEBS dispersion is similar to that of the TiO$_2$-SEBS composite dispersion. A composite stock solution consisting of 7 %vol CB was prepared using ultrasonication as described

above and then diluted in a series of steps by addition of polymer solution and sonicating each dilution with the ultrasonic tip to provide a range of CB volume fractions.

4.1.3   Preparation of PANI - SEBS-g-MA dispersions

A predetermined amount of SEBS-g-MA was dissolved in toluene (50 g/L) and mixed with different volume fractions of the conjugated conductive polymer Panipol-T, which is a commercial toluene based solution of PANI doped with dodecyl benzene sulphonic acid. A chemical reaction between the secondary amine group of PANI and the maleic anhydride of SEBS-g-MA results in grafting of PANI onto the SEBS-g-MA backbone. Green solutions stable over months were obtained, indicating a stable grafting reaction.

4.2   Preparation of composite films

Composite thin films ($\approx$ 40 μm) for electromechanical characterization were prepared as follows using the drop-casting technique. For electrical characterization, 1 ml of the ultrasonicated mixture is pipetted out of its vial and then cast on a cleaned glass slide with dimensions 37.5 $\times$ 25 mm. For mechanical characterization, the amount of dispersion was doubled (2 ml) and cast on a glass slide with dimensions 75 $\times$ 25 mm. In order to promote formation of smooth surfaces, the rate of solvent evaporation was controlled by covering the glass slides with a specially designed plastic cover. All polymer dispersions (except TiO$_2$-SEBS) were dried at room temperature for 24 hours and then stored at 50 ˚C in an oven for several days in order to remove completely the residual solvent. TiO$_2$-SEBS dispersions were dried at 50 ˚C in order to increase the rate of evaporation and promote fast film formation. This step was necessary due to the high difference in densities between SEBS ($\rho = 930$ kg m^{-3}) and TiO$_2$ ($\rho = 4200$ kg m^{-3}) leading to sedimentation of TiO$_2$ particles.

4.3   Electrical characterization

A description of the experimental techniques used to characterize the electrical properties of the composites follows now. The necessary sample fabrication steps are outlined, and the setups for the electrical breakdown test and impedance spectroscopy are discussed.

4.3.1   Sample preparation for dielectric characterization

Samples with a parallel plate capacitor configuration were required for the dielectric measurements. For this purpose, 50 nm thick aluminum metal electrodes with diameter of 20 mm were evaporated on cleaned glass slides with dimension of 37.5 $\times$ 25 mm using a physical vapor deposition technique (EDWARDS FL 400 / AUTO 306). A mask with a pattern shown in Fig. 4.1(a) was used for the evaporation. The composite dispersion was drop-cast onto the Al-electrode covered glass slide to form a thin uniform film (Fig. 4.1(b)). To make electrical contact to the bottom electrode, the edge of a composite film was peeled of and a thin copper wire was glued with a silver paste to the end of the rectangular part of the bottom electrode. For dielectric spectroscopy measurements, a metal top electrode was placed on the top (Fig. 4.1(c)). The same samples could be used for electric breakdown measurements, for which a hemispherical top electrode was used (Sec. 4.3.3).
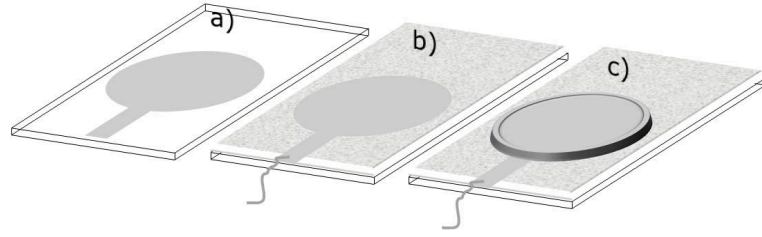
Figure 4.1: Parallel plate capacitor-fabrication steps.

4.3.2 Dielectric spectroscopy

The dielectric permittivity of the films with different contents of filler particles were measured by dielectric spectroscopy. Dielectric spectroscopy (known also as impedance spectroscopy) probes the interaction of a macroscopic sample with a time-dependent electric field. The fluctuations of local electric fields are measured which are connected to the dynamics on a molecular scale. It is a powerful technique which can be applied to wide range of materials including dielectrics, semi-conductors and composites. Dielectric spectroscopy is sensitive to the dynamics of bound charges in bulk or the mobile charges in the interfacial regions of liquids and solids. The principle of the measurement is to apply a voltage with a certain frequency to the sample $V(t) = V_0 \cos\omega t$, then measure the resulting current response $I(t) = I_0 \cos(\omega t + \delta)$, where δ is the phase difference between the voltage and the current. The applied and the measured signals are compared to obtain the complex impedance of the sample. The impedance (the frequency dependent complex resistance) can be defined as $Z = \frac{V(t)}{I(t)}$ and is represented as a complex function $Z^* = Z' - iZ''$. The complex impedance can be written both as frequency dependent capacitance or relative permittivity:

$$Z^* = \frac{1}{i\omega C^*} = \frac{d}{i\omega\varepsilon_0\varepsilon^* A} \tag{4.2}$$

The complex permittivity is related to the complex conductivity of the system by:

$$\sigma^* = i\omega\varepsilon_0\varepsilon^* \tag{4.3}$$

The experimental setup is shown in Fig. 4.2. The dielectric sample is placed in a sample holder which is directly connected to the input terminals of the impedance analyzer (Novocontrol Alpha frequency-response analyzer). The sample holder is part of a cryostat which belongs to the temperature control QUATRO cryosystem. It allows precise control of the temperature via heating and cooling with dry nitrogen gas. The impedance analyzer and the cryosystem are fully remote controlled by a personal computer.

The measuring circuit of the impedance analyzer is displayed in Fig. 4.3 in simplified form. The dielectric sample is part of an auto-balancing bridge. Potential V_1 is applied to the high terminal of the sample through the generator. Using a zero-voltage detector the potential at the sample's low terminal is detected. The zero-voltage detector adjusts the magnitude and the phase of the output V_2 of the variable amplitude-phase generator until the range-resistor current I_2 and the sample current I_1 balance, and the potential at the sample's low terminal becomes zero. The currents I_1 and I_2 can be defined as:
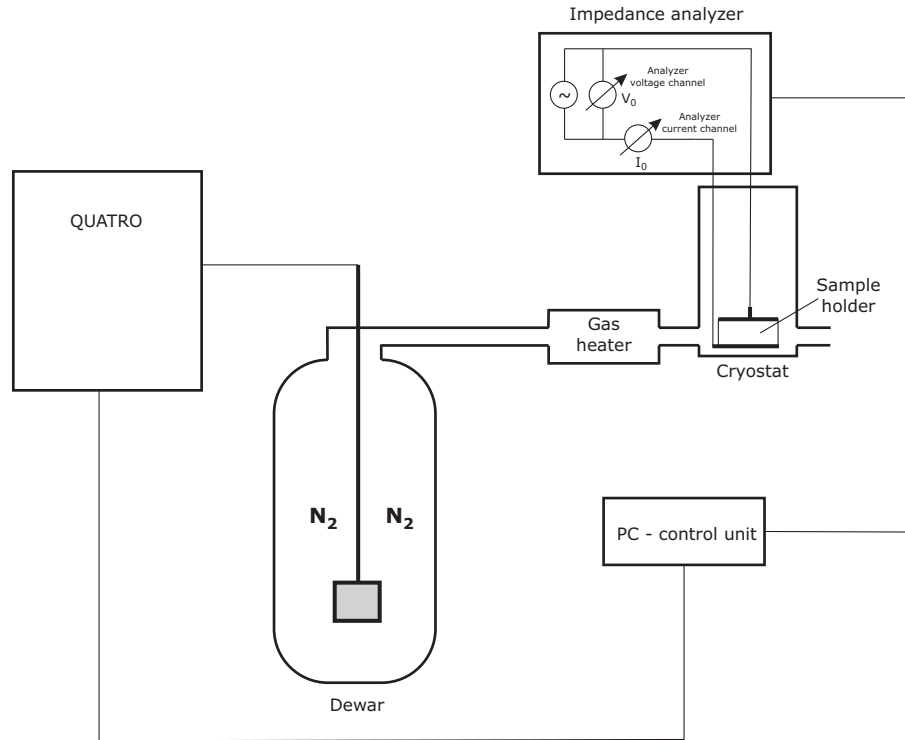
Figure 4.2: Dielectric spectroscopy - experimental setup.

$$I_1 = \frac{V_1}{Z}$$
$$I_2 = \frac{V_2}{R}$$
(4.4)

where Z is the sample's impedance and R is the resistance of the range resistor. When $I_1 = -I_2$ the impedance of the sample can be calculated as:

$$Z = -\frac{V_1}{V_2}R$$
(4.5)

The balancing operation is performed automatically over the full frequency range.
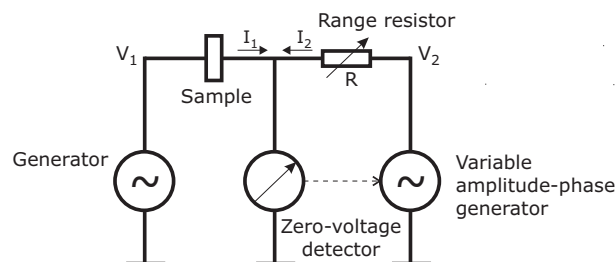

Figure 4.3: Auto-balancing bridge - simplified measuring circuit.

4.3.3   Electric breakdown test

The setup for measurement of the electric breakdown strength of a polymer film is shown in Fig. 4.4. The material under test with a configuration shown in Fig. 4.1(b) was placed on the rectangular electrode

plate and a hemispherical electrode was pressed on the top, under a load from the above electrode of 50 mN. Electric breakdown strengths were tested with a programmable high voltage generator with current monitor (HCP 35-35000, FUG Elektronik GmbH, Germany).
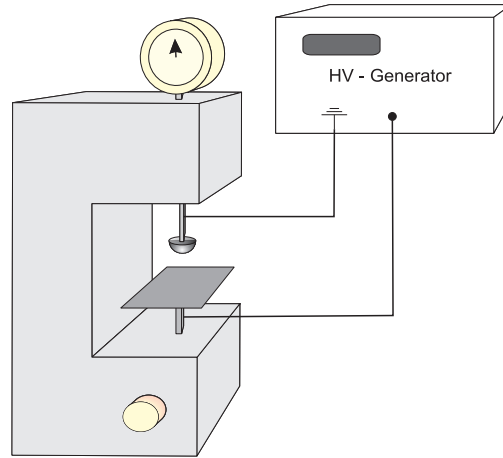

Figure 4.4: Setup for measuring the electric breakdown strength.

An increasing ramp voltage was applied to the top hemispherical electrode at a predetermined rate of 50 V/s until the sample failed. A trip current was set to 100 μA. The measurement was monitored using a computer with a program developed in a common measurement software environment (LabView 6.0, National Instruments). As a security function in case of an electric breakdown the generator is equipped with a mechanical interlock which will shield the machine against high current in case of breakdown.

4.4 Mechanical characterization

Mechanical tensile testing was performed on all materials developed in this study. Corresponding engineering stress-strain curves in uni-axial configuration were obtained. All measurements were made at a strain rate of 50 mm/min, until mechanical failure.

4.4.1 Sample preparation

Samples with uni-axial configuration were prepared for mechanical characterization by cutting them into strips with dimensions 30 x 10 mm using a laser cutter (Versa Laser, USA). Special care was taken in clamping the samples in the tensile tester, to avoid slippage. For that purpose, the strips were glued to thin plastic frames prior to clamping, for which simple tape was adequate.

4.4.2 Tensile tests

A Zwick Z005 (Zwick GmbH & Co. KG, Germany) tensile testing machine equipped with a 10 N load cell was used to measure the mechanical properties of the composites. Tensile testing is a relatively simple and accurate method where the force applied is measured as a function of the elongation of the sample. The maximum stress (force per unit area) applied to the sample before it breaks is called *ultimate tensile strength*. Another important parameter that can be derived from the stress-strain measurements is the

Young's modulus. In the region of low strain (< 5 %), the stress is proportional to the strain (relative elongation) while the slope of this elastic limit is the Young's modulus. Young's modulus is an important parameter that can be used to directly compare the mechanical properties of different materials at low strain.

4.5 Actuation experiments

The electromechanical response of the composites developed in this study was tested in a planar actuator configuration. The following section deal with the problems of handling thin elastomer films and fabrication of the actuators. The setup for actuation response measurements is presented.

4.5.1 Actuator fabrication

First, rectangular thin films with dimensions of 37.5 × 25 mm were peeled off from the glass slides. To facilitate the handling of the films during actuator manufacture, supporting plastic frames (Polyethylene terephthalate(PET), thickness 200 μm) were glued to the thin elastomer film using pressure sensitive adhesive tape (VHB^{TM}4905, 3M Deutschland GmbH). Two elastomer films were slightly stretched and clasped back-to-back and the surfaces were brushed with carbon based conducting grease. Special care was taken not to apply the conducting grease too close to the edges of the film, in order to avoid the edge arcing that will cause the failure of the actuator. Finally, thin aluminum strips were glued to the hard frames to ensure electrical connection. The hard frames were painted with a thin layer of silver paste before gluing to the film, in order to achieve a smooth transition from the leads to the carbon black based compliant electrodes (see Fig. 4.5).
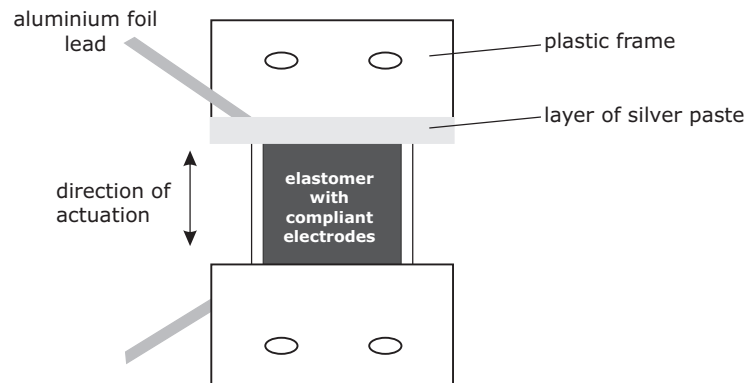
Figure 4.5: Sketch of a planar DEA actuator.

4.5.2 Setup for electromechanical response measurements

The actuator performance was tested on a Zwick Z005 with a specially developed program in a measurement software environment (testXpert® II). A high voltage amplifier (PD05031, Trek, Inc., USA) was used to apply an increasing ramp voltage at a rate of 50 V/s. Both constant force and constant strain experiments were performed [10].
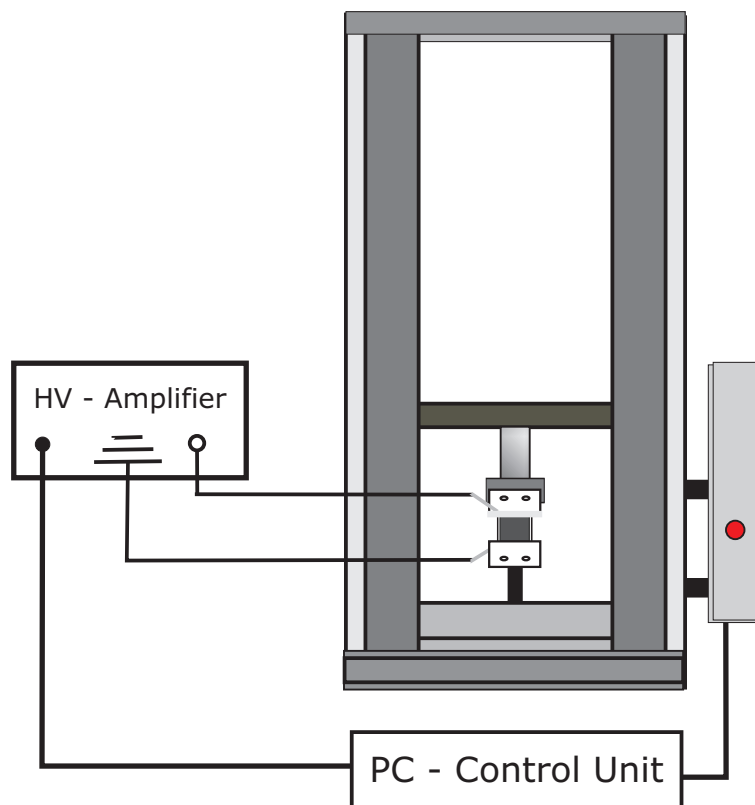
Figure 4.6: Setup for electromechanical response measurements.

4.5.2.1   Constant force

The constant force mode is known as the "hanging weight" or isotonic condition [10]. This is one of the basic actuation response experiments where a weight is hanging from an actuator, while the change of the actuator's length is measured under varying applied voltage. A hanging weight is simulated with a force feedback loop involving the translation stage and the force transducer. The feedback loop attempts to apply a constant force by comparing the current position with a constant force value from the immediately preceding data point. In this way, an estimation of the distance to the equilibrium position is made and the translation stage then moves to this position with a speed proportional to the distance from the current equilibrium position.

4.5.2.2   Constant strain

The constant strain experiment is known as the blocking force. The actuator is pre-strained to a certain level and then fixed in length. One end of the actuator is fixed to a force transducer, such that the force applied by the actuator under varying applied voltage is measured.

4.6   Infrared spectroscopy with attenuated total reflection

IR spectroscopy is a common spectroscopic technique used to identify and characterize the structure of a compound. It is based on the absorption of IR radiation of different wavelengths by a sample positioned in

the path of an IR beam. The absorbed infrared radiation is converted into energy of molecular vibration (stretching, bending). Due to the fact that different bonds and functional groups absorb infrared radiation of different wavelengths, an infrared spectrum is obtained with absorption peaks corresponding to the frequency of a vibration of a certain part of the sample molecule. The mid-infrared region (4000 cm^{-1} to 400 cm^{-1}) is used to study the vibrational energies within molecules. Molecular vibration can involve either a symmetrical and asymmetrical stretching of the bond, or a change in the bond angle, thus leading to a change in the dipole moment. One of the main advantages of IR spectroscopy is that, using various sampling accessories, a wide range of sample types such as gases, liquids, and solids can be investigated. Infrared spectrometers have been commercially available since the 1940s. At that time, prisms acting as a dispersive elements were used, but the most significant advance in infrared spectroscopy is the employment of an interferometer and the well-established mathematical process of Fourier transformation. Fourier-transform infrared (FTIR) spectrometer has dramatically improved the quality of infrared spectra and minimized the time required to obtain data [93].
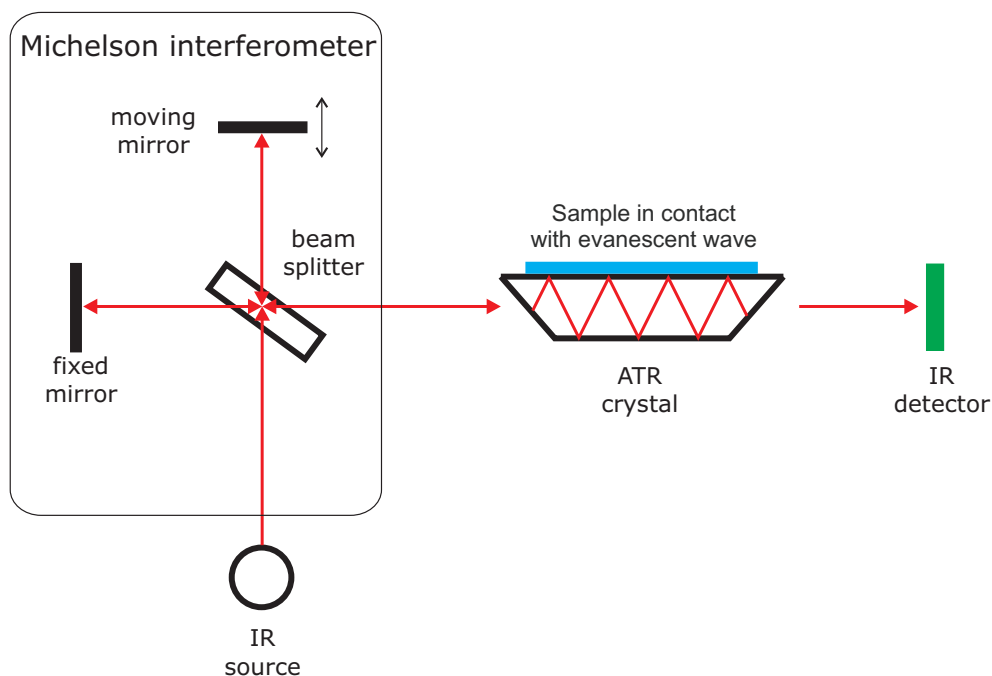

Figure 4.7: Simplified diagram of the Fourier transform infrared spectrometer (FTIR) working in attenuated total reflection (ATR) mode.

In FTIR spectroscopy, the absorption spectrum is obtained with the help of Michelson interferometer (simplified diagram shown in Fig. 4.7). The interferometer performs an optical inverse Fourier transform on the entering IR radiation. As a source of infrared radiation, SiC ceramic is usually used. The incoming light beam from the source strikes the beamsplitter, which ideally transmits one half of the radiation, and reflects the other half. Both transmitted and reflected beams strike mirrors, which reflect the two beams back to the beamsplitter. The intensity of the beam reaching the beamsplitter depends on the path difference between the beams traveling to the fixed and moving mirrors. Because of the optical path difference caused by the scanning of the moving mirror, interference occurs at the beamsplitter. The infrared radiation further goes to the sample, where the energy is either transmitted or absorbed. Finally, the beam reaches the IR detector. The interference signal measured by the detector as a function of the optical path length difference is called the interferogram. The interferogram is converted to a

spectrum by performing a Fourier transform.

Attenuated total reflection (ATR) is a sampling technique used in conjunction with a FTIR spectrometer which enables samples to be examined directly in the solid or liquid state without further preparation. An attenuated total reflection accessory operates by measuring the changes that occur in a totally internally reflected infrared beam when the beam comes into contact with a sample (indicated in Fig. 4.7). An infrared beam is directed onto an optically dense crystal with a high refractive index at a certain angle. This internal reflectance creates an evanescent wave that extends beyond the surface of the crystal into the sample held in contact with the crystal. In regions of the infrared spectrum where the sample absorbs energy, the evanescent wave will be attenuated or altered. The attenuated energy from each evanescent wave is passed back to the IR beam, which then exits the opposite end of the crystal and is passed to the detector in the IR spectrometer. Commonly used high refractive index crystals are: Zinc Selenide (ZnSe), Germanium (Ge) and Diamond.

In this study, the Platinum ATR single reflection diamond ATR module of a Bruker Alpha FTIR (Bruker Optik GmbH, Germany) was used to measure the IR spectrum of the investigated compounds.

Chapter 5

SEBS-TiO$_2$ composites

In this chapter, results obtained on a composite material are presented, made from TiO$_2$ nanoparticles and SEBS 4, as described in Sec. 4.1.1. The nanoparticles were 300 nm in diameter, and coated with silicone (PDMS, poly-dimethylsiloxane) oil to improve compatibility. Electro-mechanical measurements were performed on composites with 0, 10, 15, 20, 25 and 30 %vol of filler.

5.1 Electrical characterization

5.1.1 Dielectric characterization

Figure 5.1 displays the frequency dependent dielectric spectra (relative permittivity (left) and dielectric loss (right)) of the pure SEBS matrix and nanocomposites with different TiO$_2$ %vol in the range of 20 Hz to 10 MHz. The relative dielectric permittivity is seen to continuously increase with the volume fraction. The ε_r' of the modified dielectric is higher than the one of the pure elastomer SEBS in the whole measured frequency range. For the composites with 30 %vol, the permittivity at 100 Hz reaches a value of 8.3, which is a significant increase of 3.7 times over the pure elastomer matrix.
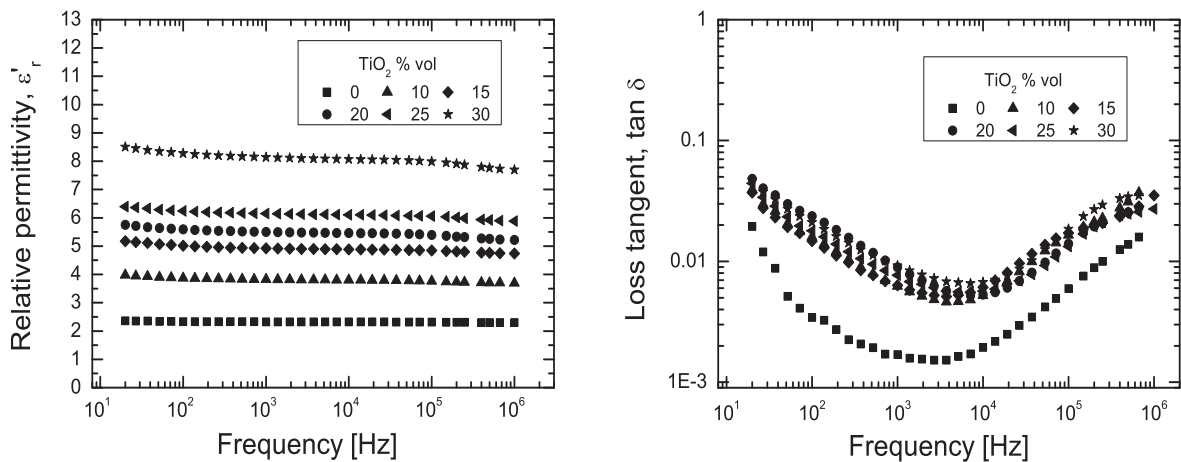

Figure 5.1: Relative dielectric permittivity (ε_r'), and dielectric loss (tan δ) as a function of frequency measured at room temperature, for varying TiO$_2$ volume fractions.

It can also be observed that the permittivity spectra of SEBS and the nanocomposites are almost frequency independent over the measured frequency range. This behavior indicates that there is no localized movement of charge within the composite. A frequency dependent contribution to the relative permittivity at low frequency is commonly observed in the literature for such metal oxide-polymer heterogeneous materials [13,94,95] due to an effect known as Maxwell-Wagner interfacial polarization (Sec. 2.2.1.1, Paragraph E). Low frequency dispersion of the relative permittivity and the dielectric loss on account of the limited flow of current caused by accumulation of charge at the polymer/filler interface does not appear in the measured dielectric spectra. This behavior could be explained as follows. The commercially available TiO$_2$ particles are coated with silicone oil to improve the dispersibility and water repellency. Possibly the thin insulating Si-O-Si layer around the particles acts as an intermediate bound layer which graduates the dielectric contrast between the matrix and the particle, thereby preventing the Maxwell-Wagner process of localized polarization. Such an approach of changing the interfacial interaction between filler and host polymer by chemical modification of the filler particles was proposed previously as being of importance for achieving high permittivity composites with low dielectric losses and high breakdown strengths [22]. The dielectric loss factor (tan δ) is slightly higher for the nanocomposites compared to the pure SEBS, which is to be expected, taking into account the heterogeneous structure of the composite. The increase of the tan δ is due to the introduction of some free charges and impurities. It is worth noticing, that the tan δ does not increase with the %vol, e.g. 20 and 30 %vol composites show almost the same loss over the whole frequency range. This is an indication that there is no charge dissipation caused by the increase of the local conductivity and therefore can be concluded that the observed increase in permittivity is caused by polarization in the polycrystalline TiO$_2$ domains.

5.1.1.1 Comparison with classical dielectric mixing rules

In the introduction on composite theories (Sec. 2.4), a number of mixing rule models have been reviewed. The measured relative permittivity of the SEBS-TiO$_2$ composites at 100 Hz was compared with theoretical values expected from Bruggeman, Lichtenecker and Yamada models. The results of the comparison are shown in Fig. 5.2.
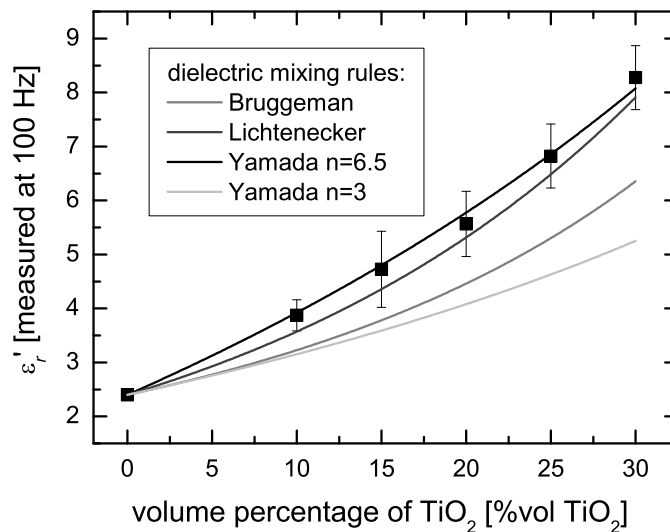

Figure 5.2: Composite relative permittivity measured at 100 Hz, for varying amounts of TiO$_2$ compared with the dielectric mixing rules.

Notably, Yamada model displays the best agreement to experimental data, which is helped by the presence of a particle shape parameter, which can be used as a free fitting parameter (Sec. 2.4.1.1). The fit shown is for a shape parameter of $n = 6.5$, which corresponds to prolate shape particles with an elliptical semi-axes ratio $\eta = 2.1$. For a comparison, the fit for $n = 3$, valid for spherical particles is shown as well. As revealed from the SEM image Fig. 3.5 (Sec. 3.3), the TiO$_2$ particles used in this study have an ellipsoid shape. The particle shape can not be considered prolate, however due to the elongated shape, one can argue that this is a reasonable approximation. Although, the particles have different size distribution, an attempt was made to calculate the semi-axes ratio of the elongated particles, giving an average value of $\eta = 2.3$, which is in a good aggreement with the Yamada fit. The Bruggeman model has shown values far bellow the experimental, although it has been shown to describe polymer-metal oxide system pretty well [69,94,95]. The reason for the discrepancy is that the model assumes spherical particles homogeneously dispersed in the composite. A reasonably good prediction is obtained from the mixing rule equation suggested by Lichtenecker. The equation is known as a logarithmic mixing rule and is an intermediate form between the two extreme levels of prediction, namely the lower bound for the equivalent series connection of two materials, and the upper bound for the parallel connection. Since this widely applicable mixing model assumes only chaotic statistical distribution of the particles, the good agreement between this model and the data indicates random distribution of particles, homogeneously throughout the entire sample volume.

5.1.2 Electric breakdown test

The results of the electric breakdown tests performed on SEBS and the 10, 20, 30 %vol TiO$_2$ nanocomposites are shown in Fig. 5.3. The values reported are the average from 25-30 independent measurements. The calculated energy density at breakdown ($\frac{1}{2}\varepsilon_0\varepsilon_r' E^2$, ε_r' at 100 Hz) is shown for the corresponding %vol in Fig. 5.3 as secondary axis (open square symbol).
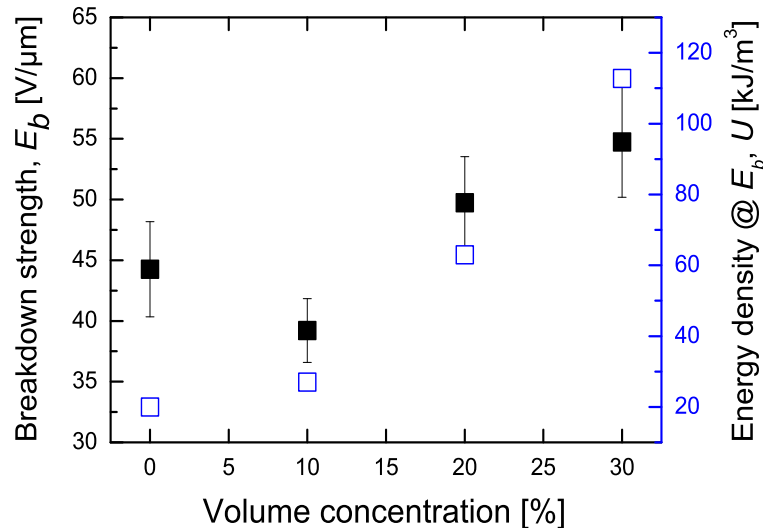
Figure 5.3: Electric breakdown strength E_b and calculated electrostatic energy density at breakdown for different TiO$_2$ %vol.

An initial drop of the electric breakdown strength is observed, followed by an increase over the polymer matrix for higher volume fractions. The inclusion of 10 %vol TiO$_2$ particles leads to a decrease of the electric breakdown strength by 11 %. For 20 %vol and above the electric breakdown strength tend to increase. As seen, at 30 %vol the breakdown strength is measured to be 54.8 V/μm, an increase over the

polymer matrix of 24 %. The electrostatic energy density at breakdown shows a steady increase with the volume fraction. At 30 %vol the energy density reaches 112.7 kJ/m^3 which is a 5.6 times increase over the elastomer matrix (20 kJ/m^3). Even for 10 %vol, an improvement in electrostatic storage ability is observed, which is due to the enhancement of dielectric permittivity balancing the observed decrease in the breakdown.

The reduction in the electric breakdown strength with the addition of small amount of metal oxide nanoparticles is not unusual. Ma et al. [96] reported that with the incorporation of 5 wt% TiO$_2$ into low density polyethylene (LDPE) the breakdown strength decreases remarkably by 40%. Khalil et al. [23] showed that addition of 1 wt% BaTiO$_3$ to the LDPE, decreases the breakdown strength by 16%. Negative impact on the breakdown strength is caused by the filler particles acting as electrical defect centers that distort and enhance the local field, resulting in reduced breakdown strength [23,24]. The field distortion is due to the difference in permittivity between the filler particles and the polymer matrix under alternating current (AC) conditions, and the difference in conductivity under direct current (DC) conditions [24]. Further, it has been shown theoretically, that when the insulating component is of nanoscopic dimensions, the internal electric field distribution will have local spots of increased electric field concentration, which reduces the electric breakdown strength of the composite [37].

To further investigate the influence of the filler particles on the nanocomposites breakdown strength, the electric current was monitored during the breakdown test (see Fig. 5.4). The pure elastomer SEBS shows a linear current-electric field curve until failure, while for all composites, the current is found to increase during the breakdown experiment, but with different current characteristics. For the pure elastomer, it is possible that the current was too low for the equipment to measure accurately, hence I will not discuss the behavior of the pure material further. Identical for all composites tested is the nonlinear electrical
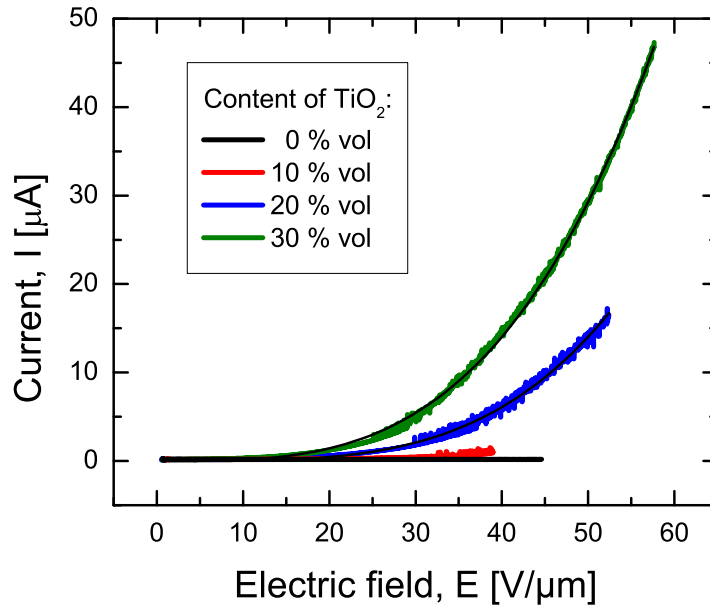
Figure 5.4: Electric current vs. electric field for varying volume concentrations (the current spike at electrical failure has been removed for clarity).

behavior: the ohmic behavior at low voltage changes to a highly nonlinear relationship for higher electric fields. Increasing the concentration of the filler particles, leads to a shift of the threshold field (above which the current increases rapidly) to lower electric fields. It should be noted that the dielectric spectra

are measured at low electric fields (0.025 V/μm), while in breakdown experiments the fields are much higher and other conduction mechanisms become important.

The observed nonlinear behavior is similar to that of well-known ZnO-based ceramic varistors, widely used for electrostatic discharge protection of electronics or for voltage surge protection in the electrical circuit [97]. The non-linear response of the ZnO particles is dictated by their grain boundaries, where the conductivity is much smaller than that of the grain interior and the Schottky barrier existing at the grain boundary contributes to the strong nonlinearity in their I–V behavior [97, 98]. Similar behavior was observed in metal oxide/polymer composites and reported in [97, 99, 100]. The voltage dependent nonlinear current observed in the investigated TiO$_2$-SEBS composite can be attributed to the tunneling of charge carriers through the intergrain and interfacial barriers at high electric fields, originating from the thin insulating elastomer layers present between the particles. At a small content of the TiO$_2$, the mean number of contacts per particle is small and the elastomer layer between the surrounding particles is relatively thick. Therefore, the probability of charge carrier tunneling is relatively small, as a result of the high potential barrier existing between the particles. As the TiO$_2$ content increases, the barrier layer between the particles decreases. Decreasing the barrier layer thickness, leads to a decrease of the potential barrier, and therefore the threshold field shifts to lower electric fields, since the charge carriers required less energy to overcome the potential barrier. The I-V characteristics of a varistor can be expressed by $I = \pm KV^{\alpha}$,where K is a geometry dependent constant and α is the nonlinear coefficient. A fit of the equation to the experimental data (shown in Fig. 5.4, black lines), yielded α values of 3.3 and 3.8 for a 30 %vol and 20 %vol respectively.

The increase of the electric breakdown strength for composites with high volume fraction of TiO$_2$ could be explained as follow. The electric breakdown in soft elastomers has been shown to be governed by electro-mechanical instability [58,59,101]. It occurs when the balance between electrical stress and internal elastic stress becomes unstable. When a thin elastomer film is subject to an electric voltage, the thickness is reduced due to the electrostatic stress, which in turns lead to a higher electric field at the same voltage, thus causing a drastic thinning of the elastomer resulting in electrical failure. Thinning of the elastomer due to electrical stress is balanced by the mechanical stress, hence strongly dependent on the Young's modulus. Kollosche and Kofod [59] developed a model describing electromechanical instability of soft elastomers in a standard breakdown experiment configuration. As described in Sec. 2.3.1 the model includes the effects of load, hemi-spherical boundary conditions, and Neo-Hookean constitutive model to account for the large deformations. Electric breakdown field E_{br}, due to electro-mechanical instability can be calculated by solving simultaneously Eq. (2.32) and (2.33). Applying the model to the experimental data gives the following values for the electric breakdown strength:

%vol	E_{br}, model	E_{br}, experimental
0	46	44
10	54	39
20	61	50
30	74	55

As seen, the model predicts accurately the pure elastomer, but the experimental values for the composites are lower than predicted. One can argue that in addition to the electromechanical instability, another mechanism plays a role. Elevated currents observed at high electric fields (Fig. 5.4) would increase the Joule heat dissipation and possibly contribute to a thermal electric breakdown. Thinning of the composite

film due to electro-mechanical instability in combination with the elevated heating leads to a breakdown due to thermal run-away. This could explain the initial drop of the electric breakdown for 10 %vol, follow by increase over the polymer matrix for higher volume fractions, e.g. 20, 30 %vol. For small volume fractions, the material remains relatively soft (e.g. $Y_{10\%vol} = 340$ kPa, see below in section 5.2), while for higher volume concentrations, e.g. 30 %vol, the composites are significantly stiffer than the pure matrix. The stiffness shifts the electro-mechanical instability to higher electric fields, but at the same time the filler particle agglomerations contribute to elevated currents and the balance between the two effects lead to the apparent increase of the breakdown strength. It is interesting to note, that the ratio between E_{br}, experimental and E_{br}, model are nearly the same for all volume fractions ≈ 0.8.

5.2 Mechanical characterization

The addition of ceramic particles to elastomer systems is expected to alter the mechanical properties of the elastomer. Approximately six samples for each volume fraction were analyzed by tensile testing, to determine the influence of the ceramic inclusions on the composite elastic properties.
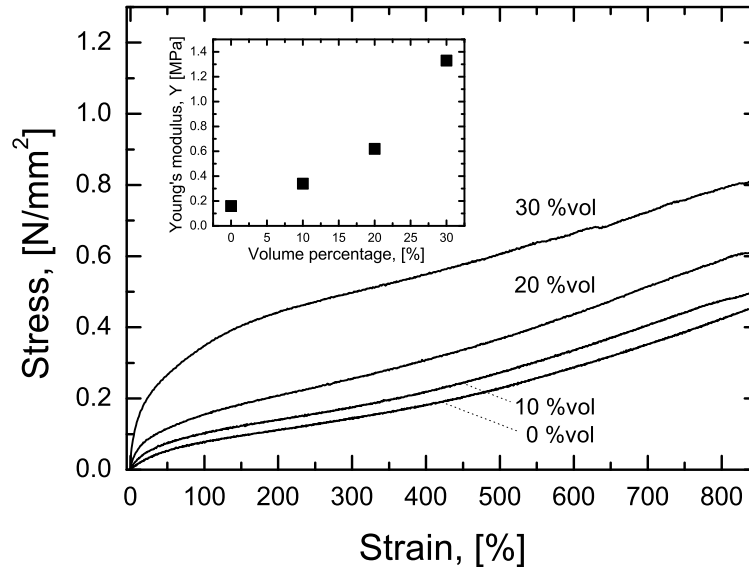

Figure 5.5: Engineering stress-strain curves for the pure elastomer SEBS and composites with different TiO$_2$ %vol.

In Fig. 5.5 the average engineering stress-strain curves from these measurements are shown. The curves present the typical non-linear trend common for rubber-like materials. For the pure elastomer, as well as for all TiO$_2$ volume fraction tested, a linear elastic behavior was observed in the region of small strains, followed by the plateau region and finally the strain hardening region with an increased slope. The Young's modulus of each sample was determined from the slope in the linear elastic region (below 5 % strain) in which Hooke's Law holds. The changes in the elastic modulus with the TiO$_2$ %vol are shown in the inset of Fig. 5.5. The high filler volume fractions required to have an impact on permittivity, deteriorate the mechanical properties of the composites. Young's modulus of the SEBS films was measured to be 160 kPa, but the addition of the TiO$_2$ particles increased Young's modulus to 620 kPa, for 20 %vol, and to 1330 kPa, for 30 %vol. This is an increasement of 5.3 and 8.3 times over the pure elastomer matrix.

Increased in mechanical stiffness is an undesired effect for dielectric elastomer materials, since it will reduce the actuation improvements due to increases in the relative permittivity.

5.3 Electro-mechanical characterization

Actuation strain of a DEA is proportional to the relative permittivity and inversely proportional to the elastic modulus and therefore an improved electromechanical response is expected from a composite material, in which the increase in relative permittivity is accompanied by low mechanical reinforcement. The two parameters can be compared by evaluating the strain sensitivity of the composite β_c with respect to the strain sensitivity of the pure elastomer β_{SEBS} using the following ratio:

$$f = \frac{\beta_c}{\beta_{\mathrm{SEBS}}} = \frac{\frac{\varepsilon_0 \varepsilon_r'}{Y_c}}{\frac{\varepsilon_0 \varepsilon_{\mathrm{SEBS}}'}{Y_{\mathrm{SEBS}}}} \Rightarrow f = \frac{\frac{\varepsilon_r'}{\varepsilon_{\mathrm{SEBS}}'}}{\frac{Y_c}{Y_{\mathrm{SEBS}}}}, \tag{5.1}$$

Composites with enhanced permittivity will be beneficial for DEA technology only if the ratio describe above is bigger than 1. The Young's modulus, relative permittivity and the ratio for the composites prepared in this work are summarized in Table 5.1. Elastic modulus at 100 % strain corresponding to the

Table 5.1: Electro-mechanical characterization.

TiO$_2$ %vol	ε_r' at 100Hz	elastic modulus at strain		f 0 %	f 100 %
		0 % [kPa]	100 % [kPa]		
0	2.3	160	120	1	1
10	4	340	160	0.82	1.31
15	4.8	430	170	0.77	1.47
20	5.8	620	230	0.65	1.32
30	8.5	1330	501	0.44	0.88

plateau region of the stress-strain curves is reported as well. It was determined as the slope of the true stress-strain curve. Engineering stress σ_{eng} given by the applied force F per unit initial (unstretched) area A_0 was converted to a true stress, $\sigma_{\mathrm{true}} = \frac{F}{A}$ as:

$$A_0 = A\lambda \quad \Rightarrow \quad \sigma_{\mathrm{true}} = \sigma_{\mathrm{eng}}\lambda,$$

where A is the cross-sectional deformed area at a given strain, λ is the deformation ratio. As seen in Table 5.1 due to the high mechanical stiffness of the composites no improvement in the electro-mechanical response is expected for all volume fractions at 0 % strain, however at 100% strain due to decrease in the elastic modulus, the figure of merit f become positive. Improvement in the electro-mechanical response is expected for composites with TiO$_2$ up to 20 %vol. Above 20 %vol, the increase in relative permittivity is not sufficient to overcome the increased stiffnes.

5.3.1 Actuation response

Planar actuators (Sec. 4.5) were prepared and the actuation response was tested at 100 % prestrain. Results are shown in Fig. 5.6. Improvement in the electromechanical response is observed for volume
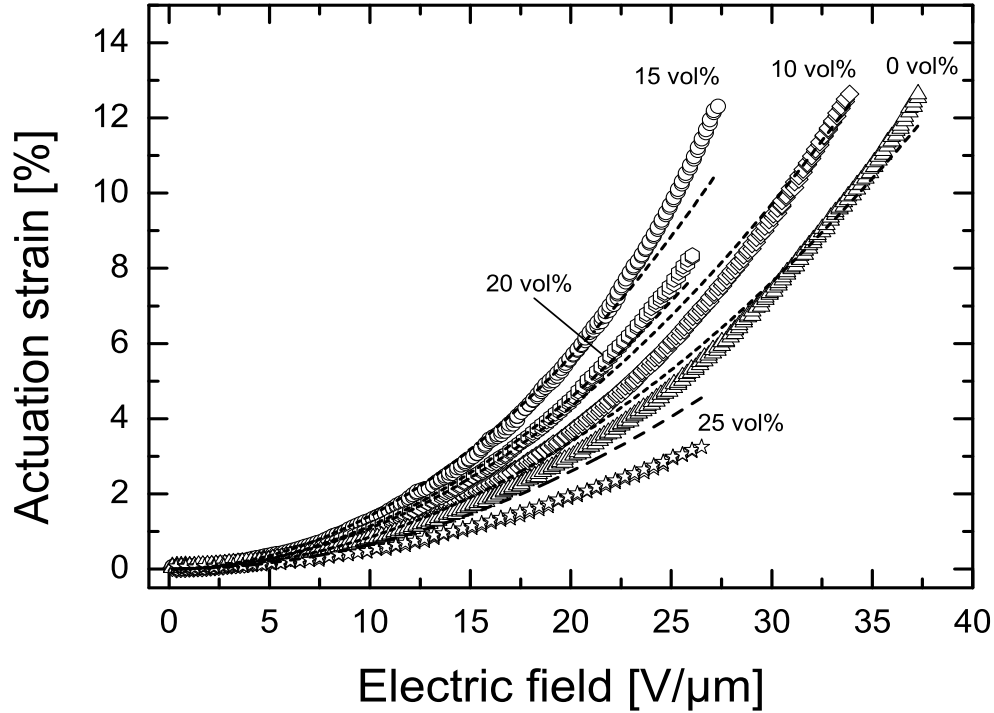
Figure 5.6: Electric-field induced strain response for the pure elastomer SEBS and TiO_2 nanocomposites with different volume fraction of TiO_2.

fractions up to 20 %vol, reaching a maximum at 15 %vol, which is in agreement with the figure of merit, f. The maximum actuation sensitivity or higher actuation strain at a given electric field is observed for a composite with 15 %vol. For example, the maximum actuation strain for this particular material is 12.3 % at 27.3 V/μm, corresponding to a 27 % reduction of the electric field compared to the pure elastomer, reaching the same strain at 37.2 V/μm. Strain sensitivity at given electric field for all the material tested was calculated from the actuation data as $\beta = S/E^2$, where S is the actuation strain. To obtain more reliable results, the actuation strains were plotted as a function of the electric fiel squared and a linear fit to the straight lines yielded the actuation sensitivity. The values for β are reported in Table 5.2 . As seen, β is strongly enhanced, from 83 nm^2/V^2 for the pure material to 150 nm^2/V^2 for the composite with 15 %vol, which is an increase of 1.8 times.

Actuators with filler content of 20 %vol and higher suffer electrical failure at low electric fields, despite the results from the electric breakdown test where electric fields higher than that for the pure elastomer were observed. The discrepancy is due to difficulties in producing and handling free standing composite films. At such high filler loadings the composites suffer degradation of mechanical properties, in terms of high weight, low flexibility and weak matrix-filler bonding. The electric breakdown test was performed on films drop-cast on glass substrates, while the electromechanical response measurements require free standing films. Peeling off of the films from the glass substrate, worsened the quality of the films and introduced localized defects such that actuators made from this material fail at lower voltages.

In order to justify that the observed actuation strain is due to the Maxwell stress, an attempt to quantify the coupling between the electrical and mechanical properties has been made. A model linking the actuation strain due to the Maxwell stress and the mechanical properties of the actuator was used [60], for detailed description see Sec. 2.3.2. Assuming linearity of the mechanical properties of the material the actuation strain S in direction perpendicular to the electric field at 100 % passive prestrain can be

obtained as:

$$S = \frac{\varepsilon_0 \varepsilon_r' E^2}{2Y} \qquad (5.2)$$

The theoretical actuation strain was calculated, using the experimental data reported in Table 5.1. The results are shown in Fig. 5.6 (dashed lines). The theoretical and experimental strain values at electric field of 25 V/μm are reported in Table 5.2 for better comparison. The model agrees reasonably well with the measured electromechanical strains, thus validating that the observed actuation strain is due to the Maxwell stress. Large variation is observed only for 25 %vol, which can be attributed to the bad quality of the film as described above. Another important parameter to evaluate the electromechanical performance of a given material is the stored elastic energy density $U_s = \frac{1}{2}YS^2$ when the elastomer is strained. The calculated values for the materials at 25 V/μm are summarized in Table 5.2.

Table 5.2: Electromechanical performance of the composites.

TiO$_2$ [%vol]	β [nm^2/V^2]	U_s at 25 V/μm [J/m^3]	S$_{exp.}$ at 25 V/μm [%]	S$_{model}$ at 25 V/μm [%]
0	83	674	4.9	5.3
10	102	1529	6.6	7.2
15	150	2073	9.9	8.9
20	116	2273	7.5	7.3
25	47	2206	2.9	4.1

5.4 Conclusion

In this study, a mixing rule approach for increasing the relative permittivity of an elastomer was investigated with respect to DEA. The results showed that dispersing high permittivity TiO$_2$ nanoparticles into a SEBS matrix leads to a substantial increase of the relative permittivity (370 %) and the corresponding electrostatic energy density (563 %). It was shown that suitable coating of the filler particles improves the interaction between the organic and inorganic phases, thus preventing the detrimental interfacial polarization causing an increase of the tan δ. A drawback of the approach is the observed up to 8-fold increase in the elastic modulus. However, it was demonstrated that with a right amount of filler and passive prestrain of the composites, an improvement of the actuation properties is possible. Improved electromechanical performances with respect to the use of pure SEBS were demonstrated up to 20 %vol. Maximum actuation sensitivity was obtained for a composite with 15 %vol, which caused a 27 % reduction of the electric field.

Chapter 6

Percolative composites with conducting particles

In this chapter a sub-percolative approach for increasing the relative permittivity and corresponding energy density of a polymer is evaluated. Advantage of it compared to the mixing rule approach is the possibility of enhancing the relative permittivity substantially above the polymer matrix at a very low volume concentration of the filler, thereby possibly preserving the valuable mechanical properties of the base polymer material. As discussed in Sec. 1.2.2.1, the effect is universally observable and it seems possible that this effect could be employed directly for enhancement of permittivity where this is required. A model system consisting of carbon black (CB) particles dispersed in SEBS matrix was investigated and increase of the relative permittivity was compared with the electric breakdown properties of the composite, in terms of calculated electrical energy density at breakdown.

6.1 Electrical characterization

6.1.1 Dielectric characterization

Figure 6.1 displays the real part of the complex ac conductivity (σ') of composites with a systematic variation of the filler volume fraction from 1 Hz to 10 MHz. The spectra are characterized by a conductivity plateau and a dispersion regime. As is typical for these systems, two cases can be distinguished: volume fraction below the insulator-conductor transition, p_c and above . Below p_c the real part of the conductivity is frequency dependent $\sigma = \omega \varepsilon_0 \varepsilon_r''$, with a slope of 1 on a log-log scale. For CB concentrations close to and greater than the percolation threshold, the conductivity is frequency independent and conductivity plateau is observed below a certain critical frequency ω_p - which increases with CB content - and above this critical frequency there is clear frequency dispersion.

The origin of the observed frequency dispersion, conductivity plateau and the corresponding shift of the critical frequency with the volume fraction can be established by considering the response of the individual composite components with the frequency. The conductivity of CB is resistive, $1/R$, i.e., frequency independent, but the conductivity (admittance) of the SEBS insulating matrix is purely capacitive and therefore frequency dependent. At a certain cross-over frequency ω_p, the resistor conductivity of CB
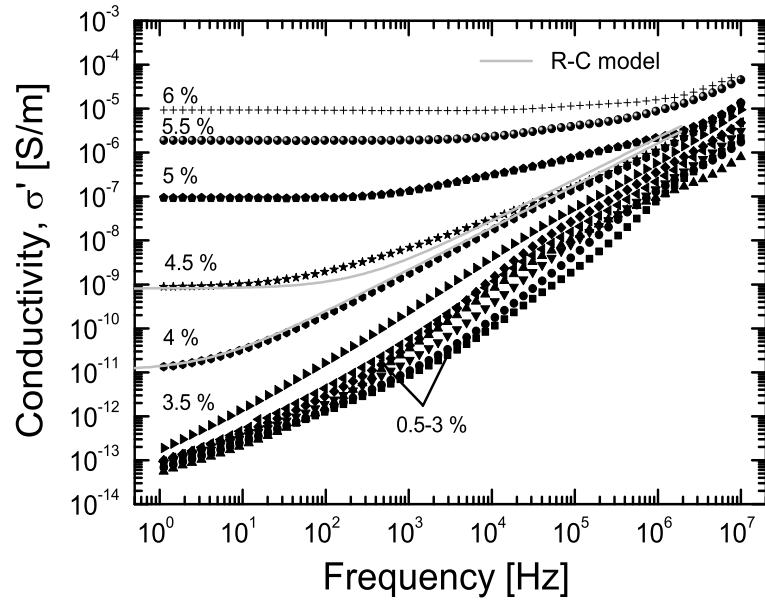
Figure 6.1: Conductivity σ' as a function of frequency measured at room temperature for varying volume concentrations.

becomes comparable to the capacitor admittance $1/R = \omega C$. Below ω_{p} the current flows through the resistor network constituted by the CB aggregates and a frequency independent plateau is observed. Above ω_{p} the SEBS admittance dominates the network response and the conductivity rises with a frequency according to the universal dielectric response (UDR) given by $\sigma(\omega) \propto \omega^n$.

In Fig. 6.2 the real part of the permittivity and the dielectric loss are shown. The permittivity spectra are characterized by a continuous increase with increasing CB filler fraction, which is in agreement with percolation theory predicting inverse relationship between the actual filling volume fraction and the threshold value of percolation.
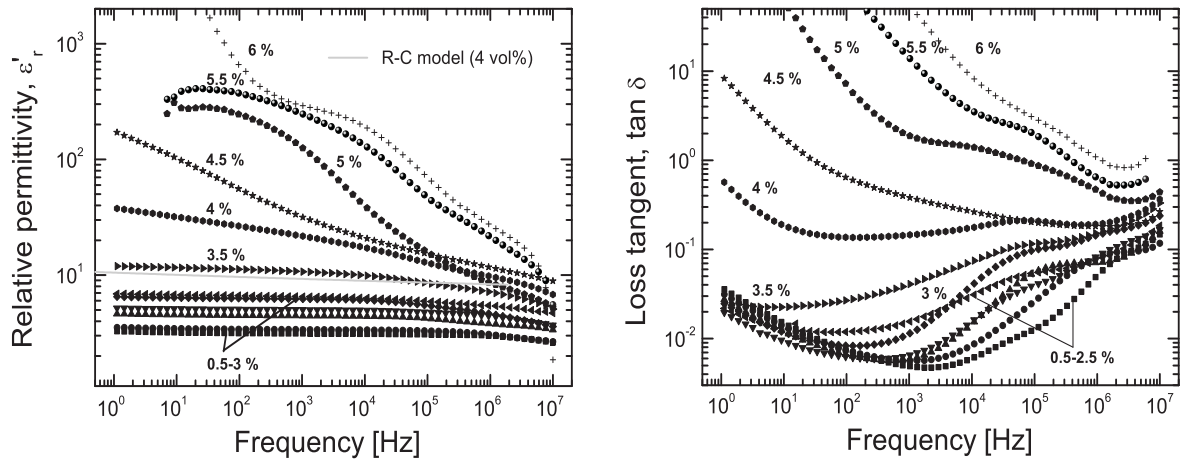
Figure 6.2: Relative permittivity $\varepsilon'_{\mathrm{r}}$ and dielectric loss $\tan \delta$ as a function of frequency measured at room temperature for different volume concentration of CB.

Up to 3.5 %vol, the permitivity spectra are seen to be flat over the measured frequency, while the dielectric losses remain very low. For example, at 3.5 %vol the $\varepsilon'_{\mathrm{r}}$ at 100 Hz is measured to be 11.2 and the tan δ=0.026. Note, that $\varepsilon'_{\mathrm{r}}$ and tan δ do not change significantly with the frequency, e.g. at 1 Hz the values

remain nearly the same. Close to the insulator-conductor transition and above the permittivity increases significantly, and the spectra begin to slope or show further large relaxations, which is reflected in the loss tangent curves displaying dramatical increases. However, still a mixing regime can be found where the increase of permittivity occurs with relative low dielectric losses. For example, at 4 %vol the permittivity of the composite reaches 27 at 100 Hz, this is an increase in permittivity of 13 times over the pure matrix ($\varepsilon'_{\mathrm{SEBS}} = 2.3$). The dielectric loss factor $\tan\delta$ at this frequency is relatively low 0.13, however a 5 times increase to 0.6 is observed at 1 Hz. It is generally argued that a $\tan\delta$ below 0.1 is acceptable for capacitive applications, however, as is demonstrated here, losses can vary substantially between 1 and 100 Hz, a frequency range important to a large range of applications. The increase of the dielectric losses at low frequency is due to the current leakage through the CB conductive network, as seen from Fig. 6.1.

The percolation threshold and the scaling exponents s and t were determined from the dielectric measurements of the real part of permittivity and conductivity and application of the scaling equations (Eq. (2.57) and (2.58)). Fig. 6.3 displays the real part of conductivity measured at 10 Hz versus the volume fraction. The best fit to the conductivity above the percolation threshold (Fig. 6.3, inset left), gives values of $p_{\mathrm{c}} = 4.75$ %vol for the percolation threshold and $t = 2.28$ for the scaling constant. In a similar way, real permittivity measured at 10 Hz was fitted below p_{c} according to the percolation law and the best fit (Fig. 6.3, inset right) was found to be for $p_{\mathrm{c}} = 4.75$ %vol and $s = 1.3$. The values for the scaling constants s and t are found to be very close to the universal value for a three-dimensional 3D lattice, reflecting the universal percolation nature of the investigated system.
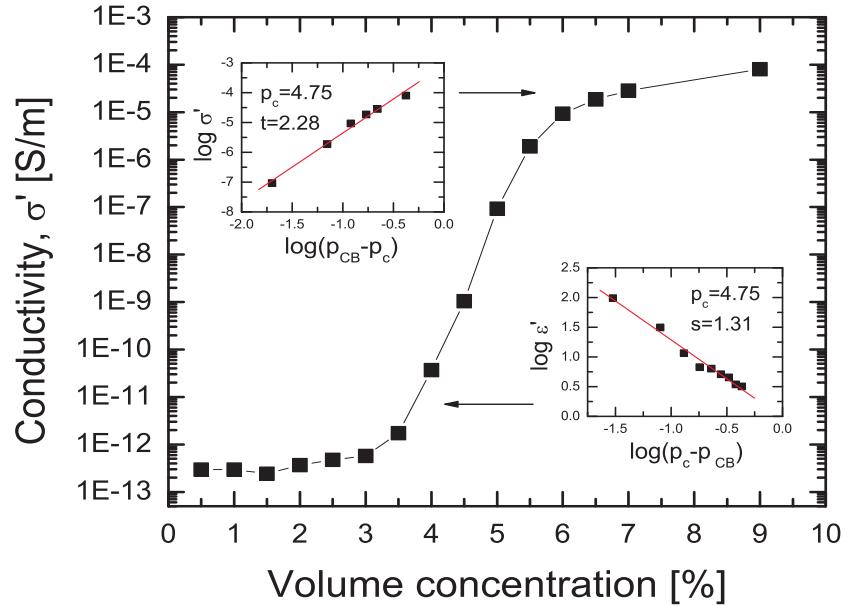
Figure 6.3: Conductivity as function of CB volume fraction measured at 10 Hz. The insets show the best fit to the percolation scaling equations.

Further evaluation of the dielectric spectra was made by modeling the spectra in terms of a network of resistors and capacitors (Sec. 2.4.2.2, Paragraph A). The ac conductivity and permittivity of percolative systems exhibit frequency dependencies given by:

$$\sigma' = \sigma_{\mathrm{dc}} + (\omega\varepsilon_{\mathrm{SEBS}}\varepsilon_0)^{\alpha_{\mathrm{c}}}(\sigma_{\mathrm{CB}})^{1-\alpha_{\mathrm{c}}}\cos(\alpha_{\mathrm{c}}\pi/2) \tag{6.1}$$

Figure 6.4: Real and imaginary part of permittivity as function of frequency for composites with 4 and 4.5 %vol and the corresponding Cole-Cole fits.
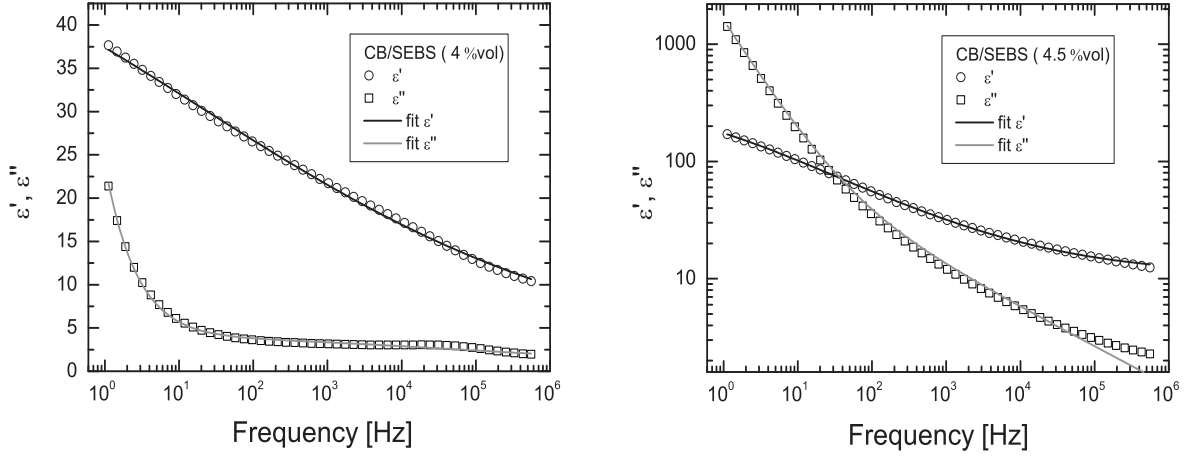
$$\varepsilon'_r = \varepsilon_\infty + (\omega\varepsilon_0)^{\alpha_c-1}\varepsilon_{\text{SEBS}}^{\alpha_c}(\sigma_{\text{CB}})^{1-\alpha_c}\sin(\alpha_c\pi/2), \tag{6.2}$$

where α_c is the volume fraction of SEBS, $\varepsilon_{\text{SEBS}}$ is the relative permittivity of SEBS, σ_{CB} is the conductivity of CB, σ_{dc} represents the plateau conductivity (determined by the percolation paths across the material), ε_∞ represents the permittivity at high frequencies. In order to determine the σ_{dc} and ε_∞ for different volume fractions, the dielectric spectra were quantitative evaluated and fitted according to the Cole-Cole equation:

$$\varepsilon(\omega) = \varepsilon_\infty + \sum \frac{\triangle\varepsilon}{1+(i\omega\tau)^\beta} + \frac{\sigma_{\text{dc}}}{i\omega\varepsilon_0}, \tag{6.3}$$

where $\triangle\varepsilon$ is the relaxation strength, τ is the relaxation time and β is the broadness parameter. The fitting was performed simultaneously for ε' and ε'' as shown in Fig. 6.4 for 4 and 4.5 %vol. The parameters obtained from the Cole-Cole fits are summarized in Table 6.1.

Table 6.1: Fit parameters for Fig. 6.4.

%vol	σ_{dc}	ε_∞	τ	β
4	$1.13*10^{-11}$	5.3	$1.9*10^{-1}$	0.17
4.5	$8.67*10^{-10}$	10.7	$8.3*10^{-3}$	0.42

The R-C network model curves shown in Fig. 6.1 and Fig. 6.2 were plotted using $\sigma_{\text{CB}} = 0.01$ S/m, $\varepsilon_{\text{SEBS}} = 2.3$ and the obtained values for the dc conductivity σ_{dc} and permittivity at high frequency ε_∞ from Table 6.1. The model curves for the frequency dependent conductivity fit very well to the experimental data, however the corresponding model curve (only $p=4$ % is shown) for the relative permittivity lies below the experimental result. Possible explanation for the discrepancy could be: 1) experimental error in the thickness measurements (ε'_r depends on the measured thickness, while σ' is thickness independent) and 2) electrode polarization caused by space charge injection near the electrodes, which has been shown to have an influence on permittivity in heterogeneous systems [51].

6.1.2   Electric breakdown test

Electric breakdown experiments performed on CB-SEBS sub-percolative composites shown in Fig. 6.5 (open squares, inset is a blow-up) reveal a large decrease in the breakdown strength compared to the pure elastomer. Even at low volume fraction (e.g. 2.5 %vol), where the dielectric spectra (Fig. 6.2) suggest a clear insulator behavior, the electric breakdown strength is lowered by more than 90 % in the composite. Two precipitous drops are observed, resulting in two distinct plateaus. It is seen that above 2.5 %vol, the breakdown strengths are below 3 V/μm, while the corresponding electrostatic energy density ($\frac{1}{2}\varepsilon_r\varepsilon_0 E_b$, ε_r at 1 Hz, full square symbols, secondary axis) shows even a steeper drop.
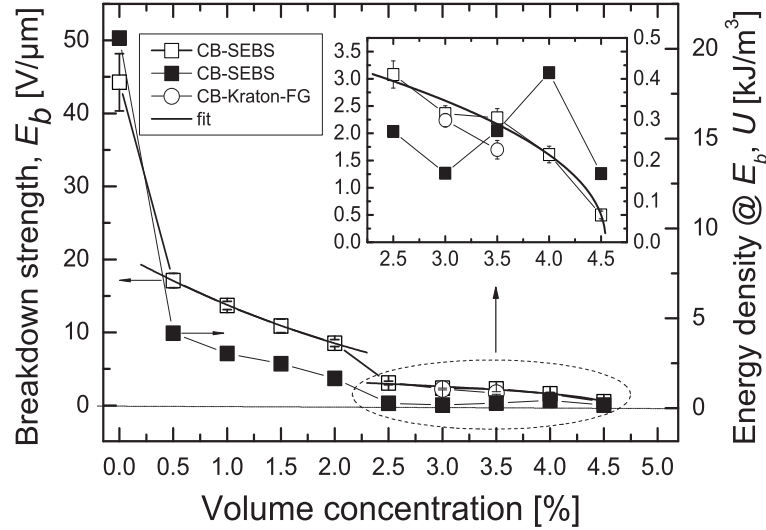

Figure 6.5: Electrical breakdown strength E_b vs CB volume concentration.

Based on that observation, it can be concluded that for this type of composite, the increase in permittivity does not make up for the reduction in breakdown strength in relation to stored electrical energy. It should be also emphasized that the corresponding dielectric spectra display an insulating behavior up to 3.5 %vol, which is commonly interpreted as a sign that the material is useful for capacitive applications, however as shown the results give an indication that the dielectric spectrum does not provide adequate information to judge the usefulness of these conductor-insulator materials for capacitive applications. To prove the generality of this result, experiments were carried out on composites with a different elastomer material (Kraton-FG 1924). The new material was SEBS based material grafted with maleic anhydride causing it to become hydrophilic. The breakdown strength of the pure material was 125 V/μm. Samples with concentrations of 3 and 3.5 %vol were investigated and was found out that their dielectric behavior (not shown) and electrical breakdown strengths (Fig. 6.5, open circles) were similar to those of CB-SEBS composites.

A possible explanation for the large reduction in electric breakdown strength, could be the formation of conducting channels of CB inside the sample, which are separated by thin insulating layers, thus forming a network of capacitors with reduced thicknesses, which contributes to the increase of the permittivity, but at the same time leads to short-circuiting of some regions in the composite, causing the voltage drop to increase in regions without conducting material (schematically shown in Fig. 6.6), leading to a local enhancement in the electric field, such that breakdown events will occur at a lower macroscopic electric field. The observed interrupted dependence with two distinct regions, can be be explained by agglomeration effects: in the low-concentration region, particles are well separated during drop-casting,
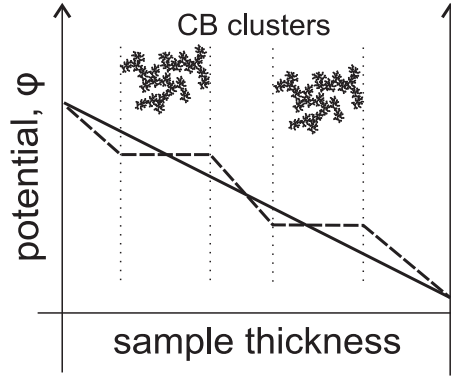
Figure 6.6: Schematic view of short-circuiting of sample volumes due to a cluster leading to increased electric field concentration.

while at higher concentrations, the particles are close enough to aggregate, forming large, structured clusters that short-circuit larger regions of the sample. Agglomeration in a similar system was observed by Flandin [102] and was found to result in anomalous percolation behavior. The plateaus were separately fitted to $E_b = (p_c - p)^y$, a model that describes electrical breakdown below the percolation threshold [35]. The low and high concentration fits resulted in $p_c = 7.73$ %vol, $y = 2.995$ and $p_c = 4.54$ %vol, $y = 0.461$, respectively. The value of the percolation threshold found from the dielectric spectra corresponds well with the value found for the high concentration electric breakdown.

6.1.2.1 Thickness dependent E_b.

In a classical 3D percolation, the size of the polymer matrix is assumed to be infinitely large compared with the size of the filler, which excludes the influence of the filler size. In reality, due to aggregation the size of the filler aggregates can approach the size of the matrix, especially for thin films (40-100 μm). Carbon black does not exist as primary particles, but as irreversibly fused primary particle clusters that have a fractal structure. During the composite preparation, these aggregates agglomerate in larger clusters, whose size depends on compatibility with the matrix and the solvent used. To investigate the influence of aggregation on the electric breakdown behavior, thickness dependent measurements were performed. The breakdown strength with increasing sample thickness was measured for samples with
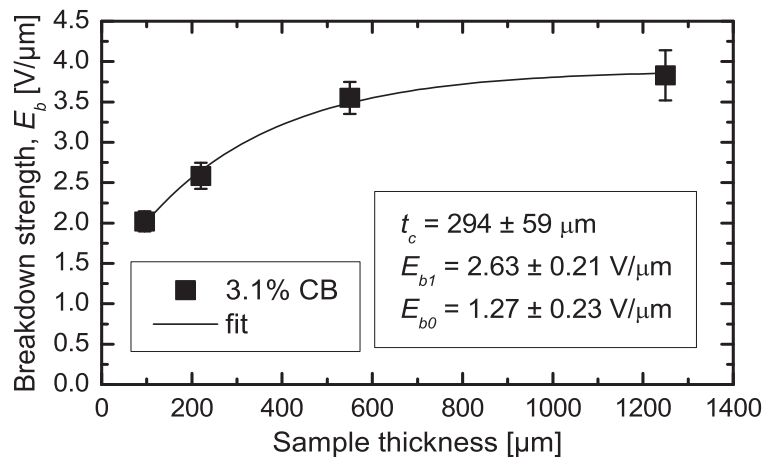

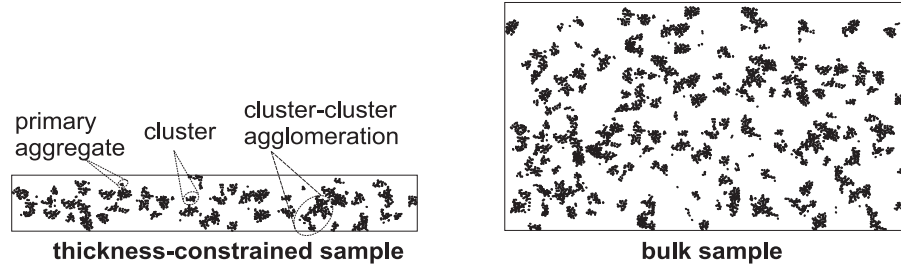Figure 6.7: Electric breakdown strength E_b vs composite thickness.

Figure 6.8: Schematic view of aggregated filler clusters in rubber for thickness-constrained sample (left) and bulk sample (right).

identical filler concentration of 3.1 %vol. (Fig. 6.7). It was verified that the dielectric spectra did not change with sample thickness. An increase of the electrical breakdown was observed, which saturates for thicker samples. The observed thickness-dependence of the breakdown strength seems to support the suggested explanation for agglomeration-enhanced reduction in breakdown strength. A phenomenological model, $E_{\mathrm{b}} = E_{\mathrm{b1}}[1 - exp(t/t_{\mathrm{c}})] + E_{\mathrm{b0}}$ with three parameters, was fitted to the available data points and the values obtained are shown in (Fig. 6.7). The measurements were found to display a critical thickness of $t_{\mathrm{c}} = 294$ μm, much larger than the average primary particle size of 30 nm. It could be argued that the cluster size is comparable to the sample thickness for thinner films (schematically shown in Fig. 6.8, left), thus shorting large area of the sample, while for thicker films a macroscopic limit is achieved (Fig. 6.8, right), in which the clusters are well dispersed, which is in effect a two-dimensional to 3D transition. The effect would be governed by a length scale on the order of the critical thickness determined in the experiment, $t_{\mathrm{c}} = 294$ μm.

6.2 Mechanical characterization

The results from tensile test measurements are shown in Fig. 6.9. As expected, the elastic modulus was
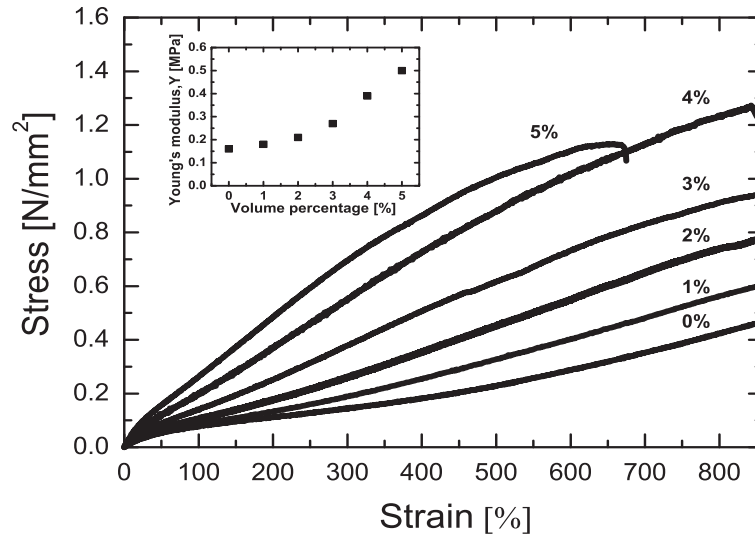

Figure 6.9: Engineering stress-strain curves and Young's modulus (left inset) measured at room temperature for different volume concentration of CB.

found to increase with content of CB due to the higher Young's modulus of the filler inclusion and efficient

load transfer to CB network. The mechanical stress is efficiently transfer from the soft rubber matrix to the carbon black fractal aggregates network leading to mechanical reinforcement. However, due to the low volume percentages used, the composites still retain relatively low stiffness, as it is required to achieve high actuation strains.

6.3 Electro-mechanical characterization

The figure of merit f, Eq. (5.1), introduced in Sec. 5.3 was applied to the experimental electro-mechanical data, in order to assess the applicability of the approach to DEA. A further figure of merit, which includes the electric breakdown strength of the material was proposed by Lotz et al. [103]:

$$k = \frac{Y_{\text{SEBS}}}{Y_{\text{c}}} \frac{E_{\text{b,c}}^2}{E_{\text{b,SEBS}}^2} \frac{\varepsilon_{\text{r}}'}{\varepsilon_{\text{SEBS}}'} \tag{6.4}$$

Eq. (6.4) is a complete measure of the usefulness of any new material for DEAs, since it includes all three important parameters for DEA: permittivity, elastic modulus and electric breakdown strength and therefore is a useful tool for comparing the expected electromechanical performance of a composite material. Improved actuation performance is expected from a composite with $k > 1$. The f, k values calculated for the different composite concentrations are shown in Table 6.2, which summarize the complete electromechanical investigation presented in this study.

Table 6.2: Electro-mechanical characterization.

CB, %vol	ε_{r}' at 1Hz	Y_{c}, [kPa]	E_{b}, [V/μm]	f	k
0	2.3	160	44.3	1	1
1	3.5	180	13.7	1.35	0.13
2	5.1	210	8.6	1.69	0.07
3	6.9	270	2.4	1.78	0.005
4	36.9	390	1.6	6.59	0.008

6.4 Conclusion

In summary, a sub-percolative composite approach for improving the electro-mechanical response of a soft elastomer has been evaluated. It was shown that the relative permittivity can be significantly increased at low volume percentages of the conductive filler, thereby preserving flexibility and elasticity of the base elastomer ($f > 1$ for all volume fractions). A serious drawback of the approach is the reduction in electric breakdown strength, such that the energy density is negatively affected. As seen, the k - figure of merit decrease drastically with the volume fraction. Based on the results presented in this chapter, it can be concluded that a simple subpercolative approach to permittivity enhancements is not useful for general applications that require storage of energy. Since the electric energy density scales quadratically with electric field, the enhancement of permittivity must be balanced by a sufficient electric breakdown strength levels. Possibly, a proper surface treatment (encapsulation) of the conductive particles could increase the breakdown strength of the composite without affecting the dielectric properties.

Chapter 7

Molecular composites

In this chapter, a completely new approach for increasing the permittivity and electric energy density of a polymer is presented, based on the concept of molecular composites. The approach specifically targets the problem of filler agglomeration, which could lead to early electric breakdown. The concept, was first suggested as a means of reinforcing a polymer at the molecular level [104], relying on the grafting of rigid rod macromolecules to a more flexible matrix. Here, for the purpose of the work the concept was modified and the aim was focused on the influence of the electromechanical properties by means of grafting π-conjugated soft macromolecules to a polymer matrix flexible backbone as described in Sec. 4.1.3. The soft macromolecules are chosen instead of rigid rod molecules to prevent mechanical reinforcement. The π-conjugated macromolecules are highly polarizable and permit charge displacement along backbone, which leads to a permittivity enhancement governed by polarization (hyperelectronic polarizaton), while the chemical bonding to the insulating backbone prevents the macromolecules from agglomerating and creating particles with detrimental local electric field concentrations, thus preserving the electric breakdown strength.

7.1 Chemical characterization

The investigated molecular composite was composed of a chemically modified SEBS block copolymer, to which a non-crystalline gel-state conjugated polymer could be grafted directly. The matrix material SEBS-g-MA (poly-styrene-co-ethylene-co-butylene-co-styrene-g-maleic anhydride) (chemical structure shown in Fig. 7.1(a)) is functionalized with 1.0 to 1.7 wt. % MA.

The unique natrure of MA chemical structure results in a highly reactive and versatile material. Chemistry of maleic anhydride is very rich, due to the unsaturated double bonds and acid anhydride groups, leading to a bifunctional reactivity. The conductive polymer polyaniline (PANI), doped with dodecyl benzene sulphonic acid (DBSA) (Fig. 7.1(b)) was grafted onto the SEBS-g-MA backbone via a chemical reaction between the secondary amine group and the maleic anhydride to achieve the PANI-grafted block copolymer of Fig. 7.1(c), requiring no further reagents. The grafting reaction was confirmed using Fourier-transform infrared spectroscopy (FTIR).
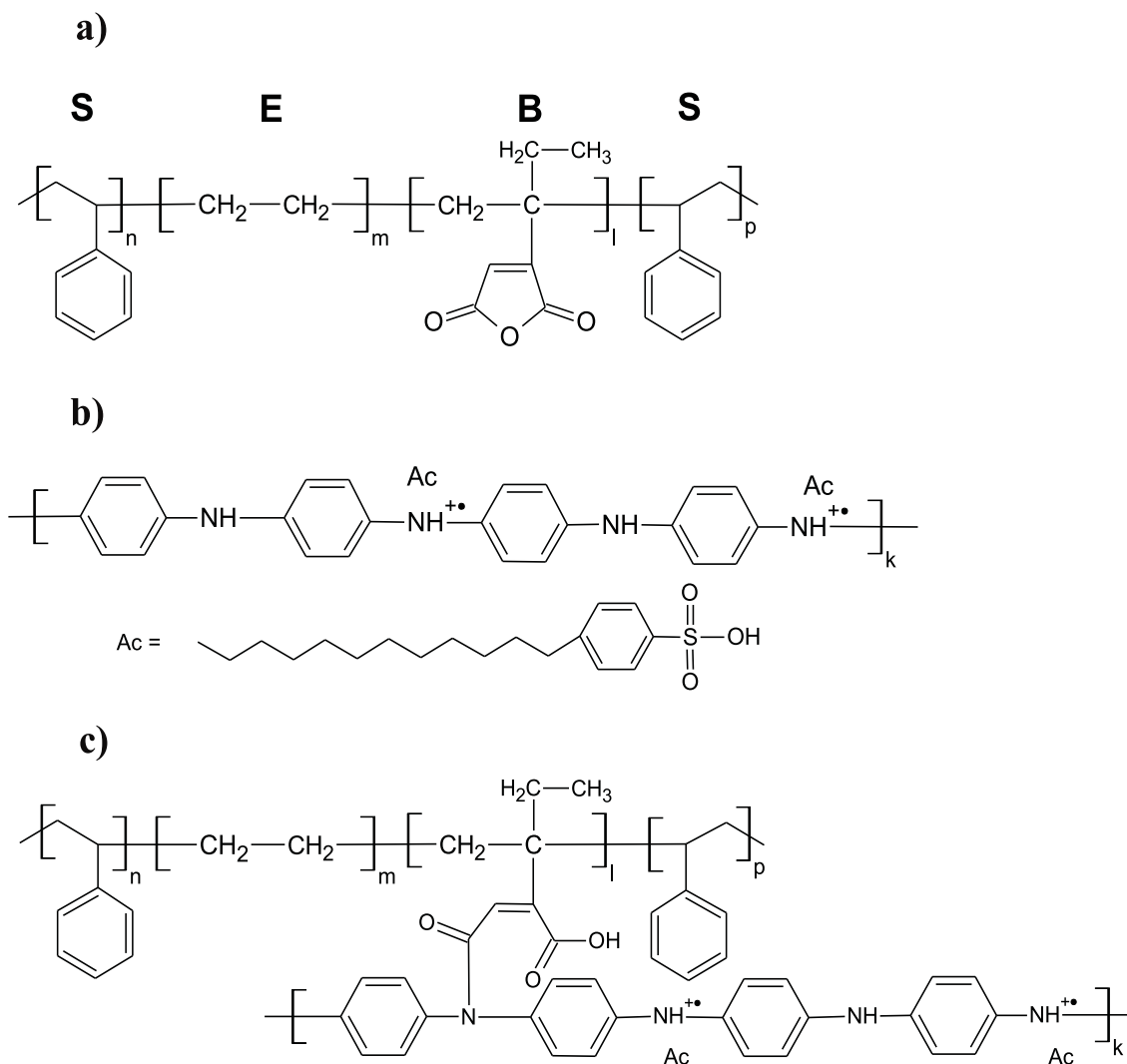
a)

b)

c)

Figure 7.1: Chemical structure of a) SEBS-g-MA, b) PANI (emeraldine salt) doped with dodecyl benzene sulfonic acid (DBSA), c) molecular composite (SEBS-g-MA grafted with PANI).

7.1.1 FTIR measurements

FTIR spectra of SEBS-g-MA, and the PANI grafted block-copolymer are shown in Fig. 7.2. The chemical grafting is evidenced by the C–N and C–C stretching vibrations associated with Amide III (1350 - 1250 cm^{-1}). Further evidence is the shoulder, known as the Amide I band, that appears on the maleic anhydride C=O stretching peak at 1712 cm^{-1} [105]. This Amide I band is shifted to lower wavelengths compared to the other carbonyl bonds due to the nitrogen atom next to the carbonyl group. The broad band at 1550 cm^{-1} is characteristic for polyaniline and is assigned to a stretching vibration of the quinoid ring [106]. The peak at 1127 cm^{-1} indicates the emeraldine salt form of PANI and could be used to estimate the doping level [107]. The two peaks at 1030 cm^{-1} and 1000 cm^{-1} are assigned to the stretching of the S=O bond of dodecyl benzene sulphonic acid (DBSA) (see Fig.1 (b)) and are commonly observed in many sulfonic acids [107]. The large band at 1017 cm^{-1} is commonly assigned to the symmetrical stretching vibration of the C–O–C ester groups in the maleic anhydride ring, and is seen to disappear when it is opened. The strongest absorption peaks are common to both spectra, and are therefore associated with the SEBS backbone of the SEBS-g-MA. The bands at 1461 cm^{-1} and 1378
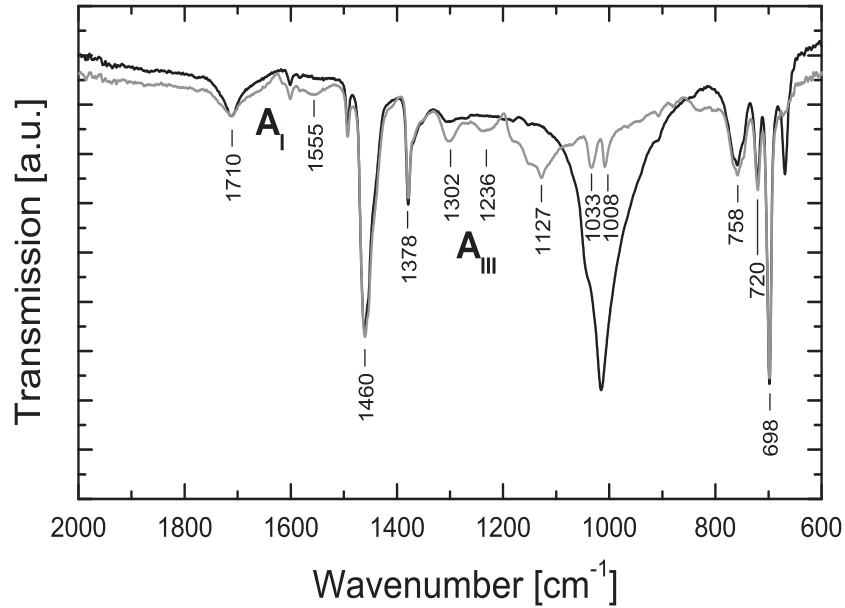
Figure 7.2: FTIR spectra of SEBS-g-MA (black line) and PANI grafted SEBS-g-MA (gray line).

cm^{-1} are assigned to the bending vibration of the EB block CH_2 group and to the C–H bending vibration of the CH_3 group on the ethyl branches of the EB block, respectively [108]. The peaks at 700 cm^{-1} and 762 cm^{-1} are assigned to the =C–H bending vibration of the phenyl group in the styrene block. The peak at 721 cm^{-1} is assigned to the C–H rocking vibration of the CH_2 in the EB block [108].

7.2 Electrical characterization

7.2.1 Dielectric characterization

Fig. 7.3 shows relative permittivity (ε'_r) and dielectric loss tangent (tan δ) as a function of frequency in the range of 0.1 Hz to 1 MHz, measured at room temperature. As expected, the relative permittivity increases smoothly with the volume fraction, however, at 2 %vol an abrupt jump is observed. In going from 2.0 %vol to 2.1 %vol, the permittivity at 1 Hz jumps from 9 to 63. Further increase in the amount of PANI leads to large further increases in permittivity, a behaviour associated with percolation. The abrupt change is strong evidence for a changeover in the mixing behaviour between matrix polymer and PANI. Below 2 %vol, all PANI can be grafted onto the backbone, while for higher amounts of PANI the ability of the backbone to graft the PANI is exhausted. At concentrations higher than 2.0 %vol, the grafting of the PANI molecules to the backbone is no longer complete, which is supported by the observed increase in conductivity (see Fig. 7.4). Exhausting the MA grafting ability leads to agglomeration and possibly a conductive network formation, as is indeed necessary for the observed percolation-enhanced permittivity. This indicates that the grafting helps to encapsulate the individual chains, such that individual chains are shielded from interacting with each other. In summary, two different mixing phenomena occur, leading in region I (see Fig. 7.3) to a polarization-dominated permittivity increase supported by fully grafted PANI molecules, and in region II to a percolation-dominated increase, a behavior governed by partially grafted PANI macromolecules. Hence, it can be expected that an increase in the amount of MA groups onto which the PANI can be grafted could lead to a shifting of the polarization governed enhancement to higher
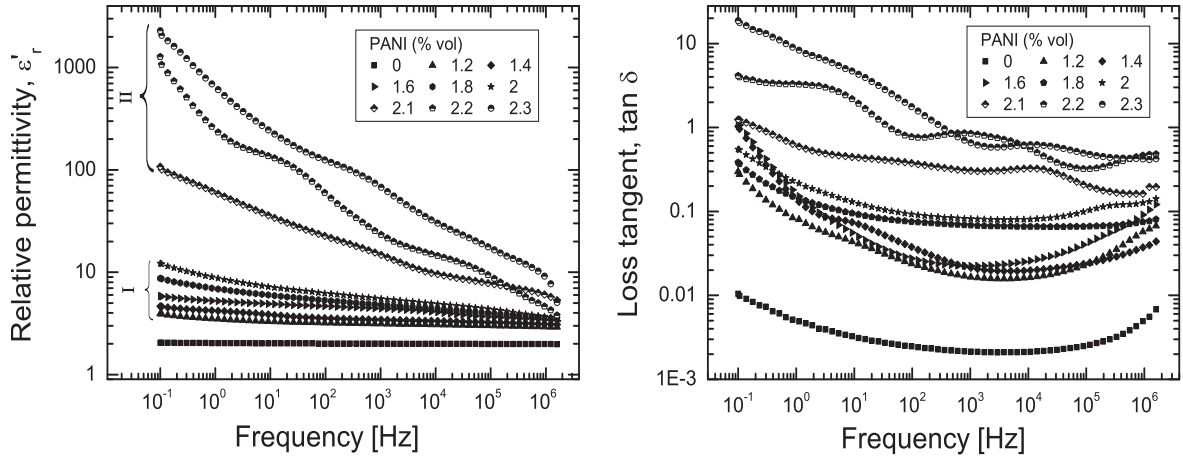
Figure 7.3: Relative dielectric permittivity (ε'_r), and dielectric loss ($\tan \delta$) as a function of frequency measured at room temperature, for varying volume concentrations of PANI.

volume percentages, thereby leading to higher permittivity values. The measured dielectric loss spectra (Fig. 7.3, right) also show a large increase in going from 2.0 %vol to 2.1 %vol, which is to be expected when percolation behaviour sets in. In region I, charge remains confined on well-separated conducting polymer chains, leading to relatively low and constant $\tan \delta$, while in region II the higher loss indicates the nearing of the insulator-conductor transition, where inter-chain hopping occurs, promoted by the presence of fractal conducting domains. The increase in dielectric loss from pure material to material with a PANI content of 1.2 %vol can be explained using the concept of hyper-electronic polarization introduced by Pohl (Sec. 2.2.1.1). Since the π-conjugated polymer chains are long, the charges may transfer far along the backbone of each separated chain. This charge migration is associated with conduction losses, which manifest themselves in the dielectric spectra [109].

The percolation behavior was investigated by measuring the conductivity of samples with a content of PANI above 2 %vol (see Fig. 7.4) and comparing the results to the mathematical prediction of percolation theory.
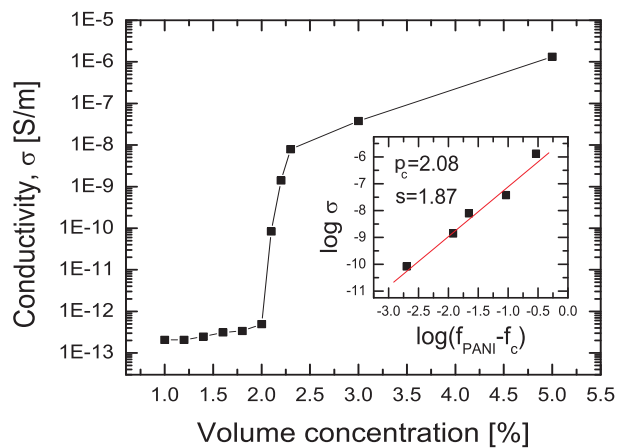

Figure 7.4: Effective conductivity of SEBS-g-MA/PANI molecular composites as a function of PANI volume fraction, measured at 1 Hz and room temperature.

The conductivity displays the common transition behavior well-known from percolating systems. The best fit to the AC conductivity measured at 1 Hz (Fig. 7.4, inset), gives values of $p_c = 2.08$ for the

percolation threshold and $s = 1.87$ for the scaling constant, which is very close to the universal value for a three-dimensional 3D lattice [73], thus reflecting the percolation behavior that sets in when the PANI concentration is above 2%vol. The very low percolation threshold could be explained by the high aspect ratio of the PANI polymer chains.

7.2.2 Electric breakdown test

Results from the breakdown tests performed for various concentrations are shown in Fig. 7.5. The electric breakdown strength of the composites displays a plateau (matching with the region I introduced previously), followed by a precipitous drop, a behavior which has been observed for percolative systems (Sec. 6.1.2).
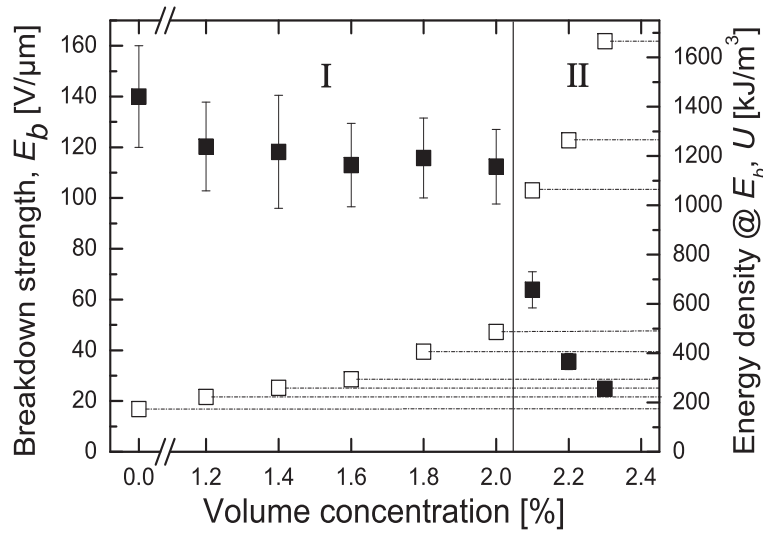

Figure 7.5: Electric breakdown strength E_b (full squares) and calculated electrostatic energy density U (open squares) at breakdown for different PANI volume concentrations.

In region I, the breakdown strength is seen to decrease from 140 V/μm for the pure material to about 120 V/μm, a drop of just 14 %. Within error, there is no further decrease in the breakdown strength until region II is reached. A system with almost no reduction in breakdown strength for a range of added conductive filler has not been reported before. The slight decrease of the breakdown strength for the molecular composites in the region I compared to the pure material, could be ascribed to the introduction of charges which increases the probability of breakdown. In region II, the composite breakdown strength decreases rapidly with the volume fraction (only the range until 2.3 %vol is shown). Also shown in Fig. 7.5 is the calculated energy density at breakdown (open square symbols, secondary axis) which shows a steady increase with the volume fraction. Interestingly, an improvement in the energy storage capacity is observed even in region II, however, this improvement might not be practically useful, as will be discussed next.

The electrical current monitored during the breakdown measurements (Fig. 7.6) shows some variation with PANI concentration. The pure material shows the lowest current during the experiment of all, and it remains constant until failure. For all composites, the current is found to increase during the breakdown experiment, but with different current characteristics. For composites with PANI contents between 1.0 and 1.8 %vol, the curves look highly similar, while for 2.0 %vol and upwards, the current rises much

faster with electric field. For all PANI concentrations until 1.8 %vol, the current increases smoothly with the electric field, following the linear ohmic behavior until failure. For 2 %vol and upwards (percolation region II) the current rises nonlinearly much faster with electric field.
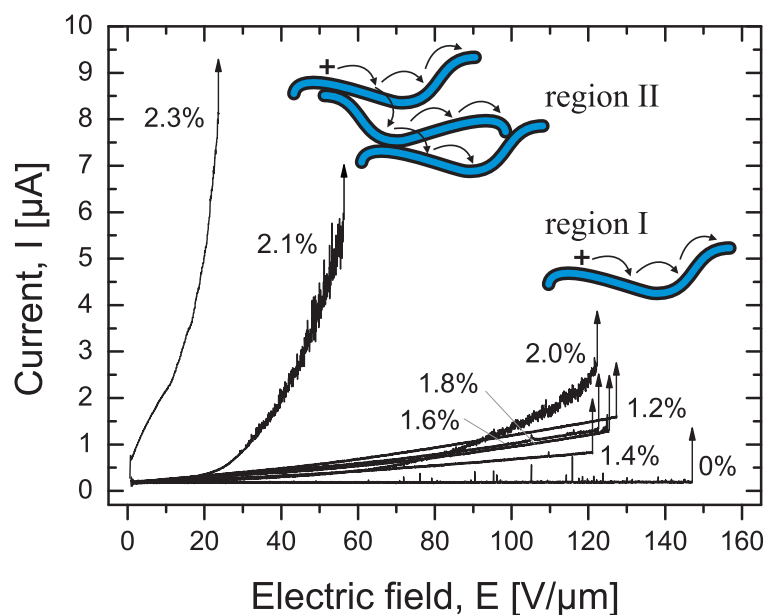

Figure 7.6: Electric current monitored during the breakdown tests vs. electric field for varying volume concentrations.

The cross-over in current characteristic could be explained as follows: The conduction behavior of PANI can be decomposed into intra-chain and inter-chain components [92]. At low PANI content, the macromolecular conductive chains are well separated and distributed, leading to a low hopping conductivity, thus the total conductivity would be dominated by impurities (e.g. the ionic conductivity of DBSA). At higher PANI content, total conductivity would be governed by chain-to-chain hopping, which results in higher current leakage at high fields. The elevated current leakage of region II might explain the extraordinary electric breakdown properties displayed in Fig. 7.5. In region I, the breakdown would be governed by the electro-mechanical instability (Sec. 2.3.1). In region II, however, the heating due to the elevated currents would cause the leading cause of breakdown to shift from electro-mechanical instability to thermal run-away. That this cross-over in current leakage occurs is seen directly from the current curves shown in Fig. 7.6.

7.3 Mechanical characterization

The influence of grafting on the mechanical properties of the molecular composites was investigated for different PANI volume fractions. The results from tensile test measurements are shown in Fig. 7.7 . The elastic moduli were determined at 0, 100 and 300 % strain as summarized in Fig. 7.7 (inset table). For 100 % and 300 % strain the elastic moduli were determined as the slope of the true stress-strain curve. The elastic modulus is found to decrease with increasing content of PANI, for which a suggested explanation follows. When bulk PANI is doped with DBSA, an ionic bond between them is formed, leading to the formation of a supramolecular comb-like structure, which in the bulk give rise to thermoreversible
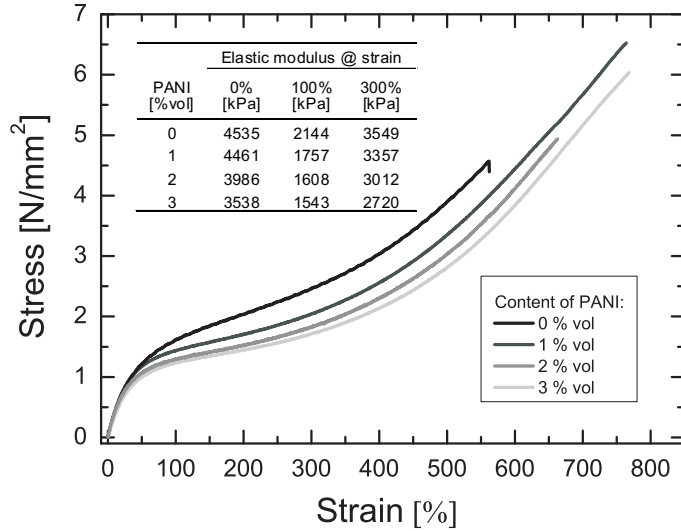
Figure 7.7: Engineering stress-strain curves of the pure elastomer SEBS-g-MA and molecular composites (SEBS-g-MA grafted PANI) with different volume fraction of PANI.

fusible networks with behaviour close to ideal rubber elasticity [92,110]. When mixed into the SEBS-g-MA material, the PANI will remain gel-like, while the reaction with the MA moieties will promote the separation of PANI-chains into single entities within the EB region, thus plasticizing the EB region. Since the reaction consumes the MA, this could cause a lowering of the glass transition temperature, which would also lead to a lowering of the elastic modulus. However, differential scanning calorimetry (DSC) measurements (not shown) could detect no difference between the samples, neither in glass transition temperatures nor in their enthalpies. Although it is difficult to verify, another suggested explanation could be that the chemical bonding of PANI to the SEBS could lead to a reduction in the degrees of freedom of the SEBS chains, thus possibly hindering to a minor extent the phase separation of the hard styrene blocks and hence affecting the mechanical properties of the elastic network.

7.4   Electro-mechanical characterization

Table 7.1 presents the complete electro-mechanical characterization of the molecular composites investigated in this study. The f and k figures of merit were calculated for each volume fraction at 0, 100 and 300 % strain. Improvement of the electro-mechanical response is expected for all %vol, at all levels of prestrain. There is a tendency for the figure of merits to increase with the prestrain until a maximum is reached and then gradually to decrease. Based on that, one would expect an optimum pre-strain, at which the actuation response would reach a maximum value.

Table 7.1: Electro-mechanical characterization.

PANI %vol	ε'_r at 1Hz	E_b $[V/\mu m]$	f			k		
			0 %	100 %	300 %	0 %	100 %	300 %
0	2	140	1	1	1	1	1	1
1.2	3.5	120	1.78	2.13	1.85	1.09	1.30	1.13
2	8.8	112	5.00	5.87	5.18	3.22	3.78	3.34
2.2	233	36	132.54	155.33	137.27	8.56	10.03	11.32

7.5   Actuation response

The electric-field induced response for the molecular composites was characterized in a constant force mode as described in Sec. 4.5.2. Increasing electric field was applied up to a 'safe limit' far below the electric breakdown strength of the material and the actuation response in direction transversal to the field was tested at different forces, in order to identify the corresponding optimum load which results in maximum actuation behavior. The results obtained for a molecular composite with 2 %vol PANI are shown in 3D plot in Fig. 7.8.
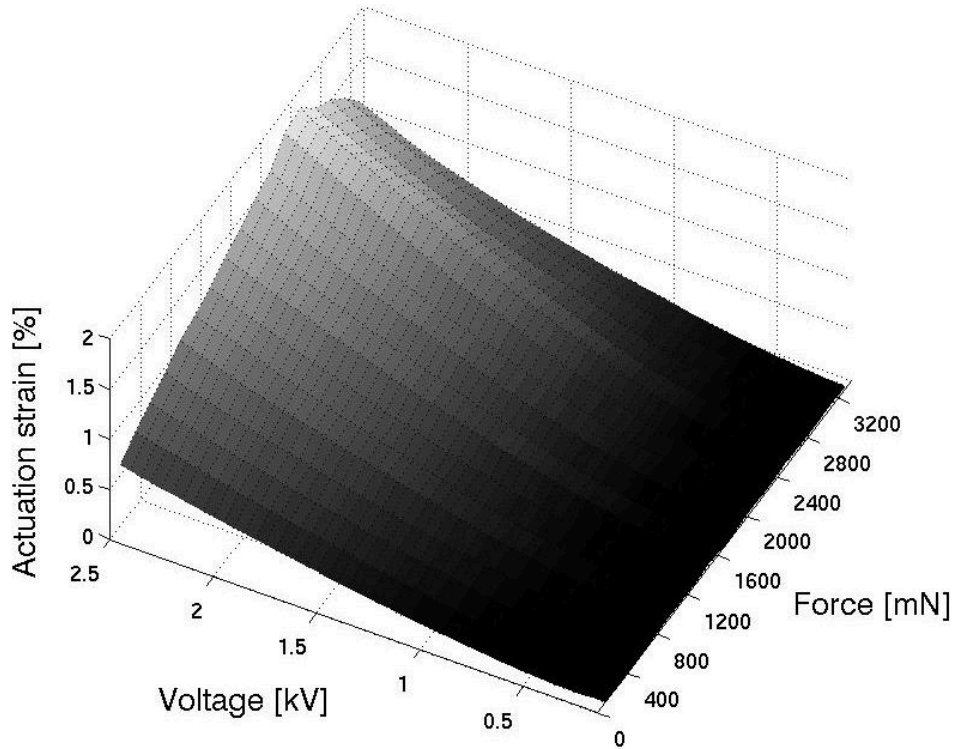

Figure 7.8: Actuation strain response of 2 %vol PANI molecular composites as a function of the applied voltage plotted for different forces.

As seen, the actuation strain at a particular voltage first tends to improve with applied force until a maximum is reached, after which the actuation strain gradually decreases. In this case, maximum actuation strain is found at a constant force of 2400 mN, which corresponds to a prestrain of 100%. This optimum force corresponds to the plateau region of the stress-strain curve, see Fig. 7.7.

The actuation strain response at optimum force for all the molecular composites tested in this study is summarized in Fig. 7.9. The curves for samples with PANI concentration up to 2 %vol could all be measured up to a safe limit of 90 V/μm, while samples with 2.1 %vol and above would suffer early breakdown. It is seen that the electromechanical response improves for all volume fractions of PANI. To measure the maximum actuation strain, the voltage was ramped higher, until electrical breakdown occurred. The measured maximum actuation strains are plotted versus the amount of PANI in the inset of Fig. 7.9. The composite with 2 %vol PANI showed the highest maximum strain, 4 % at 107 V/μm. The maximum actuation strain for the pure polymer was 1.6 % (at 136 V/μm), hence an improvement of 2.8 times was observed. Note that the 2 %vol sample is the final sample of region I. The samples in the region II suffer electrical failure at lower electric fields, hence they do not show high ultimate
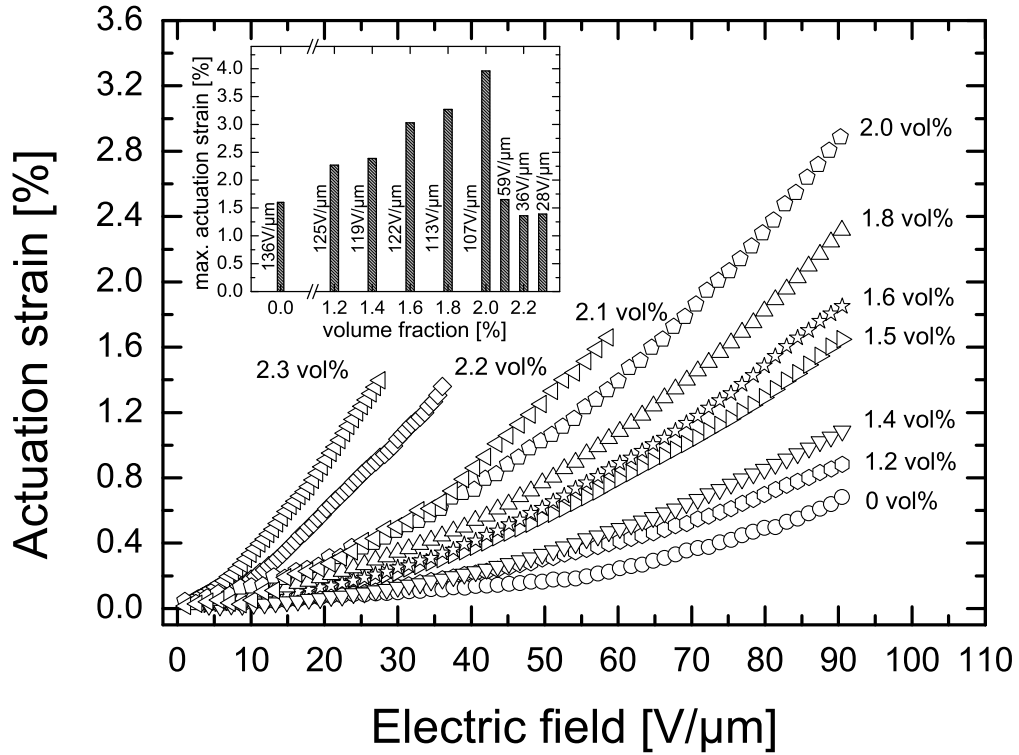
Figure 7.9: Electric-field induced strain response for the pure elastomer SEBS-g-MA and molecular composites (SEBS-g-MA grafted PANI) with different volume fraction of PANI at optimum load of 2400mN. The inset shows the maximum actuation strains at electric breakdown.

actuation strains, however, they do have higher actuation sensitivity, with higher actuation strains at a given electric field. For example, the 2.3 %vol sample shows a maximum actuation strain of 1.4 % at 27 V/μm, corresponding to a 2.2 times reduction of the electric field compared to a composite with 2 %vol, which reaches the same actuation strain at 60 V/μm. Compare to the pure elastomer, an improvement in sensitivity corresponding to 83 % reduction of the driving electric field is observed. The strain sensitivities β and elastic energy densities at maximum actuation strain were calculated for all the %vol tested and are reported in Table 7.2. It is seen that for increasing content of PANI the sensitivity increases progressively. For example, the sensitivity β increases from 0.63 nm^2/V^2 for the pure material to 3.7 nm^2/V^2 for the material with 2.0 %vol PANI. In region II, the molecular composite with the highest amount of PANI displays a sensitivity of 22.6 nm^2/V^2, which is an increase of over 30 times. The increase in the relative permittivity in combination with the decreased mechanical stiffness contributes to the observed large increase of the elastic energy density, which is an indication of an improved energy conversion efficiency. However, the high dielectric loss measured for samples in region II suggests a severe current leakage, which became pronounced at higher fields as observed from the current profiles during electric breakdown tests.

In summary, to obtain the highest sensitivity, molecular composites in Region II might be of practical use, while composites in Region I should be choosen if a combination of good sensitivity and high maximum actuation strain are required. The reported strains are relatively low due to the relatively high stiffness of the material; however, by using a softer matrix material, this can likely be improved. In this particular case this could be achieved by modifying the matrix material by lowering the styrene to ethylene-butylene ratio.

Table 7.2: Electromechanical performance of the molecular composites.

PANI [%vol]	ε'_r at 1Hz	E_b [V/μm]	β [nm^2/V^2]	U_s [kJ/m^3]
0	2	136	0.63	24.99
1.2	3.5	125	1.1	66.66
1.4	4.8	119	1.3	102.98
1.6	5.2	122	2.3	133.51
1.8	6.9	113	2.9	189.05
2	8.8	107	3.7	247.21
2.1	58.5	59	5.1	1009.92
2.2	233	36	14.4	2220.71
2.3	610	28	22.6	5570.09

7.6 Conclusion

An approach for increasing the relative permittivity and the energy density of a polymer based on the concept of molecular composites has been presented. It has been shown that grafting of a gel-like π-conjugated polymer to the backbone of a thermoplastic elastomer can lead to strongly enhanced actuation. Polarization caused by charge displacement along the conjugated backbone was found to induce a large and controlled permittivity enhancement (470 % over the elastomer matrix). It was shown that a mixing regime could be obtained, in which the composite would suffer almost no reduction in electric breakdown strength. The results presented here thus represent a large step forward in the understanding of the strategies which can be employed to obtain high permittivity polymer materials with practical use for electro-elastomer actuation.

Chapter 8

Conclusions & Further work

Conclusions

The aim of this thesis was to investigate different nanocomposite approaches with respect to their applicability for dielectric elastomer actuators and to bring physical understanding of the phenomenon involved. The main goal was to develop soft nanocomposite elastomer materials with enhanced electromechanical response, displaying improved maximum actuation strain and sensitivity. In this context, several strategies based on the use of nanoparticles for the improvement of functional properties in terms of high relative permittivity, low elastic modulus and high electric breakdown have been investigated and evaluated. In addition, a completely new approach based on the concept of molecular composites has been proposed. As a result, it has been successfully demonstrated that nanocomposite approaches to materials design can lead to useful materials with enhanced energy density and electromechanical response.

First, nanocomposites consisting of varying fractions of high permittivity rutile TiO_2 nanoparticles dispersed in thermoplastic block copolymer SEBS (poly-styrene-co-ethylene-co-butylene-co-styrene) were investigated. The nanoparticles were coated with a silicone (PDMS, poly-dimethylsiloxane) oil in order to improve the affinity between matrix and filler surfaces. It was shown that with these nanoparticles, a substantial increase of the relative permittivity up to 370 % and the corresponding electrostatic energy density (563 %) can be obtained, closely obeying the classical Lichtenecker mixing rule, while maintaining very low dielectric losses ($\tan \delta$). It was argued that the coating of TiO_2 particles improves the interfacial interaction between the particles and the polymer matrix, thus preventing the detrimental interfacial polarization causing an increase of the dielectric losses. Results from the electric breakdown measurements revealed an increase of the electric breakdown strength over the polymer matrix for higher filler fractions, e.g. 20, 30 %vol, which was attributed to the change-over from breakdown caused by electromechanical instability to those caused by thermal run-away effects. A drawback is the increase in elastic modulus, which was up to 8-fold. Improved electromechanical performances with respect to the use of pure SEBS were demonstrated for nanocomposites with nanoparticle amounts of up to 20 %vol. Maximum actuation strain of 12.3 % and sensitivity was obtained for a composite with 15 %vol, which caused a 27 % reduction of the electric field.

Second, a so-called subpercolative approach to permittivity enhancement, based on the dispersion of nano-sized conductive particles, was evaluated. It was shown that the relative permittivity can be significantly increased at low fractions of the conductive filler (13 times over the pure matrix for a nanocomposite with

4 %vol), thereby preserving the mechanical properties of the base elastomer (2-fold increase at 4 %vol). However, a serious drawback of the approach is the reduction in electric breakdown strength, such that the energy density at breakdown is severely reduced. Even at low volume fraction (e.g. 2.5 %vol), where the dielectric spectra suggest a clear insulator behavior, the electric breakdown strength was shown to be lowered by more than 90 %. The drastic reduction of the electric breakdown strength was attributed to the localized enhancement of the electric field, due to short-circuiting of some regions in the composite, such that breakdown events occurs at a lower macroscopic electric field. This conclusion was supported by an investigation of the thickness dependence of the electric breakdown strength for a fixed amount of filler, 3.1 %vol, which found that the electric breakdown strength was doubled for thicker samples compared to the thinnest sample. The increase of the electric breakdown strength with the thickness was explained as due to the cluster formation, effectively leading to a transition from two-dimensional to three-dimensional behavior as thickness increases. Based on the described experiments, it was concluded that a simple subpercolative approach to permittivity enhancements is not useful for general applications that require electrostatic storage of energy, which is the case for most applications relying on capacitance effects.

Third, a new approach for increasing the relative permittivity and electrostatic energy density of a polymer based on molecular composites was investigated, relying on chemically grafting soft gel-state π-conjugated macromolecules (polyaniline (PANI)) to a flexible elastomer backbone SEBS-g-MA (poly-styrene-co-ethylene-co-butylene-co-styrene-g-maleic anhydride). Polarization caused by charge displacement along the conjugated backbone was found to induce a large and controlled permittivity enhancement (470 % over the elastomer matrix for 2.0 %vol of PANI). The chemical bonding effectively encapsulates the PANI molecular chains, manifesting in hardly any reduction in electric breakdown strength (from 140 to 120 V/μm), and hence resulting in a large increase in stored electrostatic energy. An abrupt decrease in the breakdown field behavior was observed when the concentration of PANI exceeds 2.0 %vol, which was explained by the exhaustion of the MA moieties responsible for chemical bonding. Above this concentration, the encapsulating matrix material could no longer fully coat the PANI molecules. The transition led to drastic increases in permittivity and conductivity, and a sharp drop in electrical break-down strength. Although the transition caused further improvement of the electromechanical response, the reduction in electrical breakdown strength caused a limitation of the maximum achievable actuation strain. The increase in the relative permittivity and the observed improvement in the corresponding energy density, combined with the decreased mechanical stiffness was shown to lead to an improvement in the sensitivity of the measured electromechanical response (83 % reduction of the driving electric field) as well as in the maximum actuation strain (250 %). The approach is considered a major step towards an understanding of the strategies which can be employed to obtain high permittivity polymer materials with practical uses for dielectric elastomer actuation.

Further work

From the information collected and discussed in this study, a number of challenges and recommendations for future work can be identified:

Mixing rule nanocomposites

- chemistry and structure of the polymer-nanofiller interface

Successful design of enhanced electrostatic energy density nanocomposites based on high permittivity ceramic nanoparticles requires detailed investigation of the structure of the polymer-filler interface. Particularly when the size of the filler decreases below 50 nm, the interface becomes critical in determining the functional properties due to high surface area-to-volume ratio. Understanding of the chemistry and the interactions in the interfacial region provides a substantial opportunity to tailor the electro-mechanical properties of the nanocomposites. For example, the surface of the filler nanoparticles could be chemically functionalized by attaching proper polar groups with high dipole moment, which would induce increase of the permittivity and at the same time, would improve dispersibility in the organic media. Enhanced compatibility between filler and polymer, would possibly have a positive influence on the composite dielectric permittivity and electric breakdown strength.

Sub-percolative composites

- encapsulation of the conductive filler

Possibly, a proper surface encapsulation of the conductive particles could increase the local breakdown strength of the composite without affecting the dielectric properties. This could be done by grafting a thin insulating polymer layer to the conductive surface. For example, an excellent choice would be PVDF based ferroelectric polymers due to their high electric breakdown strength and relative permittivity. Another possibility would be a silica sol-gel encapsulation.

Molecular composites

- further enhancement of the relative permittivity

It can be expected that an increase in the amount of functional groups onto which the conjugated moieties can be grafted would lead to larger enhancement of the relative permittivity, without reduction in electric breakdown strength.

- strategies for lowering the dielectric loss

The dielectric loss could be reduced by employing PANI chains of a shorter length, so that the charges on the backbone would not migrate as far, and the migration-associated losses would be reduced. Also, other π-conjugated moieties with high polarizability and lower losses might be employed, however, as molecular composite approach implies, these must be directly grafted onto the elastomer backbone.

- further enhancement of the actuation strain

Enhancement of the actuation strain can also be done by lowering of the elastic modulus, without reducing the permittivity significantly. In the case of the molecular composites presented here, for instance, this could be achieved by modifying the matrix material by lowering the styrene to ethylene-butylene ratio. Another possibility is a physical blending with a similar thermoplastic elastomer with lower elastic modulus.

Bibliography

[1] Y. Bar-Cohen (Ed.), *Electroactive Polymer (EAP) Actuators as Artificial Muscles: Reality, Potential, and Challenges* (SPIE, Bellingham, WA, 2004).

[2] J. Pons, *Emerging Actuator Technologies: A Micromechatronic Approach* (John Wiley & Sons Ltd, England, 2005).

[3] S. Ashley, "Artificial muscle," *Sci. Am.*, **289**, 52 (2003).

[4] T. Mirfakhrai, J. Madden, R. Baughman, "Polymer artificial muscles," *Mater. Today*, **10**, 30 (2007).

[5] M. Shahinpoor, H. Schneider (Eds.), *Inteligent Materials* (Royal Society of Chemistry, Cambridge, 2008).

[6] F. Carpi, D. De Rossi, R. Kornbluh, R. Pelrine, P. Sommer-Larsen (Eds.), *Dielectric Elastomers as Electromechanical Transducers. Fundamentals, Materials, Devices, Models & Applications of an Emerging Electroactive Polymer Technology* (Elsevier, Amsterdam, 2008).

[7] R. Pelrine, R. Kornbluh, Q. Pei, J. Joseph, "High speed electrically actuated elastomers with strain greater than 100%," *Science*, **287**, 83 (2000).

[8] J. D. W. Madden, N. A. Vandesteeg, P. A. Anquetil, P. G. A. Madden, A. Takshi, R. Z. Pytel, S. R. Lafontaine, P. A. Wieringa, I. W. Hunter, "Artificial muscle technology: physical principles and naval prospects," *IEEE J. Oceanic Eng.*, **29**, 706 (2004).

[9] R. Pelrine, R. Kornbluh, J. Joseph, "Electrostriction of polymer dielectrics with compliant electrodes as a means of actuation," *Sens. Actuators, A*, **64**, 77 (1998).

[10] G. Kofod, P. Sommer-Larsen, "Silicone dielectric elastomer actuators: Finite-elasticity model of actuation," *Sens. Actuators, A*, **122**, 273 (2005).

[11] L. Qi, B. Lee, S. Chen, W. Samuels, G. Exarhos, "High dielectric constant silver-epoxy composites as embedded dielectrics," *Adv. Mater.*, **17**, 1777 (2005).

[12] C. Naber, C. Tanase, P. Blom, G. Gelinck, A. Marsman, F. Touwlager, S. Setayesh, D. Leeuw, "High-performance solution-processed polymer ferroelectric field-effect transistors," *Nat. Mat.*, **4**, 205 (2005).

[13] Y. Bai, Z.-Y. Cheng, V. Bharti, H. S. Xu, Q. M. Zhang, "High-dielectric-constant ceramic-powder polymer composites," *Appl. Phys. Lett.*, **76**, 3804 (2000).

[14] P. Barber, S. Balasubramanian, Y. Anguchamy, S. Gong, A. Wibowo, H. Gao, H. Ploehn, H. Loye, "Polymer composites and nanocomposites dielectric materials for pulse power energy storage," *Materials*, **2**, 1697 (2009).

[15] M. Wenger, D. Dasgupta, "Mixed connectivity composite material characterization for electroactive sensors," *Polym. Eng. Sci.*, **39**, 1176 (1999).

[16] Y. Rao, S. Ogitani, P. Kohl, C. P. Wong, "Novel polymer-ceramic nanocomposite based on high dielectric constant epoxy formula for embedded capacitor application," *J. Appl. Polym. Sci*, **83**, 1084 (2002).

[17] M. Arbatti, X. Shan, Z. Cheng, "Ceramic polymer composites with high dielectric constant," *Adv. Mater.*, **19**, 1369 (2007).

[18] T. Lewis, "Interfaces are the dominant feature of dielectrics at the nanometric level," *IEEE Trans. Dielectr. Electr. Insul.*, **11**, 739 (2004).

[19] Y. Sun, Z. Zhang, C. Wong, "Influence of interphase and moisture on the dielectric properties," *Polymer*, **46**, 2297 (2005).

[20] T. Tanaka, M. Kozako, N. Fuse, Y. Ohki, "Proposal of a multi-core model for polymer nanocomposite dielectric," *IEEE Trans. Dielectr. Electr. Insul.*, **12**, 669 (2005).

[21] D. Dasgupta, K. Doughty, "Polymer-ceramic composite materials with high dielectric constants," *Thin Solid Films*, **158**, 93 (1988).

[22] P. Kim, S. Jones, P. Hotchkiss, J. Haddock, B. Kippelen, S. Marder, J. Perry, "Phosphonic acid-modified barium titanate polymer nanocomposites with high permittivity and dielectric strength," *Adv. Mater.*, **19**, 1001 (2007).

[23] M. Khalil, "The role of $BaTiO_3$ in modifying the de breakdown strength of LDPE," *IEEE Trans. Dielectr. Electr. Insul.*, **7**, 261 (2000).

[24] G. Chen, A. Davies, "The influence of defects on the short-term breakdown characteristics and long-term dc performance of ldpe insulation," *IEEE Trans. Dielectr. Electr. Insul.*, **7**, 401 (2000).

[25] F. Carpi, D. De Rossi, "Improvement of electromechanical actuating performances of a silicone dielectric elastomer by dispersion of titanium dioxide powder," *IEEE Trans. Dielectr. Electr. Insul.*, **12**, 835 (2005).

[26] S. Kirkpatrick, "Percolation and conduction," *Rev. Mod. Phys.*, **45**, 574 (1973).

[27] Z.-M. Dang, Y.-H. Lin, C.-W. Nan, "Novel ferroelectric polymer composites with high dielectric constants," *Adv. Mater.*, **15**, 1625 (2003).

[28] L. Wang, Z.-M. Dang, "Carbon nanotube composites with high dielectric constant at low percolation threshold," *Appl. Phys. Lett.*, **87**, 042903 (2005).

[29] Q. Chen, P. Du, L. Jin, W. Weng, G. Han, "Percolative conductor/polymer composite films with significant dielectric properties," *Appl. Phys. Lett.*, **91**, 022912 (2007).

[30] C. Huang, Q. M. Zhang, "High-dielectric-constant all-polymer percolative composites," *Appl. Phys. Lett.*, **82**, 3502 (2003).

[31] Y. Li, M. Xu, J. Feng, Z.-M. Dang, "Dielectric behavior of a metal-polymer composite with low percolation threshold," *Appl. Phys. Lett.*, **89**, 072902 (2006).

[32] M. Panda, V. Srinivas, A. Thakur, "On the question of percolation threshold in polyvinylidene fluoride/nanocrystalline nickel composites," *Appl. Phys. Lett.*, **92**, 132905 (2008).

[33] J. Xu, C. P. Wong, "Low-loss percolative dielectric composite," *Appl. Phys. Lett.*, **87**, 082907 (2005).

[34] Q. M. Zhang, H. Li, M. Poh, F. Xia, Z.-Y. Cheng, H. Xu, C. Huang, "An all-organic composite actuator material with a high dielectric constant," *Nature*, **419**, 284 (2002).

[35] C. Huang, Q. Zhang, "Enhanced dielectric and electromechanical responses in high dielectric constant all-polymer percolative composites," *Adv. Funct. Mater.*, **14**, 501 (2004).

[36] C. Huang, Q. Zhang, "Fully functionalized high dielectric constant nanophase polymers with high electromechanical response," *Adv. Mater.*, **17**, 1153 (2005).

[37] J. Y. Li, L. Zhang, S. Ducharme, "Electric energy density of dielectric nanocomposites," *Appl. Phys. Lett.*, **90** (2007).

[38] H. Shirakawa, E. Louis, A. MacDiarmid, C. Chiang, A. Heeger, "Synthesis of electrically conducting organic polymers: halogen derivatives of polyacetylene, (CH)x)," *Chem. Commun.*, **5**, 578 (1977).

[39] M. Shaw, W. MacKnight, *Introduction to polymer viscoelasticity* (Wiley & Sons, 2005).

[40] L. Treloar, *The physics of rubber elasticity* (Clarendon Press, Oxford, 1975).

[41] C. K. Kwan, *Dielectric Phenomena in Solids* (Elsevier Academic Press, 2004).

[42] G. Raju, *Dielectrics in Electric field* (Marcel Dekker, Inc., 2003).

[43] R. Parker, "Static dielectric constant of rutile (tio2), 1.6-1060°k," *Phys. Rev.*, **124**, 1719 (1961).

[44] N. Setter, *Piezoelectric materials in devices* (EPFL Swiss Federal Institute of Technology, 2002).

[45] M. Harwood, P. Popper, D. Rushman, "Curie point of barium titanate," *Nature*, **160**, 58 (1947).

[46] T. Furukawa, "Ferroelectric properties of vinylidene fluoride copolymers," *Phase Transitions*, **18**, 143 (1989).

[47] H. Pohl, R. Rosen, *Bull. Am. Phys. Soc.*, **10**, 396 (1965).

[48] R. Hartman, H. Pohl, "Hyperelectronic polarization in macromolecular solids," *J. Polym. Sci.*, **6**, 1135 (1968).

[49] H. Pohl, "Superdielectrics polymers," *IEEE Trans. Dielectr. Electr. Insul.*, **21**, 683 (1986).

[50] A. Jonscher, "The universal dielectric response," *Nature*, **267**, 673 (1977).

[51] A. Jonscher, *Dielectric relaxation in solids* (Chelsea Dielectric Press Limited, London, 1983).

[52] A. Jonscher, "Physical basis of dielectric loss," *Nature*, **253**, 717 (1975).

[53] T. Blythe, D. Bloor, *Electrical properties of polymers* (Cambridge University Press, 2005).

[54] P. Debye, *Polar Molecules* (Dover Publications, New York, 1945).

[55] K. Cole, R. Cole, "Dispersion and adsorption in dielectrics," *J. Chem. Rev.*, **9**, 341 (1941).

[56] D. Davidson, R. Cole, "Dielectric relaxation in glycerol, propylene glycol, and n-propanol," *J. Chem. Phys.*, **19**, 1484 (1951).

[57] S. Harvriliak, S. Negami, "A complex plane analysis of dispersion in some polymer systems," *Polym. Sci. C*, **14**, 99 (1966).

[58] X. Zhao, Z. Suo, "Electromechanical instability in semicrystaline polymers," *Appl. Phys. Lett.*, **95**, 031904 (2009).

[59] M. Kollosche, G. Kofod, "Electrical failure in blends of chemically identical, soft thermoplastic elastomers with different elastic stiffness," *Appl. Phys. Lett.*, **96**, 071904 (2010).

[60] F. Carpi, P. Chiarelli, A. Mazzoldi, D. De Rossi, "Electromechanical characterisation of dielectric elastomer planar actuators: comparative evaluation of different electrode materials and different counterloads," *Sens. Actuators, A*, **107**, 85 (2003).

[61] A. Sihvola, "Mixing rules with complex dielectric coefficient," *Subsurf. Sens. Technol. Appl.*, **1**, 393 (2000).

[62] B. Sareni, L. Krahenbuhl, A. Beroual, C. Brosseau, "Complex effective permittivity of a lossy composite material," *J. Appl. Phys.*, **80**, 4560 (1996).

[63] K. Lichtenecker, K. Rother, "The derivation of the logarithmic compound law from general principles of the stationary current," *Phys. Z.*, **32**, 255 (1931).

[64] J. Maxwell-Garnett, "Colours in metal glasses and in metallic films," *Philos. Trans. R. Soc. London, Ser. A*, **203**, 385 (1904).

[65] A. Sihvola, O. Pekonen, "Effective medium formulae for bi-anisotropic mixtures," *J. Phys. D: Appl. Phys*, **29**, 514 (1996).

[66] J. Calame, "Finite difference simulations of permittivity and electric field statistics in ceramic-polymer composites for capacitor applications," *J. Appl. Phys.*, **99**, 084101 (2006).

[67] D. A. Bruggeman, "Berechnung verschiedener physikalischer konstanten von heterogenen substanzen," *Annal. Phys.*, **24**, 636 (1935).

[68] M. T. Clarkson, "Electrical conductivity and permittivity measurements near the percolation transition in a microemulsion. *II*. Interpretation," *Phys. Rev. A*, **37**, 2079 (1988).

[69] K. S. Lam, Y. W. Wong, L. S. Tai, Y. M. Poon, F. G. Shin, "Dielectric and pyroelectric properties of lead zirconate titanate/polyurethane composites," *J. Appl. Phys.*, **96**, 3896 (2004).

[70] T. Starke, C. Johnston, S. Hill, P. Dobson, P. Grant, "The effect of inhomogeneities in particle distribution on the dielectric properties of composite films," *J. Phys. D: Appl. Phys.*, **39**, 1305 (2006).

[71] T. Yamada, T. Ueda, T. Kitayama, "Piezoelectricity of a high-content lead zirconate titanate/polymer composite," *J. Appl. Phys.*, **53**, 4328 (1982).

[72] S. Cho, S. Lee, J. Hyun, K. Paik, "Comparison of theoretical predictions and experimental values of the dielectric constant of epoxy/BaTiO$_3$ composite embedded capacitor films," *J. Mat. Sci. Mater. Electr.*, **16**, 77 (2005).

[73] D. Staufer, A. Aharony, *Introduction to Percolation Theory* (Taylor & Francis, Washington D.C., 1992).

[74] J. M. Hammersley, "Percolation processes: Lower bounds for the critical probability," *Ann. Math. Statist.*, **28**, 790 (1957).

[75] D. McLachlan, B. M., R. Newnham, "Electrical resistivity of composites," *J. Am. Ceram. Soc.*, **73**, 2187 (1990).

[76] S. Munson-McGee, "Estimation of the critical concentration in an anisotropic percolation network," *Phys. Rev. B*, **43**, 3331 (1991).

[77] A. Celzard, E. McRae, C. Deleuze, M. Dufort, G. Furdin, J. Mareche, "Critical concentration in percolating systems containing a high-aspect-ratio filler," *Phys. Rev. B*, **53**, 6209 (1996).

[78] E. Garboczi, K. Snyder, J. Douglas, M. Thorpe, "Geometrical percolation threshold of overlapping ellipsoids," *Phys. Rev. E*, **52**, 819 (1995).

[79] J. Dyre, T. Schröder, "Universality of ac conduction in disordered solids," *Rev. Mod. Phys.*, **72**, 873 (2000).

[80] I. Youngs, "Exploring the universal nature of electrial percolation exponents by genetic algorithm fitting with general effective medium theory," *J. Phys. D: Appl. Phys.*, **35**, 3127 (2002).

[81] Y. Gefen, A. Aharony, S. Alexander, "Anomalous diffusion on percolating clusters," *Phys. Rev. Lett.*, **50**, 77 (1983).

[82] J. Clerc, G. Giraud, J. Laugier, J. Luck, "The electrical conductivity of binary disordered systems, percolation clusters, fractals and related models," *Adv. Phys.*, **39**, 191 (1990).

[83] J. Wu, D. McLachlan, "Scaling behavior of the complex conductivity of graphite-boron nitride percolation systems," *Phys. Rev. B*, **52**, 880 (1998).

[84] D. Almond, B. Vainas, "The dielectric properties of random r-c networks as an explanation of the universal power law dielectric response of solids," *J. Phys.: Condens. Matter.*, **11**, 9081 (1999).

[85] D. Almond, C. Bowen, D. Rees, "Composite dielectrics and conductors: simulation, characterization and design," *J. Phys. D: Appl. Phys.*, **39**, 1295 (2006).

[86] G. Holden, N. Legge, R. Quirk (Eds.), *Thermoplastic Elastomers* (Hanser, New York, 2004).

[87] M. Morton, *Anionic Polymerization: Principles and Practice* (Academic Press, New York, 1983).

[88] J. Muscat, V. Swamy, N. M. Harrison, "First-principles calculations of the phase stability of TiO$_2$," *Phys. Rev. B*, **65**, 224112 (2002).

[89] J. Donnet, R. Bansal, M. Wang, *Carbon black, science and technology, 2nd edition* (New York, Marcel Dekker, 1993).

[90] Y. Cao, P. Smith, A. J. Heeger, "Counter-ion induced processibility of conducting polyaniline and of conducting polyblends of polyaniline in bulk polymers," *Synth. Met.*, **48**, 91 (1992).

[91] Y. Xia, J. M. Wiesinger, A. G. MacDiarmid, "Camphorsulfonic acid fully doped polyaniline emeraldine salt: conformations in different solvents studied by an ultraviolet/visible/near-infrared spectroscopic method," *Chem. Mater.*, **7**, 443 (1995).

[92] T. Vikki, J. Ruokolainen, O. Ikkala, "Thermoreversible gels of polyaniline: viscoelastic and electrical evidence on fusible network structures," *Macromolecules*, **30**, 4064 (1997).

[93] B. Stuart, *Infrared spectroscopy: fundamentals and applications* (John Willey & Sons Ltd, England, 2004).

[94] F. Carpi, D. De Rossi, "Improvement of electromechanical actuating performances of a silicone dielectric elastomer by dispersion of titanium dioxide powder," *IEEE Trans. Dielectr. Electr. Insul.*, **12**, 835 (2005).

[95] G. Gallone, F. Carpi, D. De Rossi, G. Levita, A. Marchetti, "Dielectric constant enhancement in a silicone elastomer filled with lead magnesium niobate-lead titanate," *Mater. Sci. Eng., C*, **27**, 110 (2007).

[96] D. Ma, T. Hugener, R. Siegel, A. Christerson, E. Martensson, C. Onneby, L. Schadler, "Influence of nanoparticle surface modification on the electrical behaviour of polyethylene nanocomposites," *Nanotechnology*, **16**, 724 (2005).

[97] F. Greuter, M. Siegrist, P. Kluge-Weiss, R. Kessler, L. Donzel, R. Loitzl, H. Gramespacher, "Microvaristors: Functional fillers for novel electroceramic composites," *J. Electroceram.*, **13**, 739 (2004).

[98] E. Martensson, U. Gafvert, U. Lindefelt, "Direct current conduction in SiC powders," *J. Appl. Phys.*, **90**, 2862 (2001).

[99] J. Li, M. Alim, S. Luo, W. Yao, Z. Tang, Z. Zang, "The microstructure and electrical behavior of TiO_2," *J. Electroceram.*, **13**, 751 (2004).

[100] F. Greuter, Y. Dirix, P. Kluge-weiss, R. Kessler, W. Schmidt, "Polymer compound with non linear current-voltage characteristic and method of making a polymer compound," (2003).

[101] X. H. Zhao, Z. G. Suo, "Method to analyze electromechanical stability of dielectric elastomers," *Appl. Phys. Lett.*, **91**, 061921 (2007).

[102] L. Flandin, T. Prasse, R. Schueler, K. Schulte, W. Bauhofer, J.-Y. Cavaille, "Anomalous percolation transition in carbon-black–epoxy composite materials," *Phys. Rev. B*, **59**, 14349 (1999).

[103] P. Lotz, M. Matysek, K. Flittner, H. F. Schlaak, "Reduction of the driving voltage in dielectric elastomer actuators," *Proc. 11th International Conference on New Actuators*, 868 (2008).

[104] M. Takayanagi, "Polymer composites of rigid and flexible molecules," *Pure Appl. Chem.*, **55**, 819 (1983).

[105] A. Ganguly, A. Bhowmick, "Effect of polar modification on morphology and properties of styrene-(ethylene-co-butylene)-styrene triblock copolymer and its montmorillonite clay-based nanocomposites," *J. Mater. Sci.*, **44**, 903 (2009).

[106] G. Louarn, M. Lapkowski, S. Quillard, A. Pron, J. Buisson, S. Lefrant, "Vibrational properties of polyaniline-isotope effects," *J. Phys. Chem.*, **100**, 6998 (1996).

[107] S. Kim, J. Ko, J. Chung, "Electrical conductivity change of polyaniline-dodecyl benzene sulfonic acid complex with temperature," *Polym. Adv. Technol.*, **7**, 599 (1999).

[108] T. Zhou, A. Zhan, C. Zhao, H. Liang, Z. Wu, J. Xia, "Molecular chain movements and transitions of SEBS above room temperature studied by moving-window two-dimensional correlation infrared spectroscopy," *Macromolecules*, **40**, 9009 (2007).

[109] H. Pohl, M. Polak, "Nomadic polarization in quasi one dimensional solids," *J. Chem. Phys.*, **66**, 4031 (1977).

[110] J. Hartikainen, M. Lahtinen, M. andTorkkeli, R. Serimaa, J. Valkonen, K. Rissanen, O. Ikkala, "Comb-shaped supramolecules based on protonated polyaniline and their self-organization into nanoscale structures: polyaniline sulfonates/zinc sulfonates," *Macromolecules*, **34**, 7789 (2001).

Statement of Authorship/ Selbstständigkeitserklärung

I hereby declare that I have written this dissertation by myself and referred every source. This dissertation has not been submitted for the award of any other degree in any other tertiary institution. I have read and accepted the doctoral degree regulations of the mathematical natural scientific faculty of the University of Potsdam.

Hiermit erkläre ich, dass ich die vorliegende Arbeit selbstständig und nur unter Verwendung der angegebenen Hilfmittel angefertigt habe. Diese Arbeit wurde keiner anderen Prüfungsbehörde vorgelegt. Die Promotionsordnung der Mathematisch-Naturwissensachftlichen Fakultät der Universität Potsdam habe ich gelesen und akzeptiert.

<div style="text-align:right">

Hristiyan Stoyanov
Potsdam, Mai 2010

</div>

Publications

Parts of this work have been published in the following journals and conference proceedings as well as presented in the listed conferences as oral presentation or poster.

Publications in peer reviewed journals

A co-axial dielectric elastomer actuator
H. Stoyanov, G. Kofod and R. Gerhard
Advances in Science and Technology, **87**, 81 (2008)

Dielectric properties and electric breakdown strength of a subpercolative composite of carbon black in thermoplastic copolymer
H. Stoyanov, D. N. Mc Carthy, M. Kollosche and G. Kofod
Applied Physics Letters , **94**, 232905 (2009)

Molecular composites with enhanced energy density for electroactive polymers
H. Stoyanov, M. Kollosche, D. N. Mc Carthy and G. Kofod
Journal of Materials Chemistry , (2010), accepted for publication

Elastic block copolymer nanocomposites with controlled interfacial interactions for artificial muscles
H. Stoyanov, M. Kollosche, S. Risse, D. N. Mc Carthy and G. Kofod
Soft Matter, to be submitted

Broad-spectrum enhancement of polymer composite dielectric constant at ultra-low doping caused by silica-supported copper nanoparticles
G. Kofod, S. Risse, H. Stoyanov, D. N. Mc Carthy, S. Sokolov and R. Kraehnert
ACS Nano, submitted

Multilayer coaxial fiber dielectric elastomers for actuation and sensing
G. Kofod, H. Stoyanov, and R. Gerhard
Applied Physics A, to be submitted

Conference contributions

A co-axial dielectric elastomer actuator
 H. Stoyanov, G. Kofod and R. Gerhard
 DPG-Spring Meeting 2008, Berlin, Germany, February 25-29, 2008

A co-axial dielectric elastomer actuator
 H. Stoyanov, G. Kofod and R. Gerhard
 3rd International Conference "Smart Materials, Structures and Systems"
 (CIMTEC 2008), Acireale, Italy, June 8-13, 2008

Sub-percolative composites for dielectric elastomer actuators
 H. Stoyanov, M. Kollosche, D. N. Mc Carthy, A. Becker, S. Risse and G. Kofod
 Proceedings of SPIE, **7493**, 74930Q (2009)
 Second International Conference on Smart Materials and Nanotechnology
 in Engineering, Weihai, China, July 8-11, 2009

Flexible enhanced energy density composites for dielectric elastomer actuators
 H. Stoyanov, M. Kollosche, D. N. Mc Carthy, S. Risse, A. Becker, H. Ragusch
 and G. Kofod, *Proceedings of SPIE*, **7642**, 76422G (2010)
 Electroactive Polymer Actuators and Devices (EAPAD) 2010
 San Diego, CA, USA, 8-11 March, 2010

The influence of mechanical properties in the electrical breakdown in
poly-styrene-ethylene-butadiene-styrene thermoplastic elastomer
 M. Kollosche, M. Melzer, A. Becker, H. Stoyanov, D. N. Mc Carthy,
 H. Ragusch and G. Kofod, *Proceedings of SPIE*, **7287**, 728729 (2009)
 Electroactive Polymer Actuators and Devices (EAPAD) 2009
 San Diego, CA, USA, 8-11 March, 2009

Materials science on the nano-scale for improvements in actuation properties
of dielectric elastomer actuators
 G. Kofod, D. N. Mc Carthy, H. Stoyanov, M. Kollosche, S. Risse, H. Ragusch,
 D. Rychkov, M. Dansachmüller and R. Wache, *Proceedings of SPIE*, **7642**, 764220J (2010)
 Electroactive Polymer Actuators and Devices (EAPAD) 2010
 San Diego, CA, USA, 8-11 March, 2010

Dependence on boundary conditions for actuation characteristics
of dielectric elastomer actuators
 M. Kollosche, H. Stoyanov, H. Ragusch and G. Kofod
 Proceedings of SPIE, **7642**, 76422X (2010)
 Electroactive Polymer Actuators and Devices (EAPAD) 2010
 San Diego, CA, USA, 8-11 March, 2010